THE NEUTRON FISSION CROSS SECTION OF $^{235}_{92}U$ AND $^{238}_{92}U$ IN THE ENERGY RANGE 0.3 - 12.5 MeV

WOLFGANG W. OSTERHAGE

Submitted to the University of Glasgow

as a Thesis for the Degree of Doctor of Philosophy

July 1976

ProQuest LLC.
789 East Eisenhower Parkway
P.O. Box 1346
Ann Arbor, MI 48106 – 1346

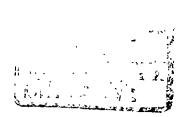

I N D E X

PREFACE

The project, presented in this thesis, has been carried out by the author at the Kelvin Laboratory of the Departement of Natural Philosophy of the University of Glasgow during the Period November 1973 to May 1976.

The experimental and theoretical work was aimed at determining the neutron fission cross sections of U-235 and U-238 in the energy range 0.3 - 12.5 MeV with good resolution and reasonable statistics. The main instrument used was the 100 MeV electron linear accelerator of the laboratory, providing a pulsed neutron source in connection with a bremsstrahlung target.

To carry out the research, it was primarily necessary, to understand the fission process in detail and the associated models. To describe it and the cross sections required the use of the liquid drop model, shell corrections, the optical and the statistical model. To see the present work in perspective, a review of past and present work in this field was neccessary.

The main instrument, apart from the accelerator, with which the experiments were carried out, was a high resolution gas scintillator, used as a time-of-flight spectrometer. This scintillator was developed by the author with Xenon as the gas in question, and by using a Cf-252 natural fission source for testing during the development. The monitor detectors, chosen for the experiments, were standard neutron detectors.

During a series of accelerator tests the optimum electronic data collection system was developed by the author. This was assisted by a bi-dimension data storage programme for a PDP-7 on line computer, earlier written by J. D. Kellie.

Apart from the time to energy conversion, which was done by a computer code by J. D. Kellie, the analysis of the data was entirely original, especially the background subtraction. Although the mathematical mechanism had been developed by J. D. Kellie, the criteria for this sub-traction were due to the author. This is also true for all normalizations and corrections.

Interpretation of the general shape of the cross sections as well as interpretation of any apparent structure has been carried out solely by the author. The computer programmes for the theoretical calculations, including fission, neutron-capture-γ-ray-emission, total scattering transmission coefficients and the final cross section calculations, have been written by the author himself, and only a code by J. D. Kellie for the calculation of the incoming wave transmission coefficients was adopted.

PUBLICATIONS

Cross Sections For the Reactions (n,f) For U-235 and U-238
by W. W. Osterhage, S. J. Hall, J. D. Kellie, and G. I. Crawford,
presented at the International Conference on Interactions of
Neutrons With Nuclei (ICINN), Boston, Mass., USA - 1976

Neutron Total Cross Section of Y-89
by J. D. Kellie, S. J. Hall, G. I. Crawford, and W. W. Osterhage,
presented at the International Conference on Interactions of
Neutrons With Nuclei (ICINN), Boston, Mass., USA - 1976

ACKNOWLEDGEMENTS

The author would like to express his gratitude towards Professor G. R. Bishop as head, Professor J. M. Reid as acting director of the Kelvin Laboratory and Professor J. C. Gunn as head of the Department of Natural Philosophy of the University of Glasgow for making available all the facilities of the Laboratory and the Departement, necessary for his research programme to have been carried out and for their interest in his work.

The author also wishes to thank Dr. S. J. Hall in particular for the close and very helpful supervision during his research project and for all the valuable advise and encouragement throughout this period.

It is also gratefully appreciated, that Dr. G. I. Crawford and Dr. J. D. Kellie of the Neutron-Time-of-Flight group were available for inspiring discussions and with assistance during the accelerator operations.

Thanks are also due to the Technical Staff of the Kelvin Laboratory under Mr. R. W. Costford and Mr. A. Keddie and in particular to Mr. J. Fraser of the vacuum workshop, as well as to Mrs. E. Taylor for preparing the photographs.

The author also wants to express his appreciation of a most generous grant by the Council of Europe, received through the British Council, which made his work possible in the first place.

Last, not least, the author would like to thank his wife for typing this thesis and for her assistance and encouragement throughout the period of his work.

CHAPTER I

1.1 Introduction

Because of the fact that neutrons do not carry any charge, they are most suitable as projectiles to be used for the investigation of nuclei. They can penetrate the Coulomb barrier at all energies undisturbed and react with the nucleus via the strong interaction.. Thus neutrons provide a useful tool for nuclear structure studies concerning the strong interaction..This, of course, is also true for the particular reaction of nuclear fission.

The study of nuclear fission with neutrons not only yields information about the physical nature and behaviour of heavy nuclei, but is at present also of considerable commercial interest. For the design of a power generating nuclear reactor the exact knowledge of the neutron fission cross section of e.g. U-235 is essential. This additional interest clearly distinguishes fission studies with neutrons from those with other projectiles.

This first chapter will firstly give an account of the considerable research work that has already been done in the field of neutron-induced fission. It then follows an introduction to the principal mechanism of nuclear fission, which will lead over to the description of the liquid drop model, as the earliest and most successfully used model, to describe in detail the fission process. There will also be a subsection, dealing with shell-corrections, which have become neccessary, to maintain the relevance of the liquid drop model. For theoretical calculations of cross sections, however, it has been found neccessary

to apply the optical and the statistical models to the concept of fission. This, together with an assessment of the present state of experimental work will cover the rest of this chapter.

1.2 Review of Past Experimental and Theoretical Work

The first observations of a nuclear fission process by O. Hahn and F. Strassmann[1] and later among others by L. Meitner and O. R. Frisch[2] was the result of a radiochemical study. These types of experiments were to dominate the further investigation of the fission process for some time and were most suited for the unambiguous selection of fission events and later for the determination of the fission fragment mass distribution. By their nature these were relatively slow experiments and therefore not particularly well suited for measurements of any fission cross sections. Nevertheless, there was already considerable theoretical interest in the shape of the cross section a short time after the discovery of fission. N. Bohr and J. A. Wheeler[3] were the first to put these considerations on solid ground by applying the liquid drop model, earlier developed by C. F. v. Weizsaecker[4], to nuclear fission.

For any measurements involving fission, neutron sources with either thermalized or monoenergetic neutrons or neutrons of a few discrete energies were used entirely in the early years, relying on (α, n)-reactions by bringing a suitable light isotope, such as $_{4}Be^{9}$ together with an α-unstable heavy isotope. After 1944 the neutron flux of experimental reactors made a continuous spectrum available and energy-determination was achieved by using the chopper-technique. Event-counting, and, if necessary, timing was done with proportional fission-chambers,

the resolution of which proved sufficient for the low energy neutrons. The use of the chopper limited the energy-range, that could be looked at to at most the keV-region.

The advent of synchrotons and particularly linear accelerators in the early 1950s allowed the operation of pulsed neutrons sources and the introduction of the time-of-flight-technique for much higher neutron energies. The simultaneous development of electronic equipment, relying on semi-conductor materials, and new detection techniques made fast timing possible. Today most neutron flux monitors are based on scintillators, liquid or solid, mounted on fast photomultiplier tubes. As fission fragment counters, surface-barrier semi-conductor detectors and proportional counters play an important role. Gas scintillators, as the one used in this research project, are a relatively new feature and have not been widely used up to date.

The development of neutron sources and detection techniques enabled measurements of fission cross sections to be improved from early spot measurements to a wide range of energies and get to know their general shape to a very high degree of accuracy. It will be pointed out in a later section of this chapter, what the present state of knowledge amounts to, and what future trends in this field can be expected.

Theoretical work in the field of fission was mainly concerned with the application of the liquid drop model to the description of the mass and energy distribution of fission fragments. Attempts have been made

to explain all phenomena by this model and to reconcile it with the miscroscopic independent particle model. However, complex investigations by J. R. Nix and W. J. Swiatecki[6] and W. D. Meyers and W. J. Swiatecki[7] showed, that shell effects play an important part in ground state deformations as well as during the fission process. But the most recent and far-reaching innovation is a postulation by V. M. Strutinsky[8] to the extent, that at least some fissile nuclei do have more than one fission barrier.

Successful calculations of fission cross sections, using a modified Hauser/Feshbach method, which has also been used in this project, have only been carried out recently. A complete and detailed acoount can be found in a publication by J. E. Lynn[9].

1.3 The Principles of the Fission Process

Fissile nuclei, having a high mass, can in their ground state already be in an energetically unfavourable state, such that just a small additional amount of energy leads to an unstable configurations. In this state of deformation the repulsing Coulomb forces of the protons exceed the surface tension holding the nucleus together, and this leads to the final breakup of the nucleus. So, when a neutron enters such a nucleus, a new exit channel exists, according to the reaction

$$ {}_{a}X^{b} + {}_{0}n^{1} \longrightarrow {}_{a-c}Y^{b+1-d-m} + {}_{c}Z^{d} + m\,{}_{0}n^{1} \quad , \qquad (1.3.1) $$

competing with all other known reaction channels. However, this reactions can be analysed more closely, leading to the observation that two different kinds of fission reactions compete with each other: the direct and the compound nucleus reactions, according to two different

ways of energy transfer from the projectile to the target.

Firstly, there is a possibility of direct momentum transfer when the in-coming neutron gives all its kinetic energy to the target nucleus, and the latter will split due to the pure mechanical impact. These direct reactions become more important at higher incident energies anddominate above 15 MeV.

The second possibility is the capture of an incoming neutron by the nucleus and the formation of a compound nucleus with a finite lifetime, according to the reaction

$$ {}_{a}X^{b} + {}_{0}n^{1} \longrightarrow ({}_{a}X^{b+1})^{*} \longrightarrow Fission \qquad (1.3.2) $$

The compound nucleus $({}_{a}X^{b+1})^{*}$ will be excited, after absorbing both the incident momentum and the binding energy of the additional neutron. Compound reactions are prevalent at lower energies and can yield information about the structure of the intermediate nucleus. It will assume a vibrational state, from which it will decay via the fission mode, when the ratio of Coulomb to surface energy is favourable. Since for some nuclei the binding energy of the additional neutron can be sufficient to excite them to a fissionable state, these isotopes will show a thermal cross section.

Pict. 1 shows a diagram, including the different steps leading to fission. A spherical ground state is assumed, and after a neutron has entered, the nucleus gets into a deformed excited state. This

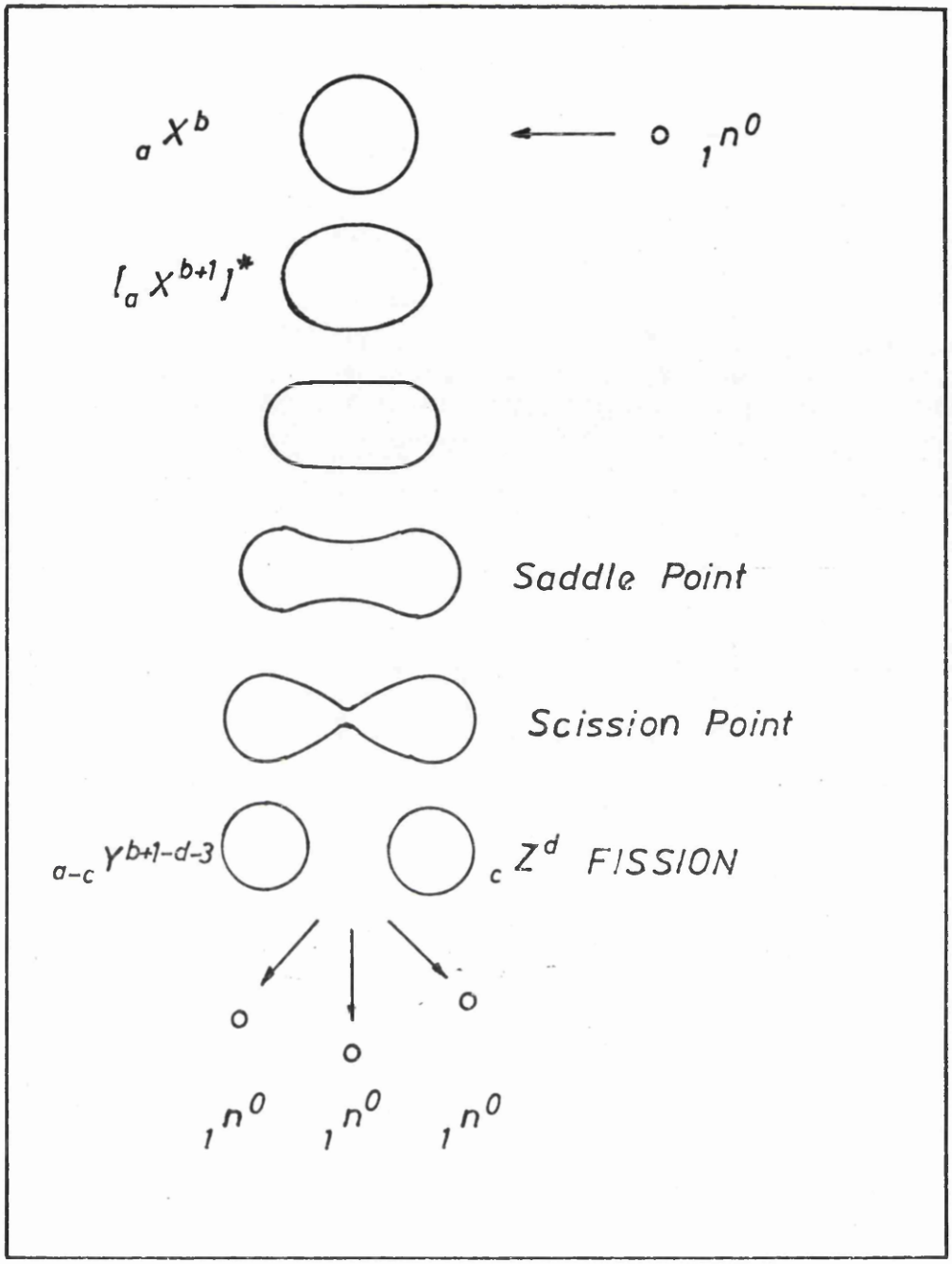

Pict.1: Basic Features of the Fission Process

deformation leads to a more and more prolate shape with eventually two mass concentrations on either side, connected by a thinner neck. When this situation is reached, i.e. when the only possible decay mode left is fission, the nucleus has passed over the saddle point. The neck grows thinner, until two adjacent spheres are left, and the instant of their final separation is called scission. There may be a few neutrons, usually not more than three, being evaporated during or after the fission process. It is also possible, that prior to fission, the nucleus decays by releasing one or even more successive neutrons, but may still have enough excitation to complete the process. Another mode is ternary fission, occuring with a probability of less than 1 %, in which the event is accompanied by a third fragment, usually an α-particle.

To give an example of the difference between direct and compound nucleus fission, the mass distributions, following these processes, are presented qualitatively in pict. 2a and 2b. Pict. 2a shows the distribution, according to direct reactions, as a Gaussian, peaking at half the mass of the original nucleus. This can easily be seen, because a splitup, due to direct momentum transfer, will be in most cases a symmetrical one. A decay, however, starting from a compound nucleus formation, takes a finite time and thus enables the single particles in the two mass groups to reorganise themselves, according to closed shell formations. This, as will be shown later, leads to the splitup into two asymmetric fragments, as can be seen from 2b. Since thermal fission is assumed here, there are no direct interactions and thus no significant contribution to symmetric fission. Pict. 2c

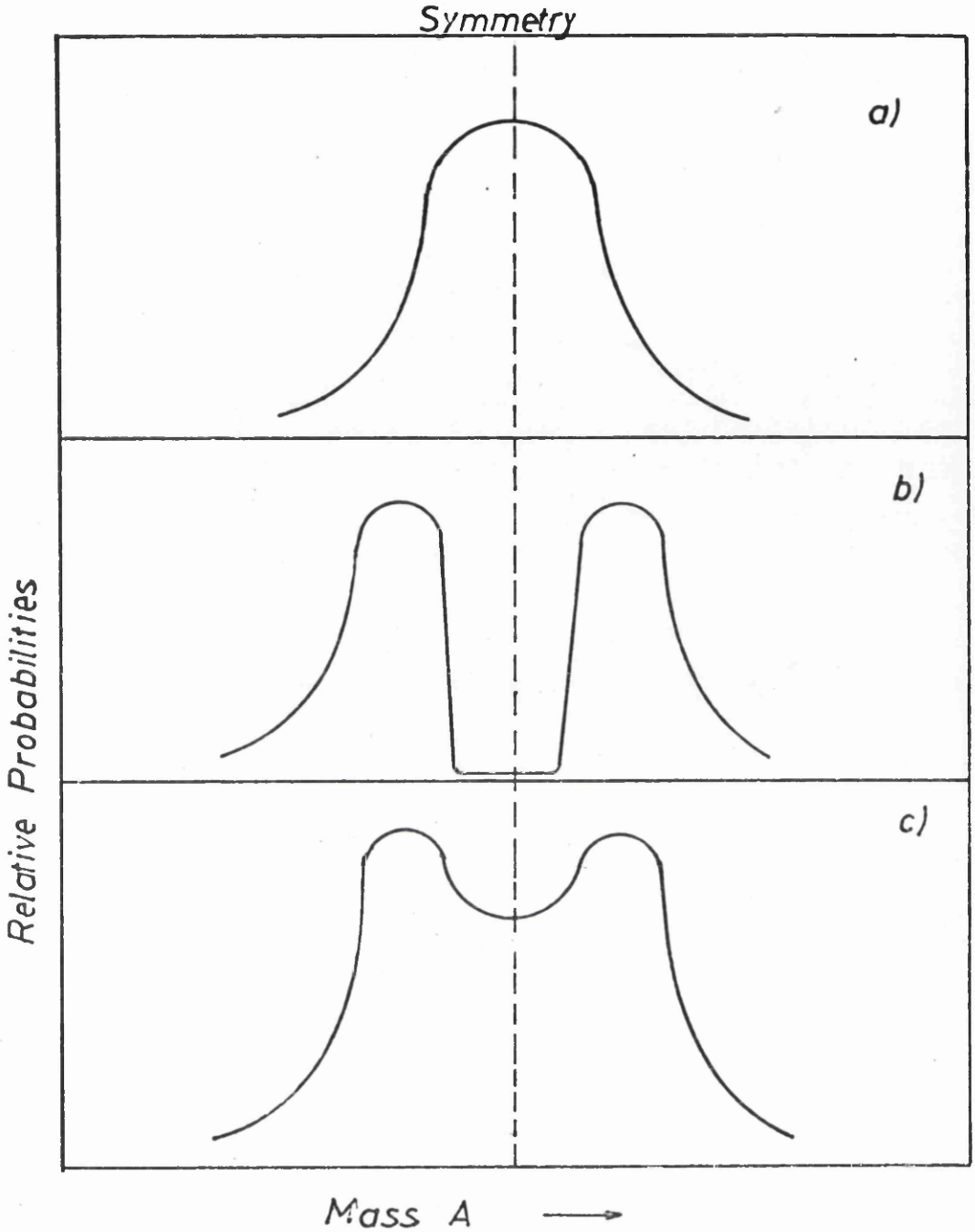

Pict. 2: a) Massdistribution of Fission Fragments
at Direct Interaction
b) at Compound Interaction
c) at Combined Interactions

shows a super-position of the two reactions, as it occurs at intermediate incident neutron energies. The valley at symmetry will be filled up more and more when these energies are increased.

1.4 The Liquid Drop Model

The liquid drop model had primarily been divised to calculate the binding energies of nuclei[4]. It treats the nucleus quasi-classically as a liquid charged droplet. The total energy of this droplet is

$$E_{tot} = E_v + E_s + E_c + \delta + s, \qquad (1.4.1)$$

where

E_v = volume energy
E_s = surface energy
E_c = Coulomb energy
δ = even-odd correction
s = shell correction,

all dependent on the neutron number N and the proton Number Z, as follows[7]:

$$E_v = -c_1 A, \qquad (1.4.2)$$

with

$$c_1 = a_1\left[1 - \kappa\left(\frac{N-Z}{A}\right)^2\right] \qquad (1.4.2.1)$$

where a_1 and κ are constants;

$$E_s = c_2 A^{2/3} f(shape) \qquad (1.4.3)$$

with

$$c_2 = a_2\left[1-\kappa\left(\frac{N-Z}{A}\right)^2\right] \quad , \tag{1.4.3.1}$$

where a_2 is another constant. f(shape) describes the dependence of E_s on the shape of the drop;

$$E_c=\frac{3}{5}\frac{e^2}{r_0}\frac{Z^2}{A^{1/3}}\,g(shape) \quad , \tag{1.4.4}$$

with e,Z and A as usual, $r_o = 1.3\times10^{-13}$ and g(shape) fulfilling a similar function as f(shape);

$$\delta=\pm c_3/A^{1/2} \tag{1.4.5}$$

with c_3 a constant. δ is positive for even-odd, negativefor even-even and zero for odd-mass nuclei, thus respecting the influence of pairing effects on the binding energy. The shell correction will be dealt with in the next subsection of this chapter.

Since only the surface and the Coulomb energy are shape dependent, they together represent the potential energy of the system:

$$V=E_c+E_s \tag{1.4.6}$$

As previously mentioned, their ratio determines their state relative to the fission decay mode. It is therefore useful to define a fissility parameter[7]:

$$x=\frac{E_c}{2E_s} \quad , \tag{1.4.7}$$

where the 2 is there for conventional reasons. x obviously changes

during the deformation process prior to fission and can thus give information about how close a nucleus actually is to fission. But x of course also varies throughout the nuclear table for all the ground states and can be used to calculate fission barriers.

Since the potential energy is combined out of the Coulomb and the surface energy, it is dependent on f(shape) and g(shape) and thus on the deformation of the nucleus. Those two shape functions can be written as

$$f(Y)$$

and $$g(Y) \qquad (1.4.8)$$

where Y means a set of coordinates and can be for instance

$$Y = x, y, z, \Theta, \phi, \psi \quad , \qquad (1.4.8.1)$$

according to pict. 3a, where x,y and z are Cartesian coordinates and Θ, ϕ and ψ are the three Euler angles. For the following, however, it is sufficient to simplify the description of deformations and shapes by using just two coordinates, as in pict. 3b, namely the distance from the centre of mass R and the angle above the horizontal, γ. In that way R can be expressed as

$$R(\mu) = a_0 \left[1 + \sum_{i=1}^{N} \alpha_i P_i(\mu) \right] \quad . \qquad (1.4.9)$$

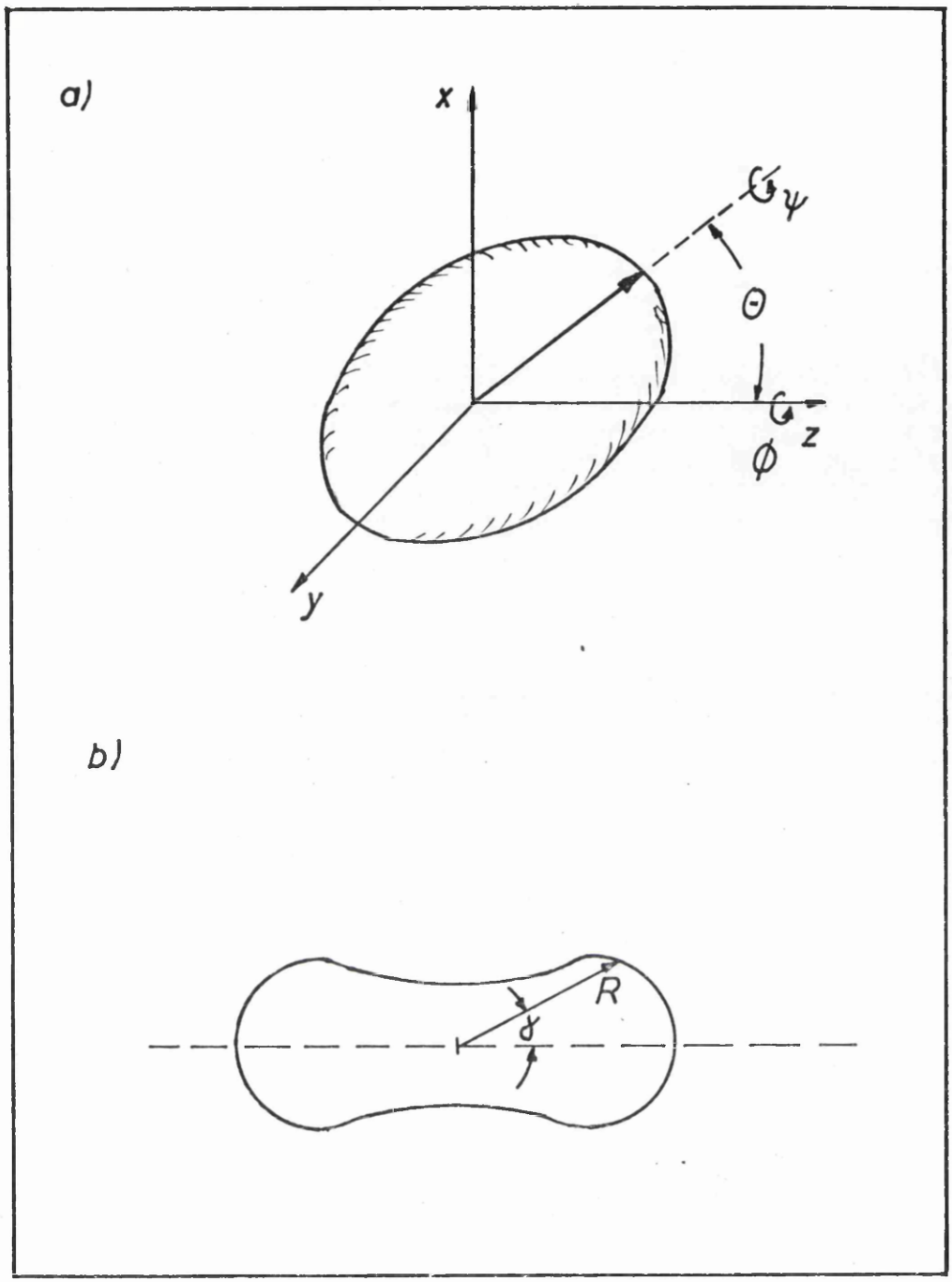

Pict.3: Coordinates of the Nucleus
a) 6 Degrees of Freedom
b) 2 Degrees of Freedom

with $\mu = \cos\gamma$, a_o is a volume normalization constant, $P_i(\mu)$ are the Legendre polynominals with their coefficients α_i . Now it is possible to express f(shape) and g(shape) and thus V in terms of R and γ . But it is also possible to write

$$V = H(\alpha_2, \alpha_4) \quad , \tag{1.4.10}$$

where in this special case α_2 and α_4 are coefficients from (1.4.9). In any case, V can be expressed as a function of deformation.. This is done in the plot in pict. 4, using relation (1.4.10). The graph shows the potential energy surface as a function of the deformation parameters α_2 and α_4 and the dotted line follows a path, which leads from a ground state configuration to fission as shown in pict. 1, which of course, shows the actual shape of the nucleus, also depending on α_2 and α_4 .

It can clearly be seen, that, to reach the fission state, the nucleus has to surpass a saddle on the potential energy surface, which gives this point its name. A bi-dimensional view of the saddle point is given in pict. 5, and the well below the barrier is filled with the bound states of the compound nucleus. The knowledge of the shape parameters of the saddle point structure is essential for cross section calculations. On the other hand, by following the path and its alternatives over the saddle, it is possible to calculate fragment mass and kinetic energy distribution.

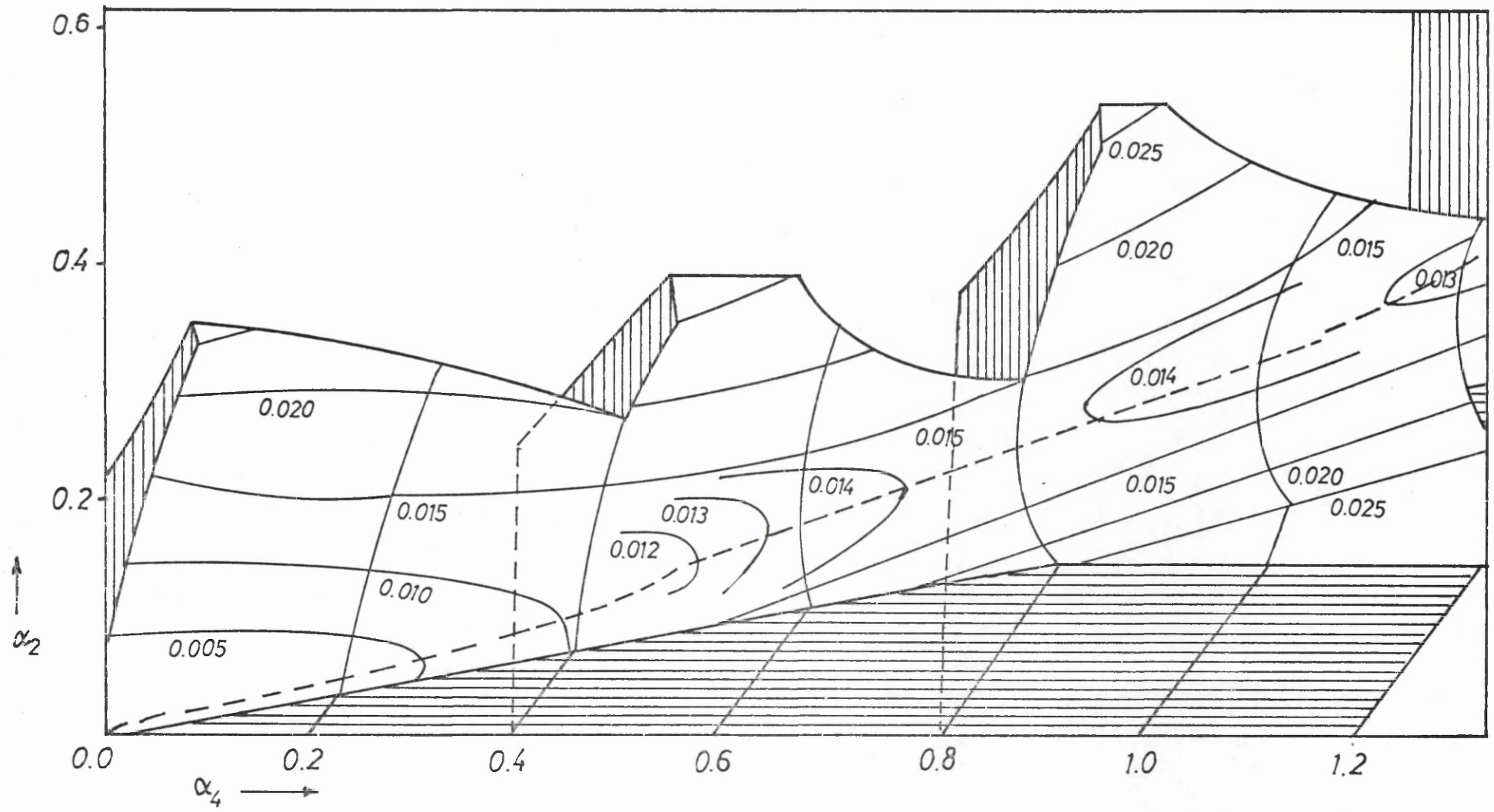

Pict.4: Potential Energy Surface in Dependence of α_2 , α_4 [5]

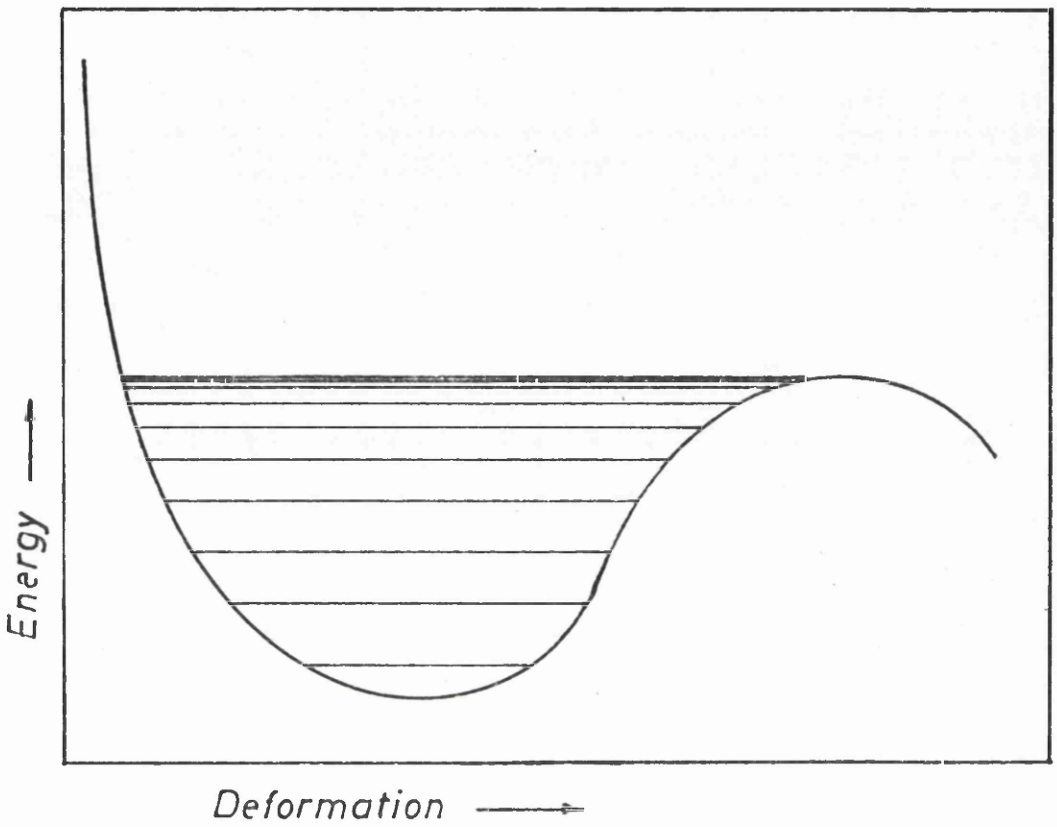

Pict. 5: Fission Barrier (Cross Section)

1.5 Shell Effects

When discussing shell effects, relevant to fission, one has to distinguish between those which are of importance before the fission process, and those, which become important during the event. They will be dealt with in this sequence.

When applying the liquid drop energy formula (1.4.1) for the calculation of nuclear masses without using the shell correction, it takes on the form

$$M(N,Z)=M_n N+M_H Z+E_V+E_S+E_C+\delta\,, \qquad (1.5.1)$$

where M_n is the neutron mass, and M_H is the mass of the hydrogen atom. Calculating the masses throughout the nuclear table [7], an interesting feature is revealed: the deviation of the experimental masses from a smooth liquid drop mass curve shows no uniform trend, but is varying cyclically. Pict. 6 shows this effect qualitatively. There are dips at magic numbers, between which the deviation functions rises, sometimes flattens out and then falls again. To interpret this phenomenon, one has to remember that the liquid drop mass formula in its simple form calculates the ground state masses for a spherical nucleus. W. D. Myers and W. J. Swiatecki conclude that a spherical nuclear potential for the mass numbers, relating to the bumps between magic numbers, would produce degeneracies due to level bunching, with a bunch corresponding to a closed shell. However, when distorting the configuration of these nuclei, the bunching will disappear. We thus have ground state deformations for some nuclei, which are energetically more favourable than the spherical shape.

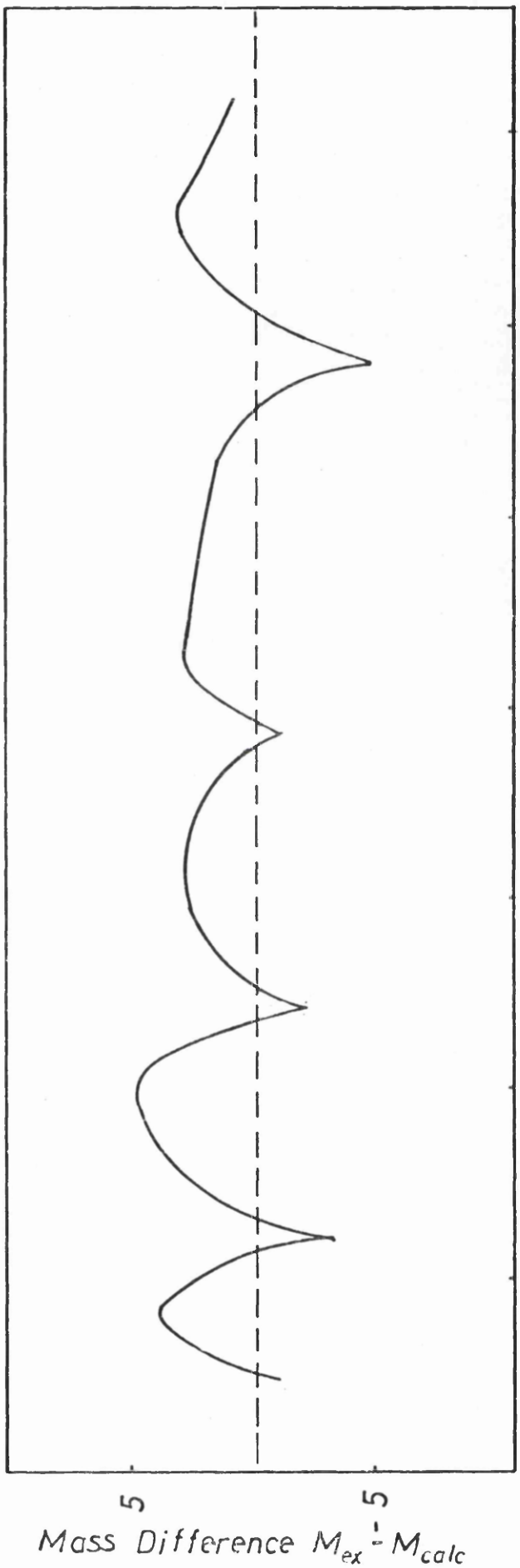

Pict.6: Differences Between Liquid Drop and Experimental Masses [7]

To be able to calculate nuclear masses still with the liquid drop formula, one has to introduce a shell correction, which takes care of the level bunching. The final form of this correction is:

$$S(N,Z)= \frac{F(N)+F(Z)}{(\frac{1}{2}A)^{2/3}} - cA^{1/3} \quad , \qquad (1.5.2)$$

where

$$F(N)=\int_0^N \left[q(n)-n^{2/3}\right]dn \quad , \qquad (1.5.2.1.)$$

$$q(n)=\frac{3}{5}\,\frac{M_i^{5/3}-M_{i-1}^{5/3}}{M_i-M_{i-1}} \qquad M_{i-1}>n>M_i \qquad (1.5.2.2)$$

and F(Z) is similar to F(N). c is a constant, M_i is a magic number.

One can see from pict. 6 that most of the fissionable actinides fall into a bump category, which means, they have stable ground state deformations. This has a serious implication for the shape of the fission barrier, as can be seen from pict. 7, in the case of U-236, where there is a double-hump-barrier. The two minima correspond to stable ground state deformations, one for prolate, the other for oblate shape, whereas at zero deformation an intermediate hump is located, showing an energetically unstable spherical shape. This is similar for most of the fissionable actinides.

The existence of a double-hump potential well can also be deduced from the appearance of spontaneous fission isomers [8], representing

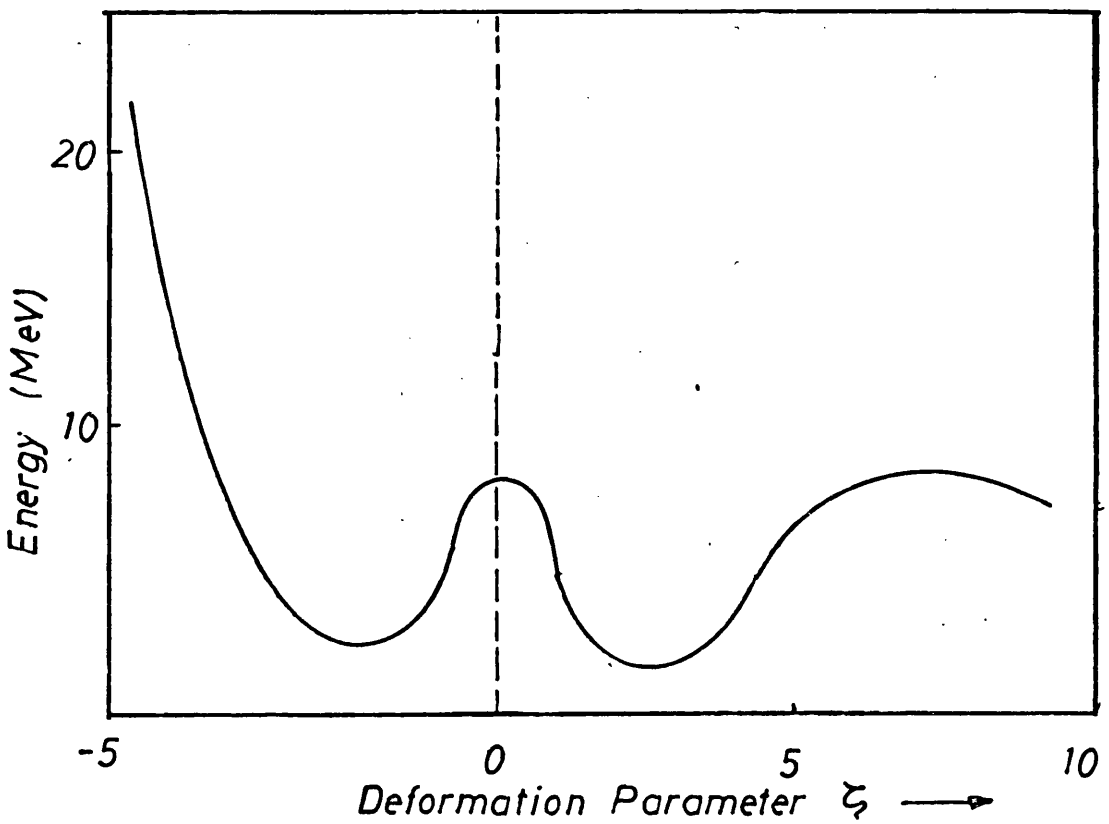

Pict.7: Double Hump Fission Barrier

isomeric ground states for the two minima.

These are shell effects, playing a major role prior to fission.

During the fission process itself, however, other shell effects become relevant when there is a compound reaction. As has been pointed out, in this case one can observe almost always asymmetric fission. Most authors today agree, that this is due to the finite life time of the compound nucleus, during which the future fragments have time to regroup themselves into magic number configurations, sharing the remaining nucleons more or less equally. This latter fact is responsible for the width of the mass distribution of fragments from compound nucleus reactions.

1.6 The Optical Model

The liquid drop model is very useful for calculating the shape of the fission barrier, but for the calculation of a cross section an interaction model is needed, such as the optical model.

When a neutron enters a nucleus, there are two possibilities [10]. Firstly it can maintain its independent particle motion, from which it either re-emerges from the nucleus, or being absorbed, forms a compound nucleus with its target. The second possibility is the immediate absorption, to create a compound nucleus. In either case we have the possibilities of absorption or re-emission. To take these into account, it is useful, to introduce an optical complex potential, the real part describing a potential well and the associated energy states for the

entering neutron, whereas the imaginary part takes care of the absorption effect:

$$U = V(r) + iW(r) \,, \tag{1.6.1}$$

where r is a coordinate.

With this potential the Schroedinger equation is:

$$\nabla^2\psi + \left[k^2 - U^*(r)\right]\psi = 0 \,, \tag{1.6.2}$$

with

$$k^2 = \frac{2\mu}{\hbar^2} E \,, \tag{1.6.2.1}$$

and

$$U^*(r) = \frac{2\mu}{\hbar^2} U(r) \tag{1.6.2.2}$$

where μ is the reduced mass, and E is the energy, $\hbar$ as usual.

The general solution of this equation is

$$\psi = \sum_{l=0}^{\infty} B_l f_l(kr) P_l(\cos\Theta) \,, \tag{1.6.3}$$

with $P_l(\cos\Theta)$ a Legendre polynomial and f_l being the solution of the radial equation. B_l can be determined by looking at the asymptotic

behaviour:

$$\psi \xrightarrow[r\to\infty]{} e^{ikz} + f(\Theta)\frac{e^{ikr}}{r} \qquad (1.6.4)$$

is the sum of the plane and spherical wave functions. The plane part can be described by spherical coordinates and becomes:

$$e^{ikz} = \sum_{l} i^{l}(2l+1) j_l(kr) P_l(\cos\Theta) \qquad (1.6.4.1)$$

where j_l is a spherical Bessel function. Comparing the radial equation for f_l

$$\frac{d^2 f_l}{dr^2} + \frac{2}{r}\frac{df_l}{dr} + \left[k^2 - U^*(r) - \frac{l(l+1)}{r^2}\right] f_l = 0 \qquad (1.6.5)$$

and that for the latter function

$$\frac{d^2 j_l}{dr^2} + \frac{2}{r}\frac{dj_l}{dr} + \left[k^2 - \frac{l(l+1)}{r^2}\right] j_l = 0 \qquad (1.6.6)$$

leads to the only difference between them, as being U*(r). So the asymptotic form of both should differ only by a phase shift δ_l, due to the potential, if that goes to zero with large r. The asymptotic behaviour of the Bessel function is

$$j_l(kr) \longrightarrow \frac{1}{kr}\sin(kr - \frac{1}{2}l\pi) \qquad (1.6.7)$$

and that of f_l is

$$f_l(kr) \longrightarrow \frac{1}{kr}\sin(kr-\frac{1}{2}l\pi+\delta_l). \tag{1.6.8}$$

B_l and $f_l(\theta)$, known as the scattering amplitude, can be obtained by comparing (1.6.3) with (1.6.4), and similarly for e^{ikz}. This leads to

$$B_l = i^l(2^l+1)e^{i\delta_l} \tag{1.6.9}$$

and

$$f(\theta)=\frac{1}{2ik}\sum_l (2l+1)(e^{2i\delta_l}-1)P_l(\cos\theta). \tag{1.6.10}$$

The total cross section can now be expressed as

$$\sigma = 2\pi\int_0^\pi |f(\theta)|^2 \sin\theta\, d\theta \tag{1.6.11}$$

which can finally be reduced to

$$\sigma=\frac{4\pi}{k^2}\sum_l (2l+1)\sin^2\delta_l. \tag{1.6.11.1}$$

This deduction can all be described as basic scattering theory[10], valid for any potential. To introduce an optical parameter, it is neccessary, to look again at the asymptotic behaviour of the scattering wave function. This can be written in terms of the phase shift factor δ_l as

$$\psi \longrightarrow \frac{-i}{2kr} \sum_l i^l (2l+1) P_l(\cos\theta) \left[e^{2i\delta_l} e^{i(kr-\frac{1}{2}l\pi)} - e^{-i(kr-\frac{1}{2}l\pi)} \right] \qquad (1.6.12)$$

or

$$\longrightarrow \frac{1}{2} \sum_l i^{l+1} (2l+1) P_l(\cos\theta) \left[\mathcal{J}_l(kr) - \eta_l \mathcal{O}(kr) \right] \qquad (1.6.12.1)$$

with $\mathcal{J}$ for the incoming and $\mathcal{O}$ for the outgoing wave and η_l being a reflection coefficient, defined as

$$\eta_l = e^{2i\delta_l} . \qquad (1.6.12.2)$$

The meaning of η_l becomes clear, when interpreting it in optical terms:

if $\eta_l = 1$, there will be 100 % reflection. It will be < 1 in proportion to the relative amount of absorption in a given incident flux and becomes 0 for complete absorption. Thus the various cross sections can be expressed as follows:

$$\sigma_{sc}=\frac{\pi}{k^2}\sum_l (2l+1)\left|1-\eta_l\right|^2 \qquad (1.6.13)$$

for elastic scattering,

$$\sigma_{abs}=\frac{\pi}{k^2}\sum_l (2l+1)(1-\left|\eta_l\right|^2) \qquad (1.6.14)$$

for absorption, and

$$\sigma_{tot}=\frac{2\pi}{k^2}\sum_l (2l+1)(1-Re\,\eta_l) \qquad (1.6.15)$$

for the total cross section. Considering the absorption cross section, one can define a transmission coefficient

$$T_l=1-\left|\eta_l\right|^2 \quad , \qquad (1.6.16)$$

which gives, in optical terms, the penetrability of a nucleus. The optical model with its complex potential can be used to calculate these transmission coefficients.

1.7 The Statistical Model

When considering a cross section, its principal variation with energy can be divided into two regions[11]. Firstly, there is the low energy part, which can consist out of sequences of many resonances. However, moving up to higher energies, the width of the resonances becomes such, that the resonances themselves overlap and thus are no longer distinguishable from each other. We are in the continuum region,

and the cross section is a smooth function, varying with energy. Coming back to the resonance region, one can take an energy interval $\triangle E$ and average the cross section over it. Such a description does not include the rapidly varying shape of the cross section in the resonance region, but leads to a gross structure, which presents the cross section as a slowly fluctuating function with energy. The statistical model can be used [12], to elaborate on the average cross section, including both the low and high energy regions.

The optical model gives a formula for the cross section in terms of a transmission coefficient:

$$\sigma_c^l = \frac{\pi}{k^2}(2l+1)T_l(E) , \tag{1.7.1}$$

in this example for the formation of a compound nucleus. To have a spin J can be expressed by the square of the Clebsch-Gordan coefficient. This is the probability for forming a compound state with spin J and incident neutron angular momentum l.

$$P_{l,J} = |lj;0m|lj;Jm|^2 , \tag{1.7.2}$$

where j denotes the channel spin of the combined neutron-nucleus system. This gives a cross section

$$\sigma_c^l |(lj;0m|lj;Jm)|^2 = \frac{\pi}{k^2}(2l+1)T_l(E)|(lj;0m|lj;Jm)|^2 . \tag{1.7.3}$$

In more general terms, when looking for example at an elastic reaction, this has to be multiplied by another probability, taking into account this particular reaction.

$$\sigma(l,j|l',j'|\vartheta)=\frac{\pi}{k^2}(2l+1)T_l(E)$$

$$\times\sum_J \frac{A_J(l,j|l',j'|\vartheta)}{1+\sum_{p,q,r}' T_p(E_q')/T_{l'}(E')} \quad , \tag{1.7.4}$$

where the outgoing neutrons have angular momentum l', the final channel spin is j' and the direction of the scattered neutrons is described by the coordinate ϑ .r and p refer to possible competing outgoing channel spins and neutron angular momentum and E' to competing corresponding neutron energies. A_J is $_q$

$$A_J(l,j|l',j'|\vartheta)=\sum_{m,m'}|(lj;0m|lj;Jm)|^2$$

$$\times|(l',j';m',m-m'|l'j';Jm)|^2\,|Y_{l',m}(\vartheta,\varphi)|^2. \tag{1.7.4.1}$$

Since (1.7.4) refers to a single energy level, to obtain the cross sections for all energies and neutron angular momenta, one has to integrate and apply the neccessary sum rules. This leads finally to the cross section for the general reaction (i/i') with original nucleus spin i and final spin i':

$$\sigma(i/i')=\frac{\pi}{k^2}\frac{1}{(2i+1)}\sum_l T_l(E)$$

$$\times\sum_J \frac{\varepsilon^J_{j,l}(2J+1)}{1+\sum_{j'',l'';q}\varepsilon^J_{j'',l''}T_{l''}(E_q')/\sum_{l',j'}\varepsilon^J_{j',l'}\cdot T_{l'}(E')} \quad , \tag{1.7.5}$$

where $\varepsilon^{J}_{j,l}$ = 2,1 or 0, for the cases: both j_1 and j_2,
: j_1, or j_2, (not both)
: neither j_1 or j_2

satisfy $|J-I| \leqslant j_i \leqslant (J+I)$, (1.7.5.1)

with

$$j_{1,2} = i \pm \frac{1}{2} \tag{1.7.5.2}$$

and the doubly primed parameters notate competing reactions. Very generally an average reaction cross section can be written as[9]

$$\overline{\sigma_{cc'}} = \frac{\pi}{k^2} g(J,I) \frac{T_{(c)} T_{(c')}}{\sum_{c''} T_{(c'')}} , \tag{1.7.6}$$

where g (J,l) stands for the statistical factor, composed out of J and l. In the special case of fission, this leads to

$$\sigma_{n,f}(E) = \frac{\pi}{k^2} \sum_{J} \sum_{j=i-\frac{1}{2}}^{j=i+\frac{1}{2}}$$

$$\sum_{I=J-j}^{I=J+j} \frac{g(J,I)\, T_{J^\pi(I,j)}(E)\, T_{J^\pi(f)}}{T_{J^\pi(f)} + T_{J^\pi(\gamma)} + T_{J^\pi(n,tot)}} , \tag{1.7.7}$$

with $T_{J^\pi\,(f)}$ for the fission, $T_{J^\pi\,(\gamma)}$ for the neutron capture gamma-ray and $T_{J^\pi\,(n,tot)}$ for the total scattering transmission

coefficients and $T_{J^{\pi}(l,j)}$ for the entering neutron transmission coefficients. Chapter V will deal with the detailed calculations of these coefficients.

1.8 Present State of Experimental and Theoretical Work and Future Trends

The fission cross sections of actinide nuclei, especially Uranium isotopes, have been measured frequently and with increasing accuracy. Some examples are measurements by E. Pfletschinger and F. Kaeppler[13], W. P. Poenitz[14], W. P. Poenitz and R. J. Armani[15], J. W. Meadows[16], and G. D. James[17,18]. There exist also several reviews and evaluations presenting a picture of the validity of past measurements and the present state of the experimental work. A very elaborate and relevant evaluation is the one by M. G. Sowerby et al.[19], being the most recent at the time of starting this present experimental undertaking.

A careful study of the past experimental work reveals, that in spite of the frequency of measurements, there are several shortcomings; firstly, most measurements carried out so far are ratio measurements rather than absolute ones. Secondly, the fission cross section of U-235 is very well known only below 0.5 MeV. The low energy region of course, was primarily of interest for thermal fission reactor design and has therefore been studied exhaustively. The general shape of this cross section and of the one for U-238 between 1 and 10 MeV is fairly well known, although there still exists a number of discrepancies among different experiments. Also, the energy resolutions seem to be rather poor over this range. Above 10 MeV the statistical

accuracy is also poor, and there are are large fluctuations among different authors. These facts prevented the observation of any structure yet.

For these reasons it was therefore necessary to remeasure the fission cross sections of U-235 especially and U-238, and to gain more accuracy by doing so. Firstly, the subthreshold study of these isotopes is particularly interesting from the point of view of the doubly shaped fission barrier, predicted by some authors [7,8]. This should show up as structure in the cross section. On the other hand, the fast fission cross section between 1 and 10 MeV has to be known more accurately for multigroup reactor dynamics calculations for fast breeder reactors, being developed at present.

Future experiments would almost certainly include the measurements of fission cross sections for super-heavy nuclei with the present method, which has been proved successfully for the Uranium isotopes. This is of considerable interest for core-criticality calculations for any nuclear reactor and also to some extend for nuclear waste management, apart from the pure scientific interest.

There are also a number of refinements for measuring fission cross sections with more accuracy. One such method is the method of threshold cross sections, described in detail by J. W. Behrens [21].

Considering the field of fission, it is inevitable to look beyond the scope of cross sections alone. To identify any resonances in fission cross sections positively, a coincidental measurement

of angular distribution of fragments is neccessary. Together with fragment mass distribution measurements, a more complete picture of the fission mechanism could be developed.
Another very interesting development is the investigation of the BNG mode of decay of fission fragments, meaning the subsequent decay via a beta particle, a delayed neutron and a gamma ray. Investigation of this process is already in progress [22].

In the field of theoretical cross section calculations for fission, there is little experience up to date. All the relevant systematics are described by J. E. Lynn [9]. Improvements can be made by refining the optical model parameters, to calculate the incoming and total scattering transmission coefficients for high A nuclei. A better experimental knowledge or more advanced liquid drop model calculations can lead to a better parametrization of the barrier shapes and thus to more realistic theoretical fission cross sections in future.

CHAPTER II

2.1 Introduction

The principal instruments to do neutron-time-of-flight work were well established in the Kelvin Laboratory, and so was a lot of experience with the 100 MeV electron linear accelerator as the pulsed neutron source. This is also true for the neutron flux monitors. However, to develop a detection system for fission-time-of-flight work with neutrons, yielding the required good time resolution, it was neccessary to turn to a previously in this laboratory not used detector, a gas scintillator.

This second chapter will firstly describe the established instrumentation in connection with the accelerator and give a view over the principal time-of-flight technique in connection with fission cross section measurements, involving the use of the gas scintillator. It will then proceed to describe the development of this scintillator, starting with the basic gas scintillation processes for particle detection. This leads to the special case of Xenon, used for this specific scintillator, and the influence of certain physical parameters, such as pressure, on the performance of the gas. After that the design of the gas chamber and the attached vacuum system will be described. Special emphasis was laid upon cleanliness and stability of the detection system. A series of tests with a Cf-252 natural fission source were performed, to adjust the optimum conditions for fission detection. This source was of course later replaced by Uranium target foils in a certain geometry to the attached photomultipliers

and the neutron beam. The influence of magnetic fields on the photo-tube and electric field effects on the gas were investigated and eliminated.

The two final subsections of this chapter will deal with the monitor detectors and the reduction of after-pulsing, due to the γ -flash which precedes the pulsed neutron beam.

2.2 The Linear Accelerator of the Kelvin Laboratory as a Pulsed Neutron Source

As described by G. I. Crawford et al.[24] the Kelvin Laboratory 100 MeV. electron linear accelerator (LINAC) can be used as a pulsed neutron source. Electrons are injected from an electron gun at an energy of 30 keV through a set of deflection plates, across which a 10 kV pulse is applied to give a 3.5 ns wide pulse, before entering the first of three accelerator sections. The final beam current at the end of the accelerator is between 50 and 100 mA, depending on the selected electron energy and the pulse repetition rate, the latter typically 600 pps. In principle the beam may enter one of three different beam lines after leaving the beam deflection system, a set of dipole magnets: at 0^{o}, 45^{o} and 90^{o}. Since for neutron-time-of-flight experiments an exact knowledge of the energy of the electron beam is not required, the commonly used beam line is the 0^{o} line, applying no deflection onto the beam.

The beam then enters the neutron cell, hitting a neutron production target. Pict. 8 shows the basic layout of the front section of the accelerator system, used for neutron work. The beam can be focused onto the neutron production target by a set of quadrupole magnets.

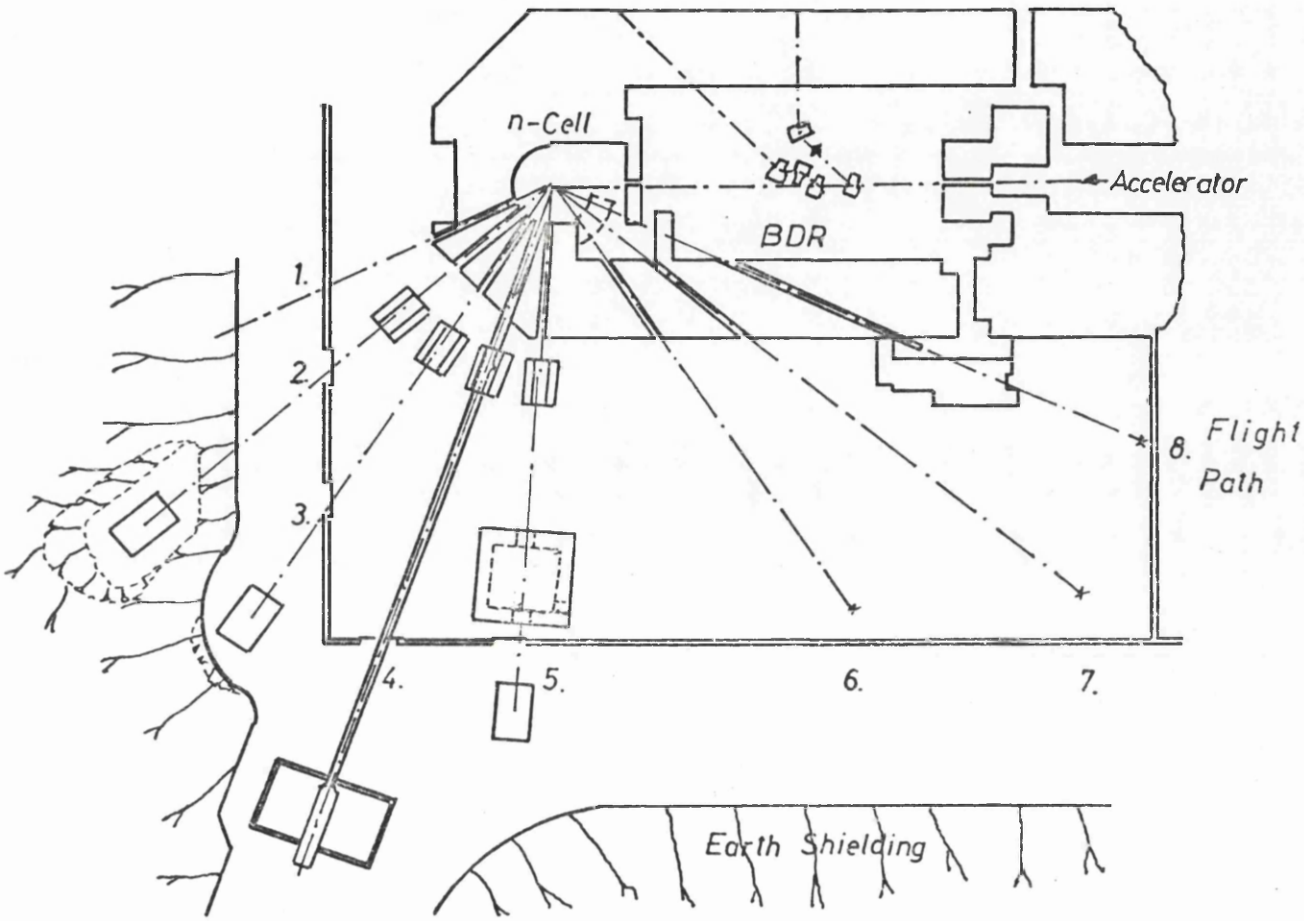

Pict. 8: Front Section of the 100 MeV LINAC

In front of the target there is a scintillation screen, painted with Zns, to show the beam spot, which is observed by a closed circuit TV-camera. Typical diameters of the circular cross section beam are between 1.0 and 1.5 cm. For neutron production the electron energy is of the order of 100 MeV.

The neutron production target is preferably a rod of high Z material, either natural Pb or U. In the presented experiments Pb was used. It was cast into a stainless steel tube, closed at the bottom end, because the Pb melts under the heat, dissipated by the high energy electrons in the target. When the electrons are stopped by the Coulomb potential of the Pb atoms, they produce high energy bremsstrahlung. Part of the bremsstrahlung quanta cause neutron emission from the Pb nuclei by (γ,n) reactions. The resultant neutron spectrum is of Maxwellian type, ranging from about 0.5 to 10.0 MeV and peaking at about 2.0 MeV.

The accelerator and of course also the neutron cell are surrounded by concrete shielding. This shielding is interrupted by 8 flight tubes at different angles and at the level of the electron beam and the production target. The diameter of these tubes is typically 20 cm, and the tubes can be equipped with different kinds of collimators. Most of the tubes enter the Kelvin Laboratory North Experimental Hall, though the 70^{o} tube enters into a 100 m evacuated flight path with further detector stations at 25 m and 50 m.

2.3 Measurement of Fission Cross Sections, Using a Gas Scintillator and the Time-of-Flight Technique

When using the time-of-flight technique, the time, a particle of known mass travels over a certain distance, is measured. Knowing that distance, the kinetic energy of the particle can be calculated. The measurement of the flight-time is usually done by a time-to-amplitude converter (TAC), which has to have a start pulse generated at the beginning of the flight path and a stop pulse produced at the end position.

In the case of the flux created in the neutron production target in the neutron-cell, the electron beam produces a start pulse, when passing through a toroid just in front of the target, as can be seen from pict. 9. After origination the neutrons travel through the collimater along the flight-path, until they reach a monitor detector, usually a plastic-scintillator-photomultiplier-system. The detection signal in this detector serves as a stop pulse. The output of the TAC, being proportional to the flight-time and inversely to the neutron energy, is then fed to a multichannel analyzer, which stores the incident neutron spectrum, according to the different times of arrival of the neutrons at the monitor detector. In this way the incident neutron flux is measured as a function of energy.

In front of the monitor is the main detector, a gas scintillator, which provides very little attenuation to the flux. Inside the gas-chamber is the fission target, a thin layer of the isotope under investigation. When an incoming neutron produces fission, in most cases one fragment escapes out of the foil into the surrounding gas, where it creates a scintillation pulse. This pulse is seen by the attached photomultiplier and again serves as a stop pulse for another TAC, which got its start

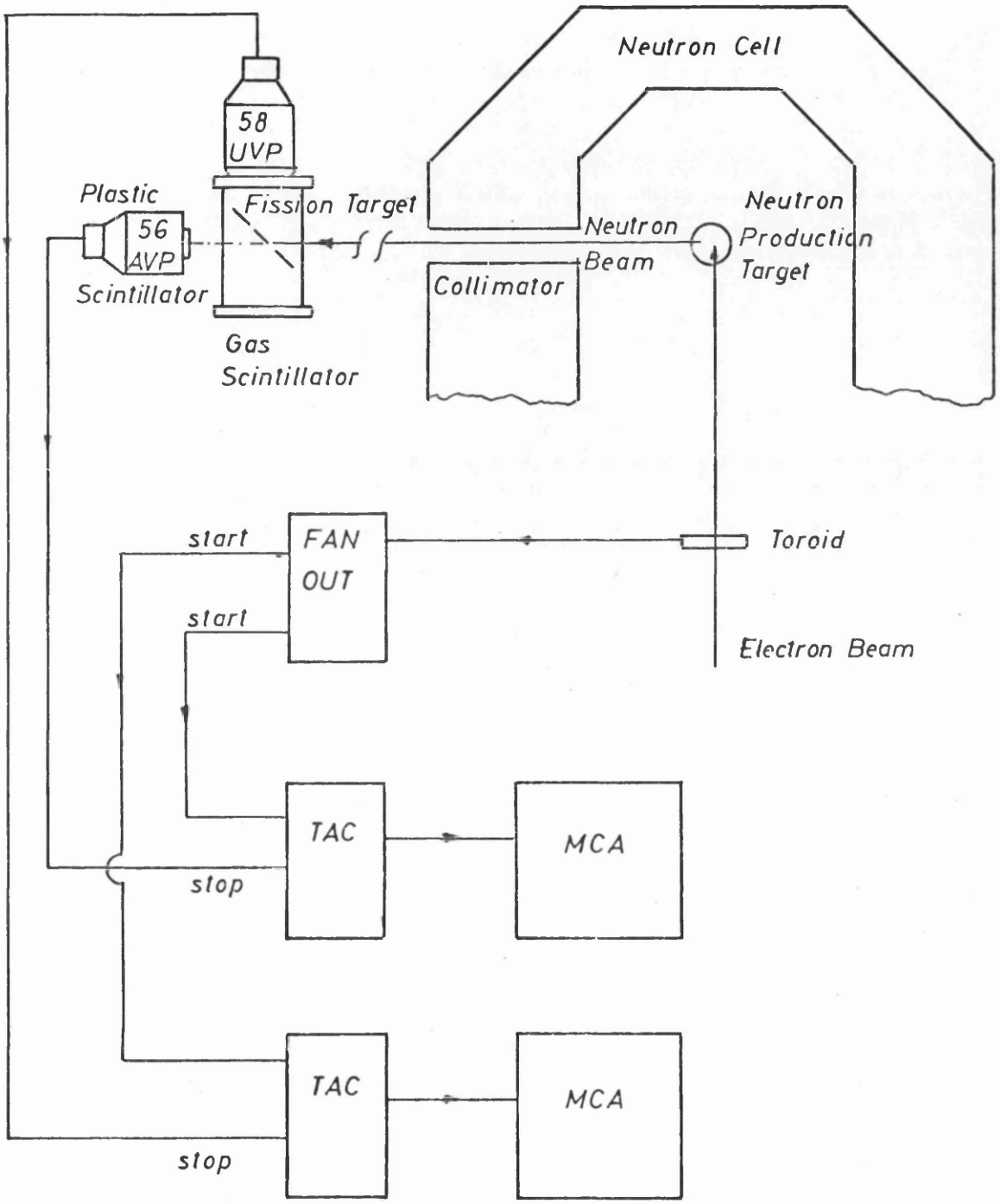

Pict. 9: Setup For a Time-of-Flight Measurement of Fission Cross Sections

pulse also from the already mentioned toroid. The output of this second TAC is fed into a different multichannel analyser, to store a spectrum of the neutrons, creating fission. From those two accumulated spectra it is, in principle, possible to derive the fission cross section.

From the above it can already be seen, that there are two main factors, which contribute to the energy resolution of the system: the length of the flight path and the time response of the detectors. The latter fact already limits the variables for the design of the gas scintillator.

2.4 Choice of a Gas Scintillator, and Its Basic Mechanism

When choosing a fission detector, suitable to be used in the time-of-flight arrangement as described in the previous subsection, the following requirements have to be met:

1. Separation of fission events from other reactions.
   The main alternative reaction is the emission of α-decay products from a target foil. A good separation, according to particle mass, to distinguish α's from fission fragments, can be achieved in a gas scintillator. This is because of the low ionization densities along the scintillation path of these ions, which prevents saturation of the pulses from fission fragments. Therefore the relative pulse height correctly represents the relativ energies of α's and fission fragments.
2. Insensitivity to total energy of γ-flash.
   A gas scintillator would show a reduced sensitivity to the γ-flash, preceding the neutron flux from the bremsstrahlung target, because of its low density, thus reducing interaction probabilities with

γ -rays.

3. Fast pulse, to achieve good timing resolution.

Looking at the various decay times of different gases makes Xenon an obvious choice with 7.1 ns as the shortest one.

4. Achievement of 4π-or 2π-geometry.

This can be achieved with a gas scintillator easily, since a target could be incorporated in it directly.

The principles of scintillation counting in general and of gas scintillators in particular have been presented well by J. B. Birks [25]. It is found, that the scintillation output of gaseous scintillators ranges from the vacuum ultraviolet (UV) to the lower limit of the visible spectrum, but in inert gases it remains mainly in the UV-region with very short decay times for the scintillation pulses. Other favourable properties are volume flexibility and control of the pulse amplitude by the pressure.

Different gases of course have different qualities, and the choice is basically among Helium, Neon, Argon, Krypton, and Xenon, although Carbon-Tetrafluoride has been used [26], and the adding of Nitrogen, to shift the UV-wave length into the visible region, is often practised. Various authors also use mixtures, combined out of the noble gases. Although the scintillation process in detail is rather dependent on the gas or the mixture, the basic mechanism is the same for all. To investigate it, one has to look at the reactions with heavy charged particles, such as α-particles or fission fragments, escaping from the source inside the gas.

After such a particle has left the source, it will travel a certain distance in the gas, depending on the pressure, until it is in equilibrium with its environment. This is typically of the order of 1 cm in He at a pressure of about 1 at, depending on the initial fragment energy, of course [27]. While travelling this distance, the particle loses all its initial kinetic energy, according to Bohr's classical theory:

$$\frac{dE}{dx} = \frac{4\pi e^4 Z_{eff} Z_2 N}{mv^2} \ln \frac{1.123 mv^2}{I Z_{eff} v_0} , \qquad (2.4.1)$$

where dE/dx is the energy loss per unit distance, Z_{eff} is the effective charge of the particle, Z_2 is the total number of electrons of the stopping atom, N the number of atoms per unit volume, m the mass of the particle, v its velocity, v_o the velocity of an electron in the first Bohr-orbit and I the ionization potential of the outer shell electrons of the medium. There are now a considerable number of simil-ar refined calculations available [27,28,29].

Along the path of the fragment surrounding atoms or molecules are excited by atomic collisions with the particle, and their subsequent de-excitation produces the scintillation pulse, which can be observed by a photomultiplier, for example. There are, however, several possibilities of excitation and subsequent de-excitation in noble gases [30]. Simple de-excitation is like

$$X^* \longrightarrow X + h\nu . \qquad (2.4.2)$$

Another possibility is an exchange reaction

$$X^* + X \longrightarrow X + X^* \qquad (2.4.3)$$

in interatomic collisions. The third possibility is the creation of an ionized molecule:

$$X^* + X \longrightarrow X_2^+ + e^- . \qquad (2.4.4)$$

There is also the possibility of impurities or wave-length shifter, taking the place of the partner-atom in interatomic collisions. Multiple atom-collisions with more than one partner are also possible. This appearance of several competing reaction channels explains the absence of strong atomic lines in the scintillation spectrum of noble gases.

2.5 Properties of Xenon

Xenon is a noble gas, and therefore it does not react chemically with any other material, from which for instance a scintillator enclosure may be made. Comparing it with any other inorganic scintillator, be it of gaseous, liquid or plastic type, its outstanding advantage in relation to timing resolution in a time-of-flight experiment is its extremely short decay-time of only 7.1 ns [31] in the fast component, as shown in pict. 10. The energy transfer to and de-excitation of the Xenon atoms can be described by the three reactions:

$$2Xe + Xe^* \longrightarrow Xe_2^{**} + Xe \qquad (2.5.1)$$

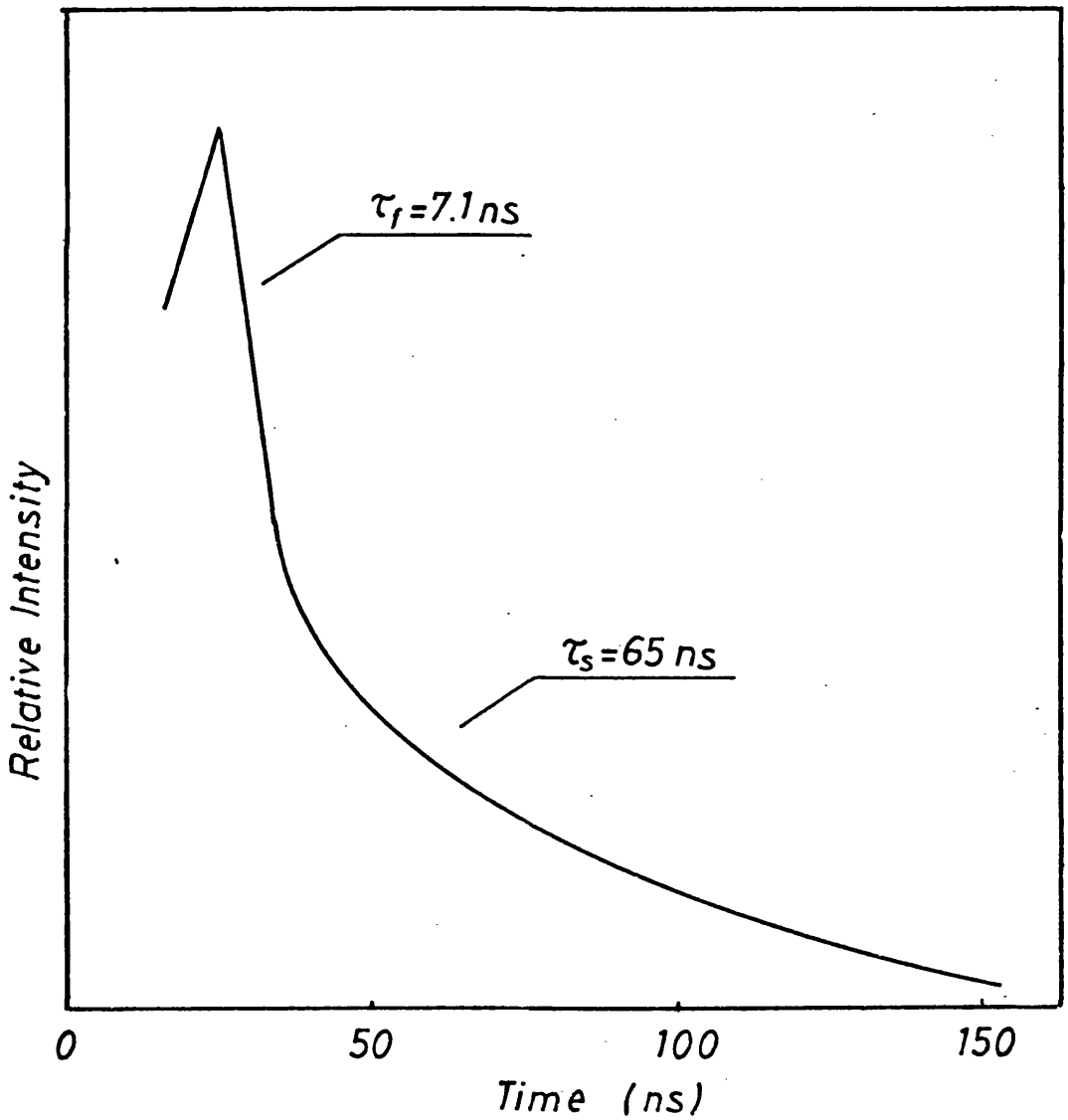

Pict.10: Scintillation Response in Xenon [31]

$$2Xe + Xe^{*} \longrightarrow Xe_2^{*} + Xe^{*} \qquad (2.5.2)$$

$$Xe_2^{**} \longrightarrow Xe_2^{*} + h\nu \qquad (2.5.3)$$

The principal portion of the light emitted, lies below 200nm wave length. This necessitates a quartz window for the construction of the scintillator and a quartz-faced phototube for observation.

2.6 Influence of Pressure, Chamber Geometry and Impurities

In the previous section of this chapter it has already been mentioned, that the scintillation response in Xe consists of two components: a fast and slow one. According to V. I. Lyashenko et al.[32], the fast component lies in the vacuum-UV-range, whereas the slow component contributes to the visible range. However, the ratio of their intensities varies with pressure. Pict. 11 shows the dependence of the decay time of the slow component τ_s on the Xe pressure. The fast component comes mainly from atomic resonance excitation[33], whereas the slow component is attributed to meta-stable levels of excited ions. The recombination time of these ions of course depends strongly on the pressure and temperature of the gas. The chance of recombination decreases with decreasing pressure, and the proportion of the slow component intensity thus increases relative to the fast component. However, this proportion only becomes significant below about 300 torr. At this stage the increase in de-excitation time of the slow component itself is so substantial, that Xe now has become a slow scintillator.

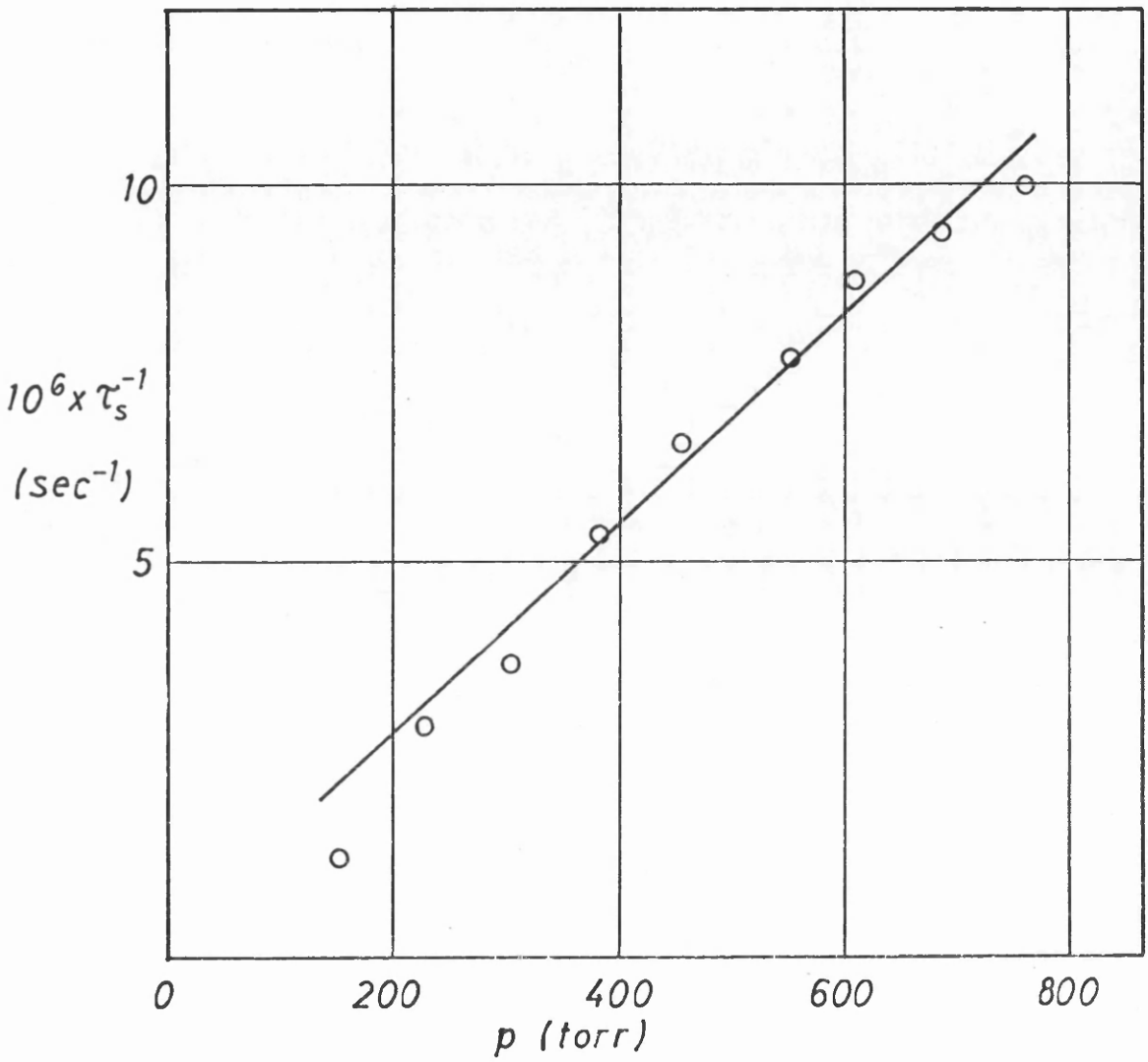

Pict. 11: Dependence of τ_s^{-1} on Xenon Pressure[32]

Another feature is the variation of pulse height for a given particle with a given incident kinetic energy due to varying pressure [34], and the effect of this on the pulse height resolution of the system. A detailed investigation of these effects will be described in section 11 of this chapter.

The observed pulse amplitude by a photomultiplier is also critically dependent on size, geometry and surface of the scintillator enclosure [31]. The size of the detector and the position of the photomultiplier determines the amount of light absorbed by the medium itself at a given pressure. Pict. 12 illustrates this effect. The geometry determines, how often the light is reflected, until it reaches the photocathode. It is therefore advantageous in terms of optical efficiency to have the simplest possible chamber, for instance a cylinder. The state of the surface of course contributes to the light collection efficiency in respect to its ability to deflect as much light as possible and absorb as little as possible. It therefore has to be polished.

Some gas scintillators will only give an output, when there are impurities in the form of Nitrogen present, for example Helium. Nitrogen, as has been pointed out before, can also be used as wave length shifter, and already a small fraction of it provides enough intermolecular collisions to be able to rely entirely on the visible output of the scintillator. However, since this sort of reaction involves at least one, possible two more subreactions after the first excitation of a Xenon atom, it will stretch the over-all decay time of the pulse, which cannot be tolerated if fast timing is

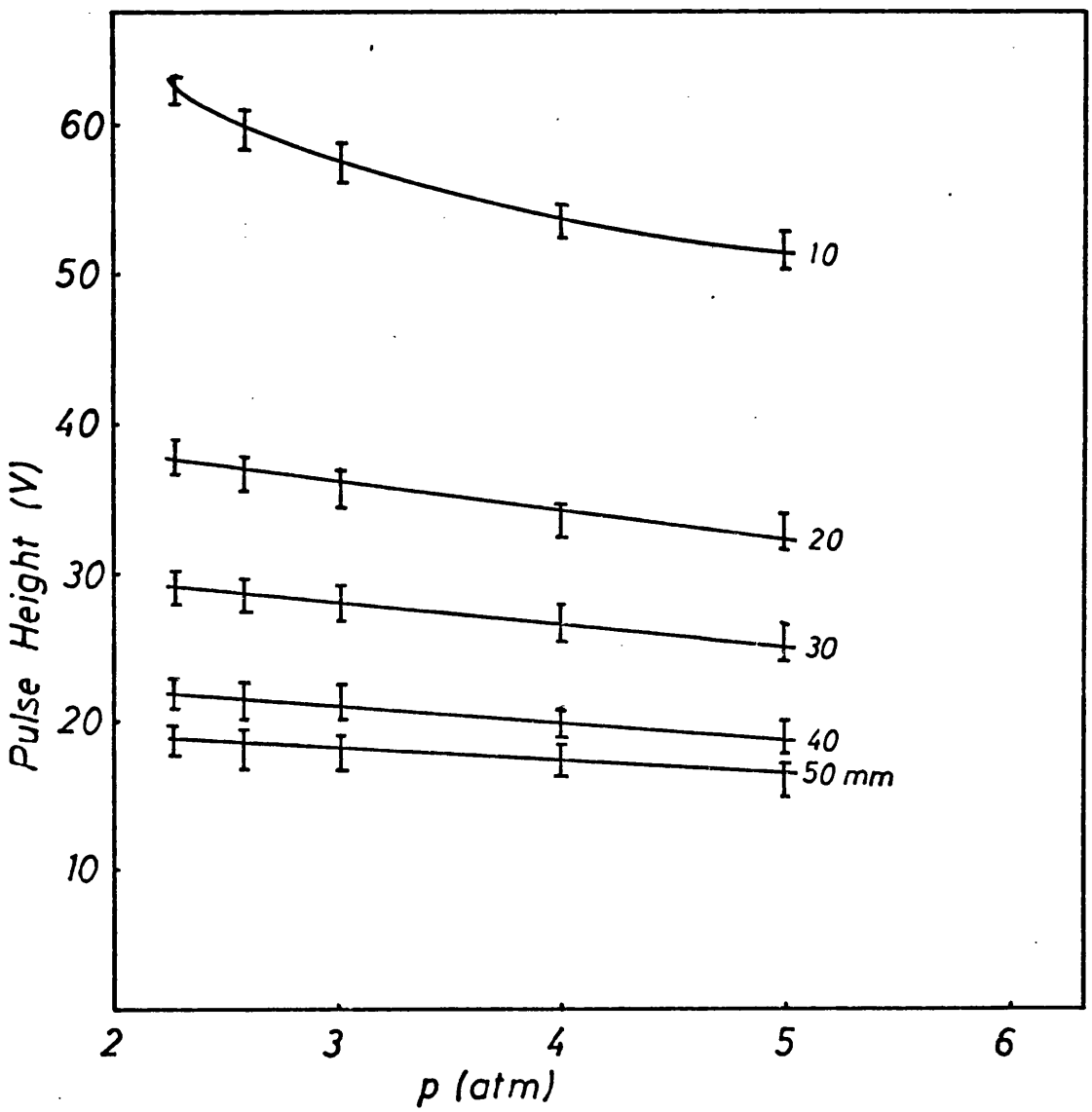

Pict.12: Pulse Height Versus Pressure For Gas Scintillation Chambers With Constant Diameter and Heights From 10 To 50 mm [31]

desired. It is therefore neccessary to dispose in this case of all impurities, especially of organic compounds, in the system.

2.7 Design of the Scintillation Chamber

Pict. 13 shows the detailed design of the Xe gas scintillation chamber . Its main body consists of a stainless steel tube of about 10 cm diameter and with a wall thickness of 12 thou", to provide as little attenuation to the incoming neutron flux as possible. There are also two stiffening ribs, rolled coaxially into the tube, to make it rigid against deformation under pressure. Welded onto the ends of the tube, which suspends to about 15 cm in length, are two 1 cm thick stainless steel flanges, which have holes to take 6 bolts each. These flanges have a 1 mm x 1 mm groove on their outside surface to take an Indium seal. Indium is used for sealing, because it is a soft metal, and rubber or plastic seals would outgas under vacuum and thus contaminate the system. Onto each flange a quartz qindow, a 1 cm thick disc, can be fixed with the help of Tufnol flanges, matching those at the chamber body. Between the Tufnol flanges and the quartz window is a rubber seal, to even out pressure irregularities, due to different tensions on the six fastening bolts on each side. The thickness of the quartz disc had to be not less than 1 cm, to sustain at least 2 atm gas pressure inside the chamber.

Onto the window a phototube can be attached, and it is coupled to it optically by Silicone grease. As pointed out before, the photomultiplier face has to be out of quartz as well, not to attenuate the UV scintillation radiation. There are only few photomultipliers, which conform with this condition. One is the 58 UVP [35], and its

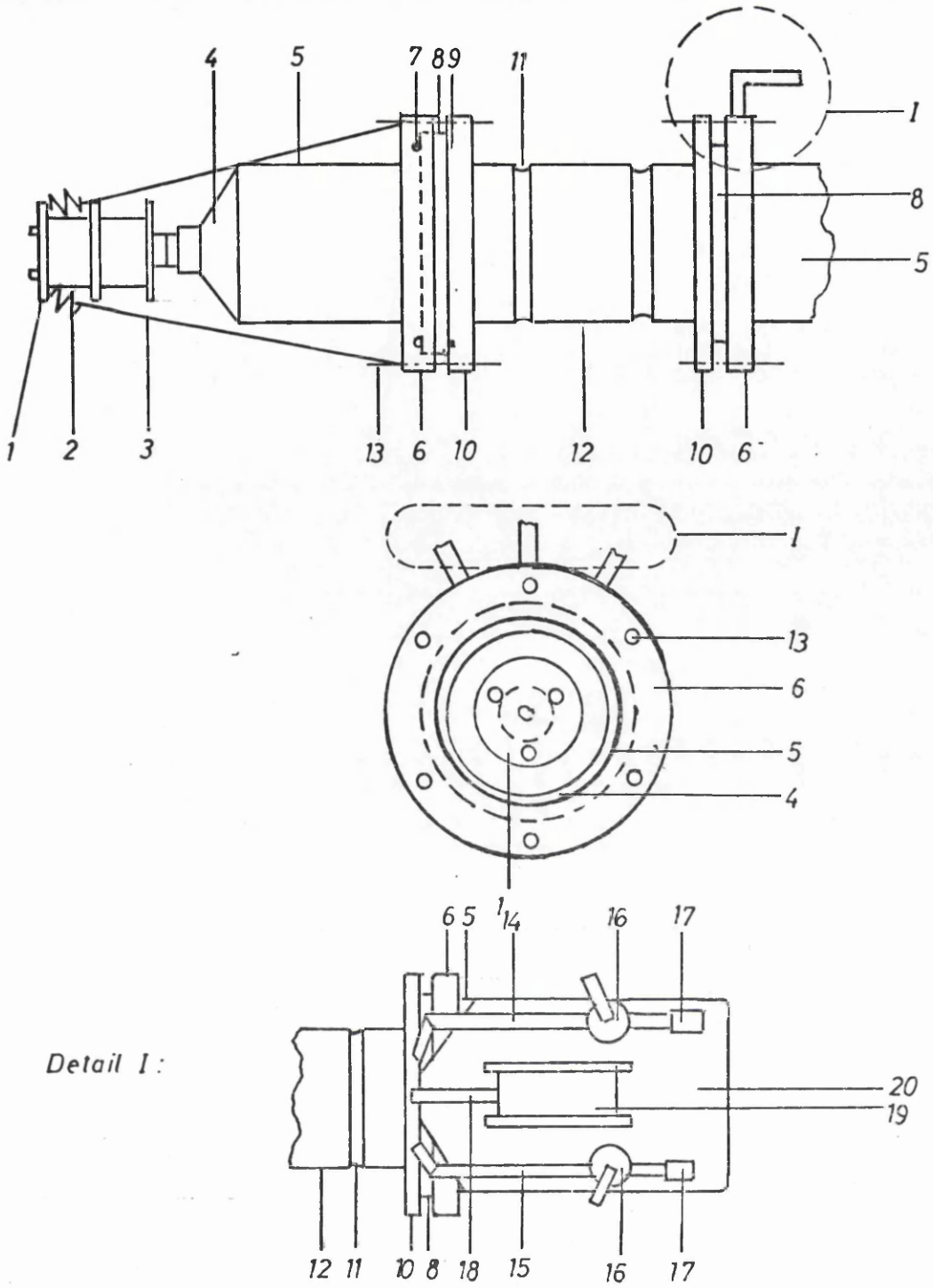

Pict. 13: Design of the Gas Scintillator

1: Photomultiplier Base; 2: Metal Springs; 3: Plastic Cord; 4: Photomultiplier; 5: Mu-Metal Shield; 6: Tufnol Flange; 7: Rubber Seal; 8: Quartz Window; 9: Indium Seal; 10: Metal Flange; 11: Stiffening Ribs; 12: Chamber Body; 13: Bolts; 14: Gas Pipe; 15: Vacuum Pipe; 16: Valves; 17: Connectors; 18: Pressure Pipe; 19: Pressure Gauge; 20: Support

sensitivity versus wave length is plotted in pict. 14. The tube itself is shielded by Mu-metal against magnetic disturbance over its entire length and rests between two sets of clamps. It is forced against the window by metal springs, fastened between a point at the photomultiplier base, which is a standard resistor chain, and a length of plastic cord, fixed to a bolt, connecting the flanges, with the other end.

2.8 The Vacuum and the Gas System

To achieve a clean gas, to be used as a fast scintillator, it is neccessary to produce a good vacuum before hand. The chamber therefore has separate gas- and vacuum supply connectors and one for a pressure monitoring gauge. These can be seen from detail I in pict. 13. Three pipes leave one of the flanges, welded onto the chamber body, radially. The flange itself has holes drilled into it, thus making a connection to the interior of the chamber. The three pipes then bend by 90^{o}. The vacuum and the gas pipe are then interrupted by valves, whereas the pressure pipe leads straight to a gauge, which is capable of measuring pressures from vacuum to 2 atmospheres absolute. The gas and vacuum pipes have connectors to the gas supply and to a vacuum pump respectively. All piping, seals, parts of the valves, including membranes, have to be out of metal, for the same reasons as applying for the Indium seals in subsection 2.7.

The seal, connecting the gas supply, also has to be out of Indium, whereas the seal at the vacuum connector can be a rubber one, because any contamination, arising from it, would be pumped out and the valve closed after that.

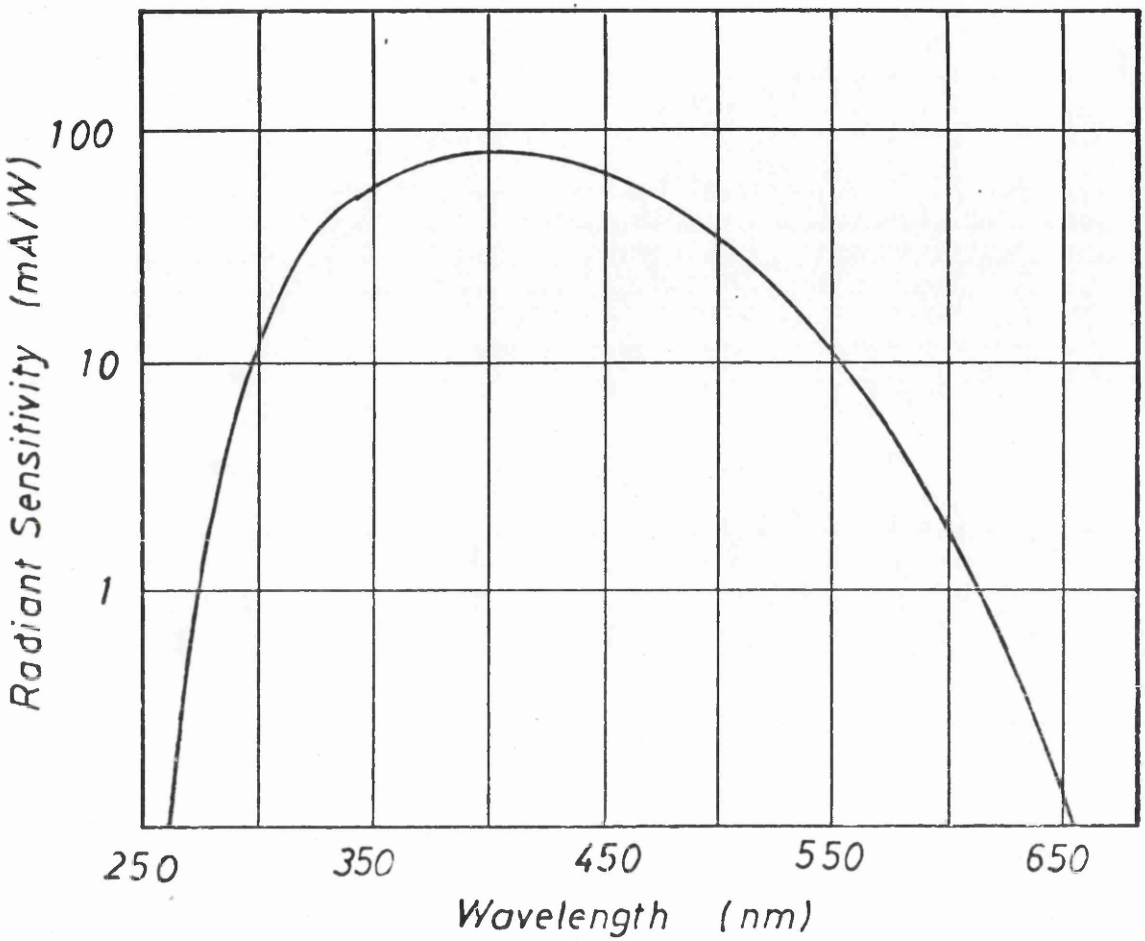

Pict. 14: Radiant Sensitivity Against Wavelength For a 58 UVP[35]

The vacuum itself is achieved by firstly using a rotary pump, to pump the chamber down to a rough vacuum, about 10^{-1} torr, and after that a diffusion pump is brought into action to bring the pressure down further.

2.9 Cleanliness of the Detector System

Every precaution was taken to make the chamber and its additional parts as clean as possible. The interior of the chamber itself was cleaned with Nitric acid, to get rid of dirt from the welded and soldered connections. It was then rinsed under water. The pipes, leading to the gas bottle and to the pumps, were filled with Trichlorethylene and left for 24 hours, before they were also rinsed under water.

During the evacuation process the whole chamber and the pipe work, including valves, were covered with resistive heating tape, the power output of which could be controlled by a variable transformer. The temperature of the tape was monitored carefully, not to exceed 150^{o} C, which is below the melting point of Indium. The heating was necessary, to evaporate any residual water or organic compounds, the vapour of which could then be pumped out by the diffusion pump.

After the pressure reached about 10^{-3} torr, a cold trap, which was part of the pumping system, was filled with liquid Nitrogen, to condense residual vapours in the chamber-pump system. The pressure near absolute vacuum was monitored by a sensitive Penning manometer,

rather than by the gauge at the chamber, the accuracy of which was only useful at higher pressures. After 24 hours of pumping the vacuum obtained was 10^{-5} torr, which was considered to be sufficient under the described precautions.

2.10 Stability of the Detector

When talking about stability of the gas scintillator, the constancy in pulse amplitude for a given particle with given energy over a period of time is referred to. A given pulse amplitude spectrum can also be used as a reference. How this was done, is described in the next subsection.

The factors, influencing the stability of the scintillation output, are:

a) Gas Pressure:

The effect of this has been carefully investigated and is presented in subsection 2.11.

b) Temperature:

This effect is similiar to that concerning pressure. It was usually sufficient to rely on the outside temperature at the detector station, since variations are small during one and the same experimental run (estimated $\pm 2^{o}$ C maximum variation) and their effect is even smaller on the scintillation output. The other possibility is to keep the chamber temperature constant at about -70^{o} C by the use of a cold finger, welded onto one of the flanges, and cooled by solid CO_2 (dry ice).

c) Electric Field Effects:

These are of repetitious short time nature, and their elimination is described in subsection 2.14.

d) Magnetic Effects on the Photomultiplier:

The investigation of these is presented in Appendix A.

When eliminating the causes c) and d), and keeping a) and b) constant, no change in pulse amplitude could be observed over long periods of time. Even after having left the gas in the chamber for several months, no adverse effects on the pulse amplitude resolution could be observed, and the scintillator was still in a useable state, as if freshly filled with gas. This, of course, was only possible, when the chamber was absolutely gas tight, and all impurities had been eliminated, before filling it with gas.

2.11 Tests With a Cf-252 Source

To test the scintillation chamber in its response to α-particles and fission fragments, and to adjust its pressure, to give an optimum pulse amplitude resolution, tests were carried out with a Cf-252 source. This emitted fission fragments and α-particles as natural decay products. This is a well-known procedure for calibrating a gas scintillator[36]. The strength of the source was about 120 fission events per minute and an about 30 times higher α-rate. The source was obtained from the UKAEA Harwell. It had been evaporated onto a thick stainless steel backing and was covered by a thin Nickel film, to prevent migration of the Californium. It was placed inside the chamber in a small frame, facing one window at a distance of about 10 cm.

It has been observed[34], that the pulse amplitude of a given particle

with given initial kinetic energy varies with pressure in a gas scintillator. Since this is of importance for the pulse amplitude resolution, a series of tests were conducted, and pulse amplitude spectra were taken for different pressures. A measure for the resolution was hereby the qualitative impression of good separation between fission fragments and α-particles as well as the clear appearance of two well distinguishable fission fragment peaks.

The electronic setup for these tests is shown in pict. 15. The photomultiplier was powered by a regulated high voltage power supply. The anode output of the tube was taken from a resistor chain base and fed into a selectable active filter amplifier, where it was integrated and amplified. The amplifier output then was split, to observe it on an oscilloscope, and was fed simultaneously to two different pulse height anlaysers, one providing a numerical outprint of the channel contents, the other a paper tape output. A photograph of the display of the latter was also taken with a Polaroid Cam-era. The paper tape output was coupled to the analyser by an analog to digital converter.

The general range of possible pressures was between 0 to 2 atm, predetermined by studies of other authors[33], the discussion of timing and pressure in subsection 2.6 and the mechanical strength of the chamber itself. During the actual tests measurements were taken at vacuum, 0.06, 0.17, 0.3, 0.5, 0.67, 0.8, 1.0, 1.3, 1.6, 2.0, 2.3, 2.6, 3.0 atm abs. Pict. 16 shows a series of Cf-252 spectra, taken at various pressures. It can

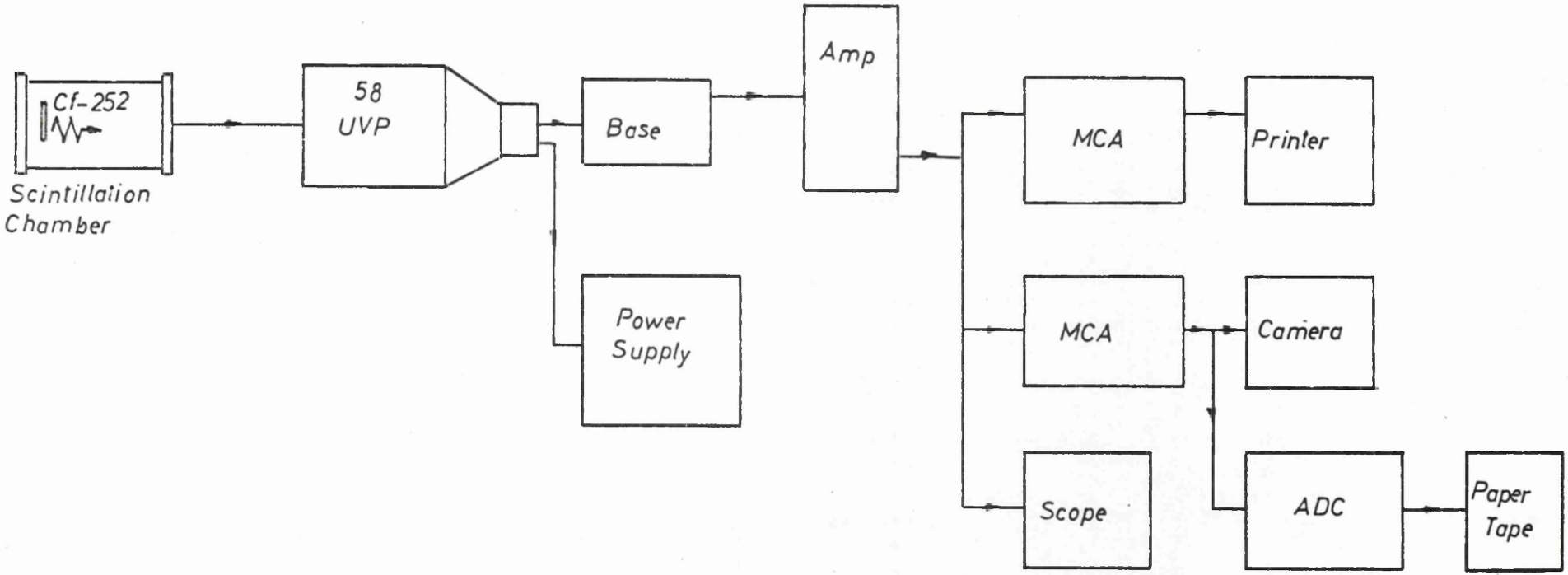

Pict. 15: Electronic Setup For the Cf-252 Tests

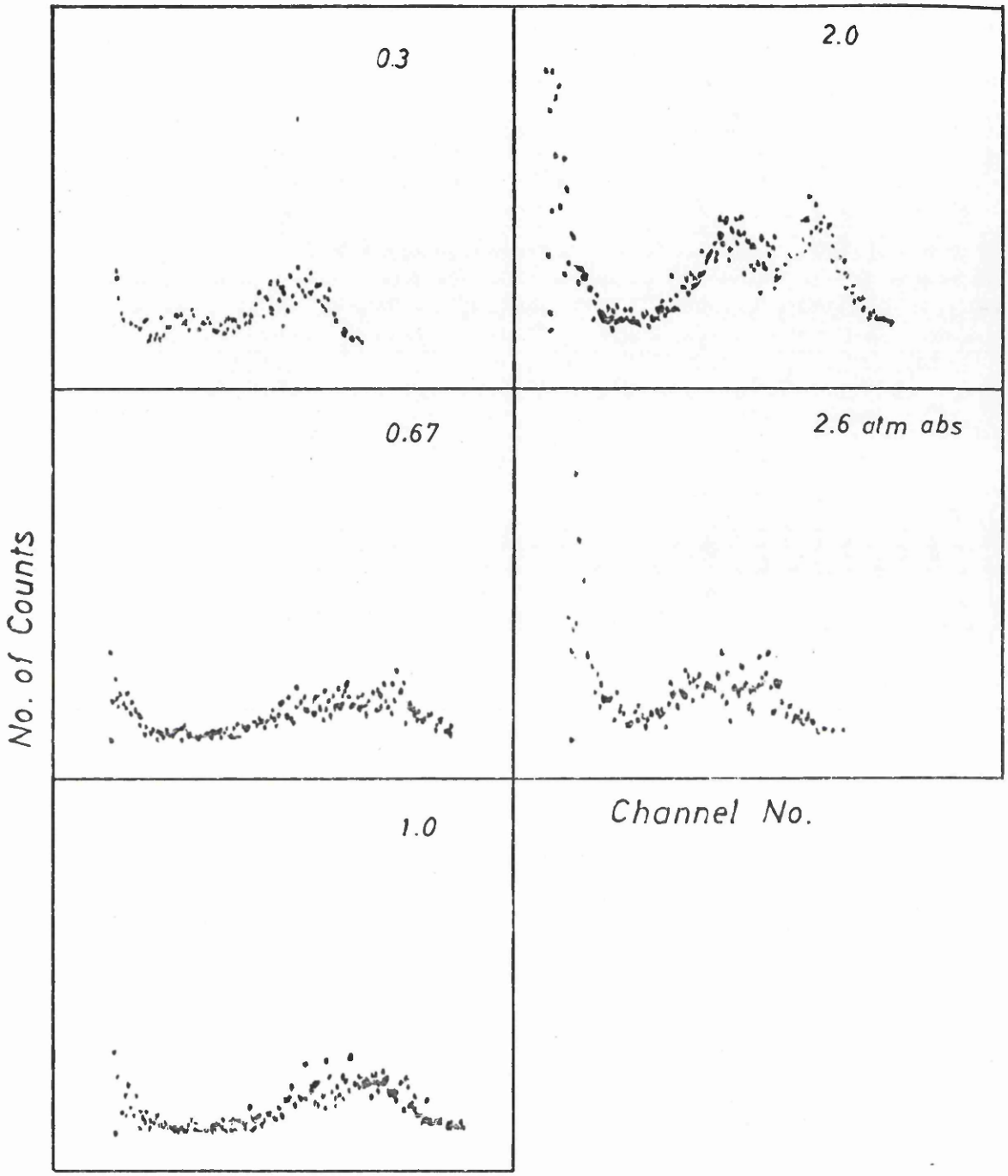

Pict.16: Cf-252 Spectra At Different Pressures

clearly be seen, that the pulse amplitude decreases with increasing pressure, but that the resolution is not determined by a simple proportional law. It was finally decided, that in the investigated range the spectrum, taken at 2 atm abs, showed the best resolution. In the following the details of this measurement are given:

Accumulation Time:	20 min.
High Voltage:	2 kV
Amplifier, Ortec 440A:	Coarse Gain (high): x32
	Fine Gain: 0
	Shaping Time: 2 μsec.
	Unipolar Prompt Output

Since the decay of Cf-252 is accompanied also by γ-radiation, γ-quanta were present at the same time, but they were either submerged in the α- and noise-peak, or the detector was not sensitive to them. Tests with an external stronger γ-source also did not show any conclusive evidence about the detection capability of γ-rays by the scintillator.

2.12 Target Arrangement

As has been mentioned in the previous subsection, the Cf-252 source had to be fitted into a small frame, which was stuck inside the chamber, to face the phototube. The arrangement for the U-235 and U-238 fission targets, however, had to be different, since the targets had to face the incident neutron beam, which was perpendicular to the chamber axis and also face the chamber window, which was parallel to the neutron beam, at the same time. A 45^{o} angle represents a compromise between these requirements. The U-235 fission target foil was obtained again from

the UKAEA Harwell. The fissile material, which was at a thickness of 0.75 mg/cm^2, was evaporated onto a Tantalum backing in the form of U_3O_8, which left a 2 mm wide fringe around the circular 7 cm diameter sensitive target area. A thin film of Gold covered the foil, to prevent migration of the α-active fission material. The U-238 target was bought from Twentieth Century Electronics, and the backing was stainless steel, 8 cm in diameter. There was no covering film over the sensitive area, which was 7.6 cm in diameter, and the fission substrate was pure Uranium at a thickness of 1 mg/cm^2. A more detailed assessment of the target mass as well as α-activity will be made in appendix C.

A target holder was constructed (s. pict. 17), which consists mainly out of two steel rings, fitting concentrically between the chamber reinforcing ribs and held together by two strips of steel. Between these strips a pivoting ring was fixed, to take one target on the side, facing the neutron beam and at the same time one chamber window at 45^o, and on the other side, with its back to the target, the Cf-252 source. The target ring could be pivoted from outside by using the force of gravity, when the chamber was tilted, and thus the same phototube could face either the fission target or the Cf-252 source. The latter was included, to have a known reference for the pulse height spectrum during an experimental run. Target and source were fastened on a sheet of thin Aluminium, which in turn was bent round the edge of the pivoting ring.

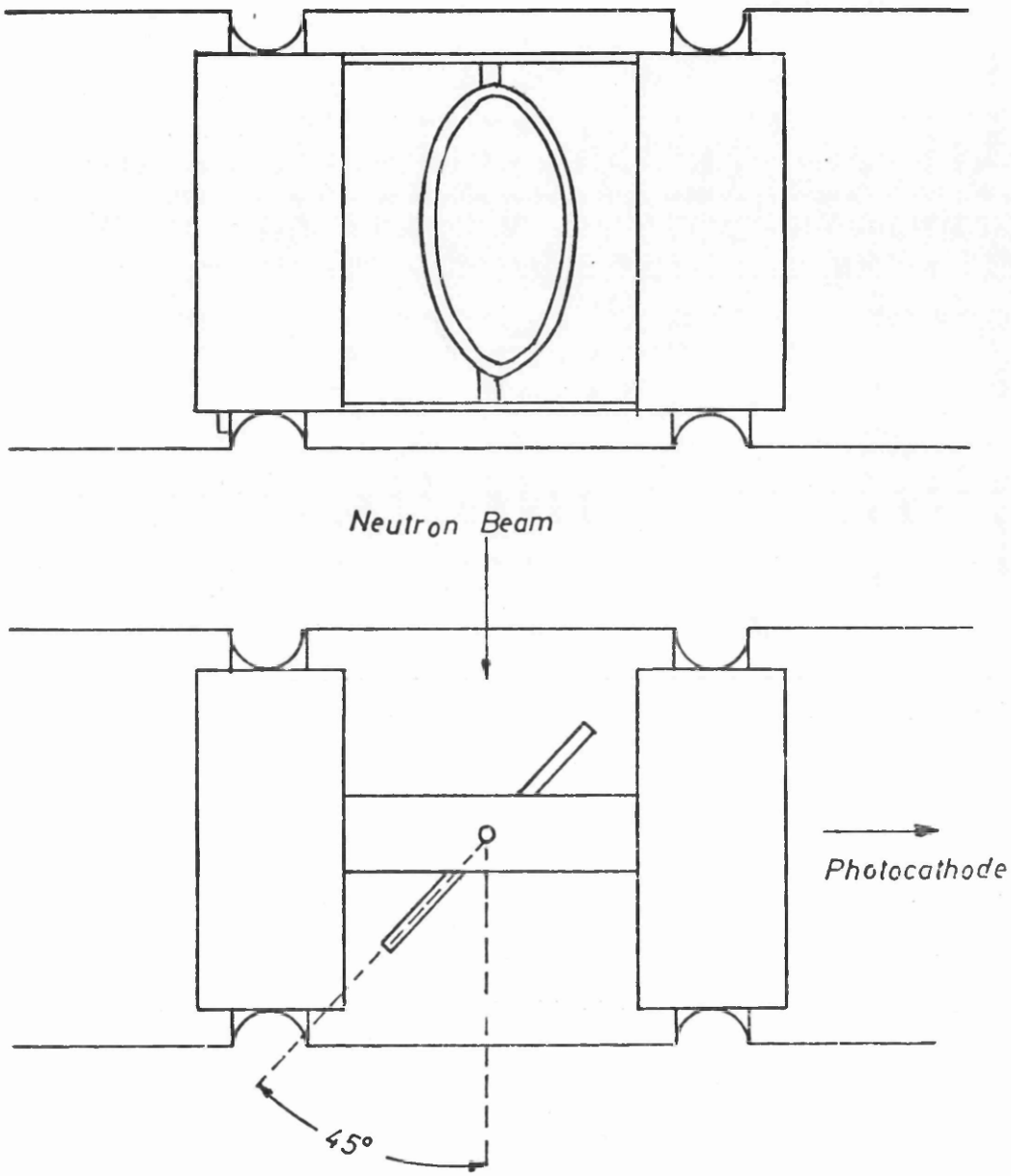

Pict. 17: Target Arrangement

2.13 Accelerator Test and Elimination of the γ-Flash

To test the gas scintillator under experimental conditions on the pulsed neutron beam of the Kelvin Laboratory electron LINAC, the U-235 fission target was arranged as described in the previous subsection, and the detector placed at a distance of 13 m from the neutron production target at the 90^{o} flight path in the North Hall. During this test it was soon discovered, that the detector was sensitive to the γ-flash, preceding the arrival of the first neutrons from the production target. At this flight path position a γ-flash signal of 3 to 4 Volts was measured on an oscilloscope. This was of the same order of magnitude as the fission fragment scintillation pulses, whereas the α-particles did not exceed about 300 mV. Since the γ-signals, occuring with the repetition frequency of the accelerator, would trigger a TAC every beam burst, and since they could not be excluded by setting a discriminator threshold, some other means of excluding them had to be devised.

For the pulse height analysis a similar electronic setup was used as in the tests with the Cf-252 source. In addition to this the timing of the fission pulses was investigated. The whole electronic system for these tests is displayed in pict. 18. The anode pulse of the photomultiplier is taken from the base and fed into a linear fan out, which provides two outputs. One of them serves as an input to a discriminator.

The discriminator is set to exclude the small amplitude α-signals,

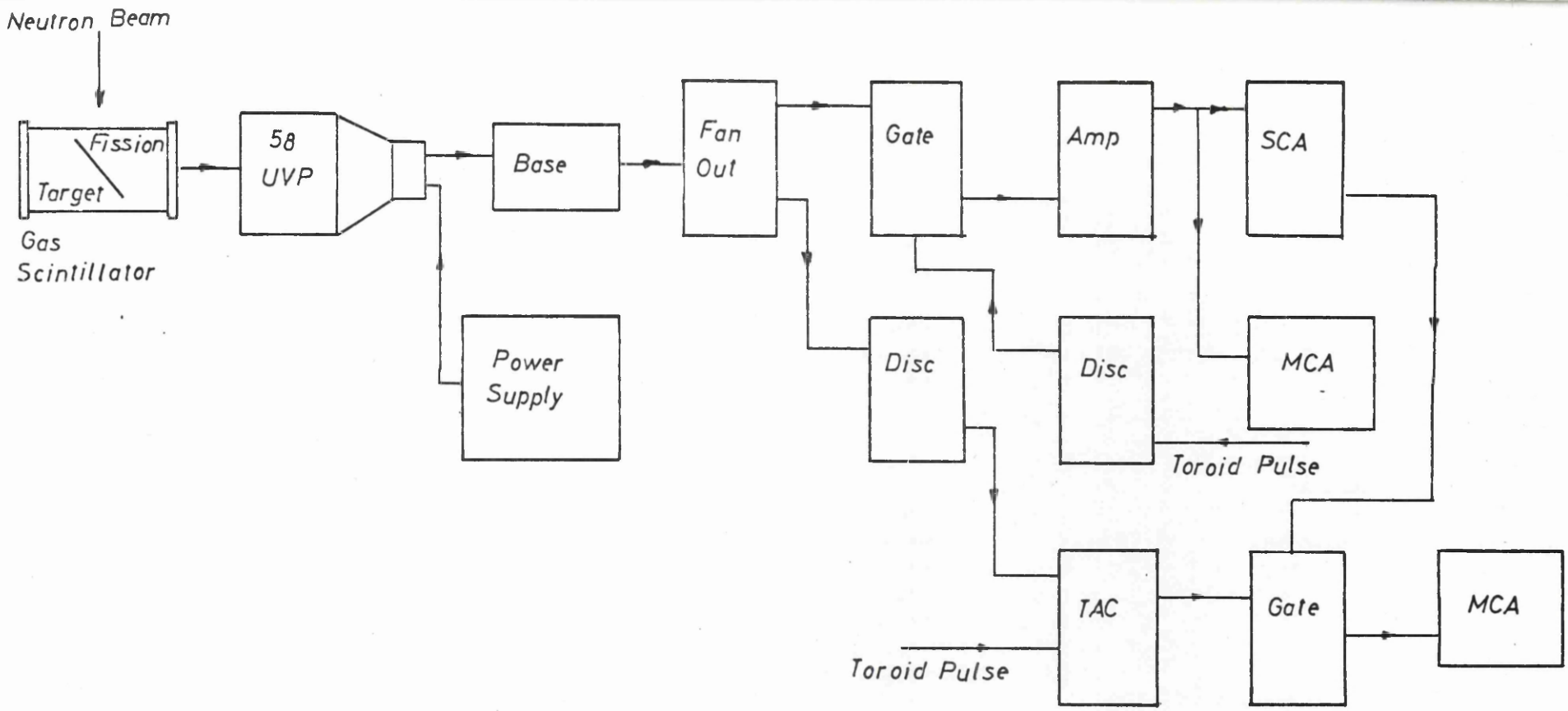

Pict.18: Electronic Setup For the Accelerator Test

and its logic output goes as a stop pulse to a TAC, which gets its start pulse, delayed after the γ-flash, from another discriminator, having as input a toroid pulse, produced by the electron beam. The TAC output is then fed through a linear gate to a multichannel analyzer.

Pulse height information is derived from a second fan-out output. The second fan-out output is fed through a fast linear gate, before it goes to an amplifier for pulse height analysis. The fast gate is driven by the output of a gate generator, which has its input from another toroid beam pulse. This output is also delayed after the arrival of the γ-flash, according to pict. 19, and opens the fast gate for several μsec., to cover the required energy range. The amplifier output is split, and one pulse goes to a multichannel analyzer for pulse height investigation, whereas the other one serves as an input of a single channel analyzer, the threshold of which is set to exclude α-particles and drives the linear gate, which controles the TAC outputs.

Setting a threshold twice against small pulses - once at a discriminator for the time pulses and once at a single channel analyzer for the linear pulses - was done, because it is difficult to exclude all small pulses with a fast discriminator, without excluding accidentally also a portion of larger fission pulses. Therefore the discriminator was mainly set to exclude noise, and the single channel analyzer to exclude the somewhat larger α's and random

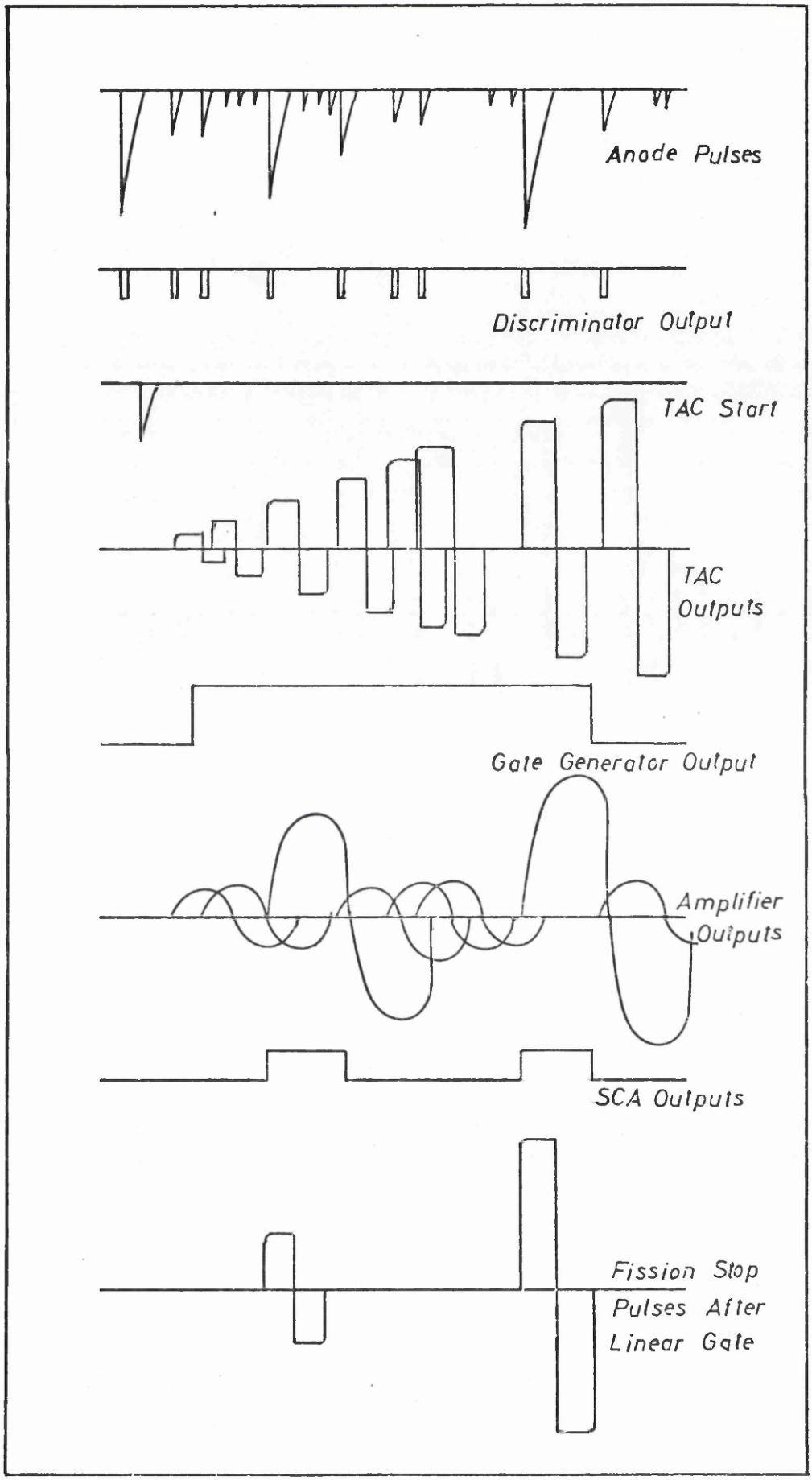

Pict.19: Pulse Scheme For Accelerator Test

small γ's. The single channel analyzer was also neccessary, to exclude the amplified transients of the fast gate.

The main aim of these tests was, to test the detector's reaction to the γ-flash and to find a system, which eliminated its effect, which was done successfully.

2.14 Electric Field Effects On the Chamber

During initial tests with the Cf-252 source large pulses, by far exceeding those created by fission fragments,were observed in the pulse height spectrum. These pulses were randomly distributed over a wide range beyond the fission pulses as well as culminating in a broad peak in a high pulse amplitude region. Pict. 20 shows the total pulse amplitude spectrum.

There is no explanation possible of these pulses, having a genuine physical meaning in terms of arising from particles or from the Californium source. When observing these pulses during the accumulation on the multi-channel analyzer, it was discovered that after time intervals of a few seconds the photomultiplier was recording a burst of pulses all over the amplitude region, but primarily at these high amplitudes. This led to the conclusion, that there was a build up of an electrostatic field in the chamber, created by the combined action of the high voltage photocathode (2000 V) and the di-electric quartz window. This

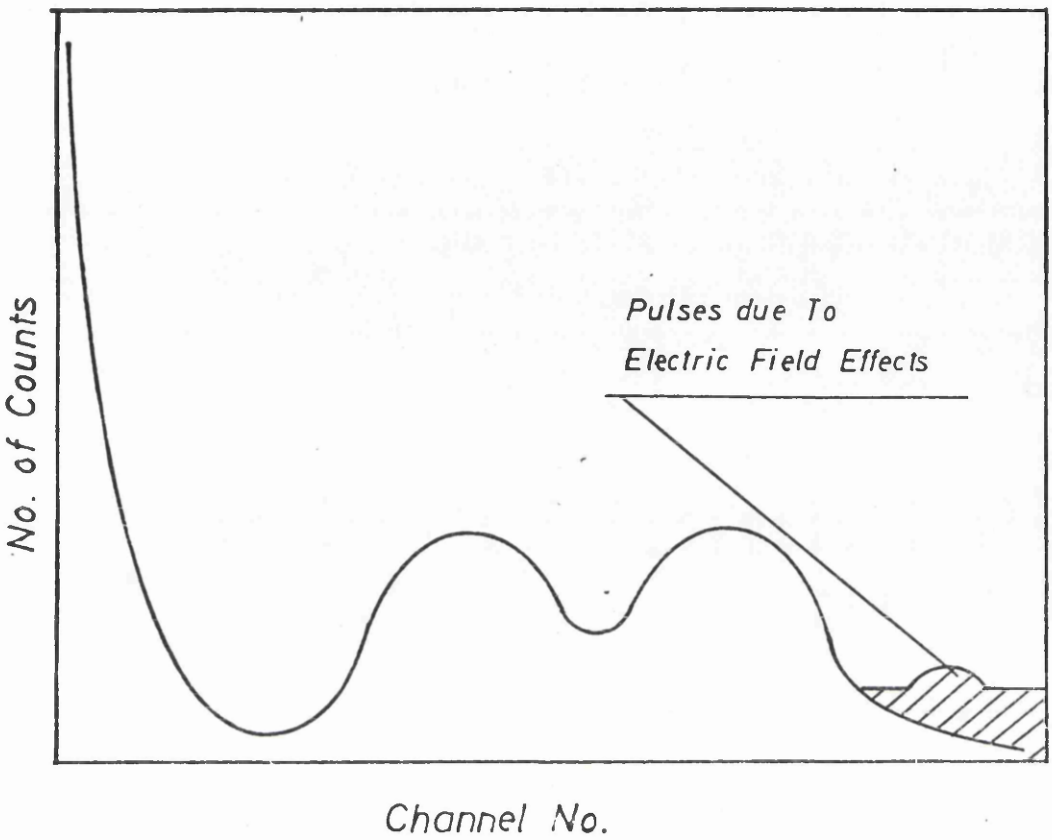

Pict.20: Pulse Amplitude Spectrum With Electric Field Effects

"condenser effect" led to a discharge after some time, producing secondary emission of electrons by accelerated ions towards the window from a scintillation pulse, which in turn created a release of a number of small scintillation pulses, piling up to a single large amplitude pulse as well as a number of smaller amplitudes.

To eliminate these field effects, it was neccessary to have the chamber at the potential of the photocathode. To provide good electric coupling and to have no adverse effects between the quartz window and the outer face of the phototube, a grid of conducting paint was painted over the face of the photomultiplier. This grid was connected electrically to the photocathode and to the chamber body, so that the whole system was at equipotential high voltage. Further tests revealed now the disappearance of the previously observed field effects.

2.15 The Monitor Detectors

As has been pointed out at the beginning of this chapter, to measure a fission cross section, it is essential to have at least one separate detector from the fission chamber, which monitors the incident neutron flux in strength and energy-distribution. This requires a fast neutron detector, which has good timing qualities, and the efficiency of which is known or can be calculated fairly accurately. Such detectors have been used and tested under experimental conditions exhaustively in the past, and one of them

is a plastic scintillator, mounted on a photomultiplier, in the present case an NE 102-56 AVP combination .

The scintillation properties of this kind of detector are understood very well [25,33]. In the neutron detection process an incoming neutron collides with a proton of the hydrocarbon compound, out of which the scintillator is composed, and thus excites the molecules. In the de-excitation process a photon is emitted, which can be detected by a photomultiplier. In the present case the dimensions of the NE 102 scintillator were 0.621 x ∅1.27 (cmxcm). This meant, that for calculating the efficiency of the detector, multiple scattering of an incoming neutron could be disregarded, and the scintillator could be used at a fairly short flight path, (ab. 20.0 m), without having too much pile up, when monitoring the incoming flux.

Although in principle one monitor detector should be sufficient, it is very useful, to have a second one,which at least measures the strength of the neutron flux. This need not be a time-of-flight detector, and it therefore need not be positioned at the same flight path than the other two detectors. Its main purpose is to compare its counting-rate with that of the other two detectors, to check their stability, regarding, for example, photo-multiplier gain. Because the accelerator beam itself can be unstable in current or steering, this can be checked with the count-rate of three detectors. Their ratios should be constant, if they are working all right, and if variations are only due to accelerator conditions.

The second monitor detector was a LiI-crystal. The scintillation process of these are different than for organic scintillators[25,33]. A main part is played by impurities in the crystal, for instance Tl^+-ions, which provide intermediate energy states between the valence band and the conduction band. An excited electron can thus be captured into such an intermediate state, from which it can decay either radiationless through crystal vibrations or by emitting a photon, which can be observed by a photomultiplier. Since the probability of neutron detection decreases with neutron energy, a moderator of paraffin wax was introduced in front of the detector, to provide thermalized neutrons. This was feasible, because only the number of neutrons per unit time was interesting, not their energy-distribution, which is independent of accelerator variations.

2.16 Reduction of After-Pulsing In the Monitor Detector

The NE 102 monitor detector is, of course, similarly effected by the γ-flash, as the Xenon Chamber, only, that the signal produced in it is about 12 V for the necessary high voltage (2 kV). A pulse of that magnitude will create after pulsing in the photomultiplier, and it is therefore not sufficient, to exclude the γ-flash signal in the same fashion as for the gas scintillator.

After-pulsing or satellite pulses have been investigated by several authors[37,38]. When a strong light signal hits the photo-

cathode and produces the release of a shower of electrons, there is the possibility of positive ions being released subsequently from the first dynode. These ions can originate from residual water, enclosed in the phototube during manufacture, and they tend to migrate to the photo-cathode after having been released, and so create a secondary signal. This effect is negligible for normal small pulses, but not for large saturating signals. There is naturally a variation of recovering capability within a short period of time and of the time between original pulse and after-pulse. This time-lapse is characteristic for each type of photomultiplier, and, indeed, for each individual phototube itself. After-pulses are small in amplitude and well defined in time, regarding their first appearance in a time spectrum, although the distribution tends to tail off rather slowly. Pict. 21 shows the typical time distribution of after-pulses.

To eliminate them, it is neccessary to make the photo-cathode of the multiplier insensitive to the scintillation signal, which causes it. In pict. 22 the electronic system used can be seen. The photocathode is constantly at a "barrier" voltage, which prevents electrons reaching the first dynode, i.e. the first dynode is permanently negative with respect to the cathode. Only shortly after the γ -flash the cathode is made sensitive for a period of time (several μsec.), by applying a pulse from a generator, which enables an amplifier circuit, to set the cathode to normal operating potential for its duration, allowing detection of the subsequent signals. After that the cathode is reset to"barrier" voltage again. In this way it cannot "see" the γ -flash at all, and no after-pulsing is produced. The pulse generator input is taken from an accelerator

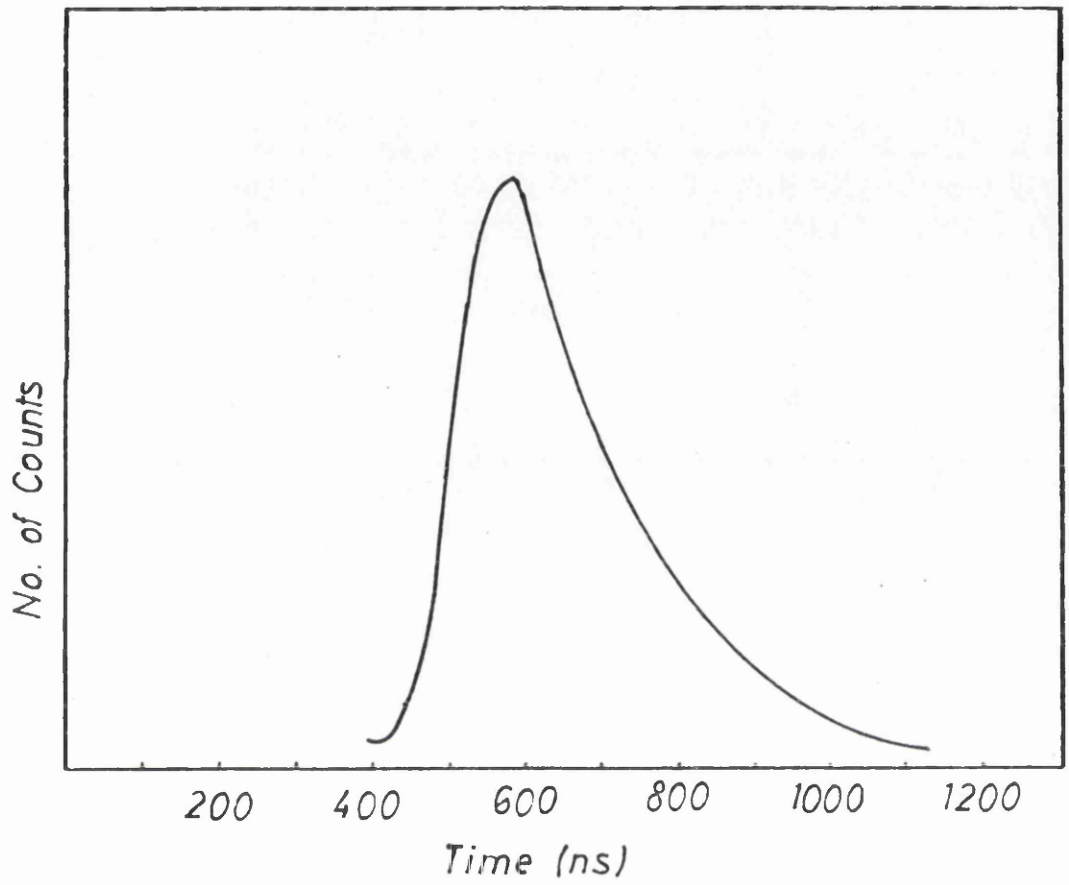

Pict. 21: Time Distribution of After Pulses[37]

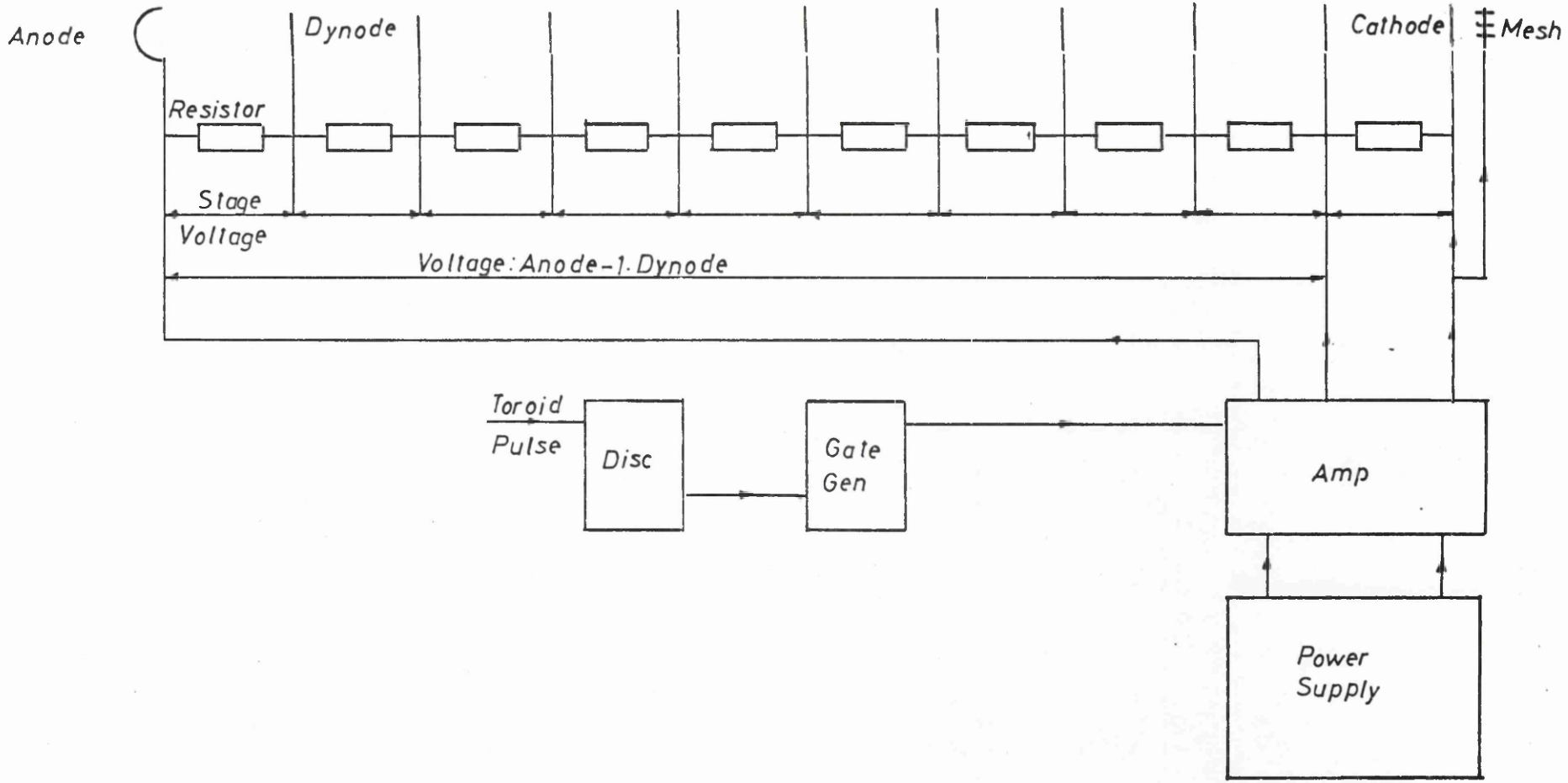

Pict. 22: Cathode Switching Scheme

toroid and thus occurs at beam frequency. To provide good electrostatic coupling between the pulse circuit and the photo cathode, a wire mesh is introduced in fron of the photomultiplier face and also connected to the cathode potential.

After pulsing is not a serious problem for the LiI monitor and the γ-flash can be eliminated by the same technique, applied to the gas scintillator.

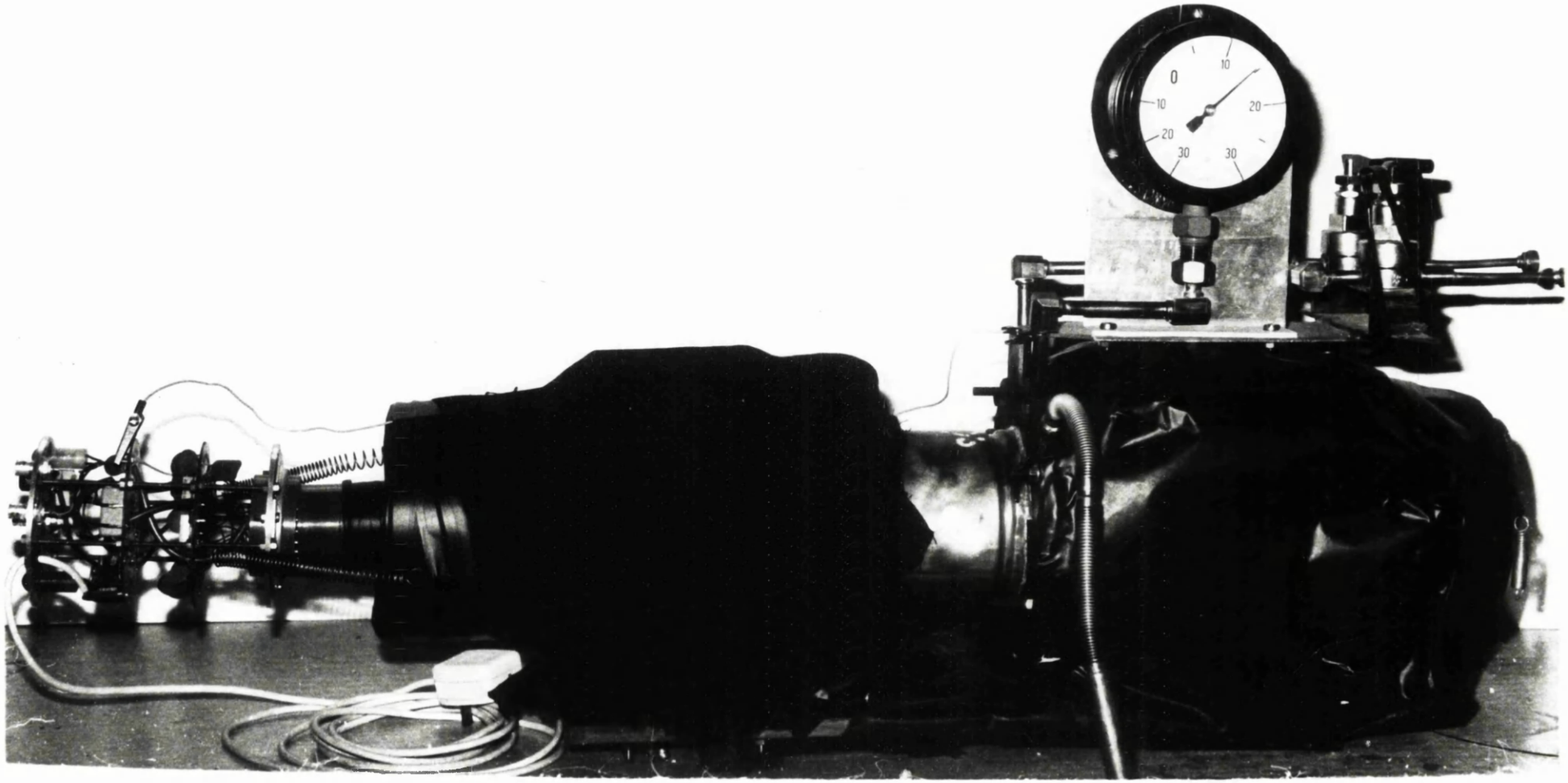
0
10
10
20
20
30
30

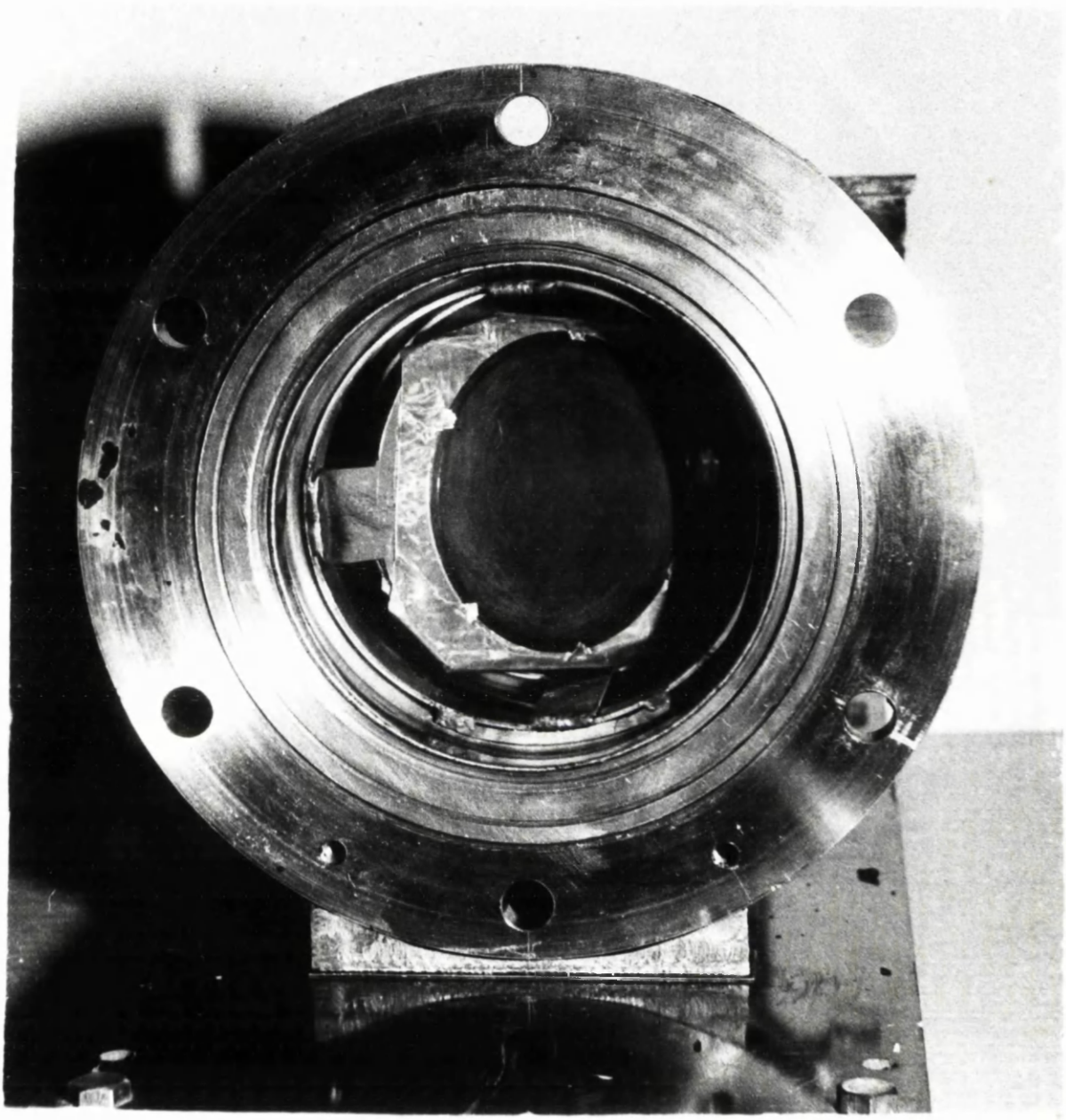

CHAPTER III

3.1 Introduction

The measurements of the fission cross section of U-235 and U-238 were performed during two subsequent experimental runs with the gas scintillator, described in the previous chapter. The duration of the run was determined by the statistical precision required and the decision about how long a time would be reasonable in terms of stability of the detectors and electronics and of the general experimental schedule in the Kelvin Laboratory. The energy region investigated was determined by the neutron flux, provided by the LINAC, the effect of eliminating the γ-flash and the thresholds neccessary for the main monitor detector to eliminate noise. Major tools beside the detection system were, of course, the 100 MeV electron linear accelerator and a PDP-7 online computer of the Laboratory.

A careful decision about the choice of flight-path in respect to the angle to the elctron beam as well as to its length had to be made. This is also true for beam collimation and filtering. The electronic systems for both main detector and monitors were somewhat different from those, used in the previous tests, mainly because of the use of the online computer. Before the run the discriminator for the anode time pulses had to be set at a certain bias level, to eliminate noise. This had to be checked during and after the run. The data storage was done, as already indicated, in a PDP-7 computer via analog to digital converters, using a programme, which allowed a coincidence storage of time and linear pulses for the main

detector. Flight Path, electronics, beam pulse, and storing bin width determined the time resolution of the system. The background in these experiments was - apart from electronic noise - mainly due to α-decay of the targets and a small amount of after pulsing due to γ-flash in the phototube for the Xenon Chamber. For the later conversion of the time spectra to energy spectra a time calibration of the multichannel store had to be undertaken as well as an absolute energy calibration for at least one particular individual channel.

3.2 Positioning of the Detectors and Collimation

The γ-flash produced a rather high signal in the gas scintillator, although much smaller than in the NE 102 monitor. Since, to eliminate field effects, the whole chamber had to be at photocathode potential, and therefore to eliminate this small amount of after-pulsing, the chamber itself would have to be switched. This presented problems, concerning electrical coupling and therefore gain stability. It was decided, to accept these after-pulses and eliminate them later in a different way analytically. Nevertheless it was neccessary to make the γ-flash as small as possible. This was possible in three ways: choosing a fairly long flight path, choosing a backward angle with respect to the elctron beam direction, and finally, reducing the γ-flash by introducing high Z material filters. All three methods were engaged, and with all compromises had to be taken:

a) Length of flight path:

Since the inverse square law for flux reduction against

distance is valid, in theory the γ -flash can be made as small as desired. The limit here is set by the simultaneous reduction in neutron flux, leading to a smaller and smaller event rate. The compromise was such, that the γ -flash should be made as small as feasible, without reducing the neutron flux to an unacceptably low level with regard to the duration of the experiments. A flight-path length of 20.0 m was regarded as acceptable. In fact, it was exactly 19.96 m. The monitor detector was placed behind the gas scintillator at 20.47 m. It was not possible to place it in front of the gas chamber, without disturbing the incident flux, whereas the main detector provided little attenuation to the same. Monitor detector and fission target, of course, were coaxially positioned.

b) Angle of flight-path:

separate investigation had shown that the γ -flash is reduced, when selecting a more backward angle with respect to the electron beam direction. It is strongest in line, i.e. at 0^{o}, with the beam and falls off, when increasing the angle away from the beam. It was therefore decided to position the gas scintillator and the main monitor detector at the most backward angle possible at that length of flight-path within the North Hall. This was at 124^{o}.

c) Filtering:

by putting lead into the neutron beam line, the γ-flash could be reduced further, but naturally the intensity of the neutron flux with it. Pict. 23 shows the effect of lead on the amplitude of the γ-flash and the intensity of the neutron flux. It is noticeable, that above a certain thickness of lead the γ-flash amplitude remains constant. However, it was noted, that the frequency *i.e.* intensity, of the γ-flash is further decreased by increasing the thickness of the filter material. A compromise had to be found, regarding the acceptable amount of γ-flash in comparison with the desired not too low count rate. 3.0 cm of lead in the flight path seemed appropriate.

Inside the flight tube a lead collimator of 2" in diameter and 1 yd. in length was placed, so that the neutron beam was approximately adjusted to the target diameter at the position of the detector. The profile of the beam was measured at a distance of 15.0 m from the centre of the neutron cell and is shown in pict. 24. Since the beam was still wide at the detector, a further collimator of about 40.0 cm in length and with an internal diameter of 5" was placed just in front of the detector, mainly to prevent scattering of the γ-flash and neutrons from the flanges of the chamber, and to prevent (γ,p)-reactions in the flanges. This was checked after placing a 1' thick box of paraffin in the flight-path inside the neutron cell. All neutrons were absorbed, but the γ-flash came through in strength. No reaction from it was observed with the gas scintillator except for γ-flash.

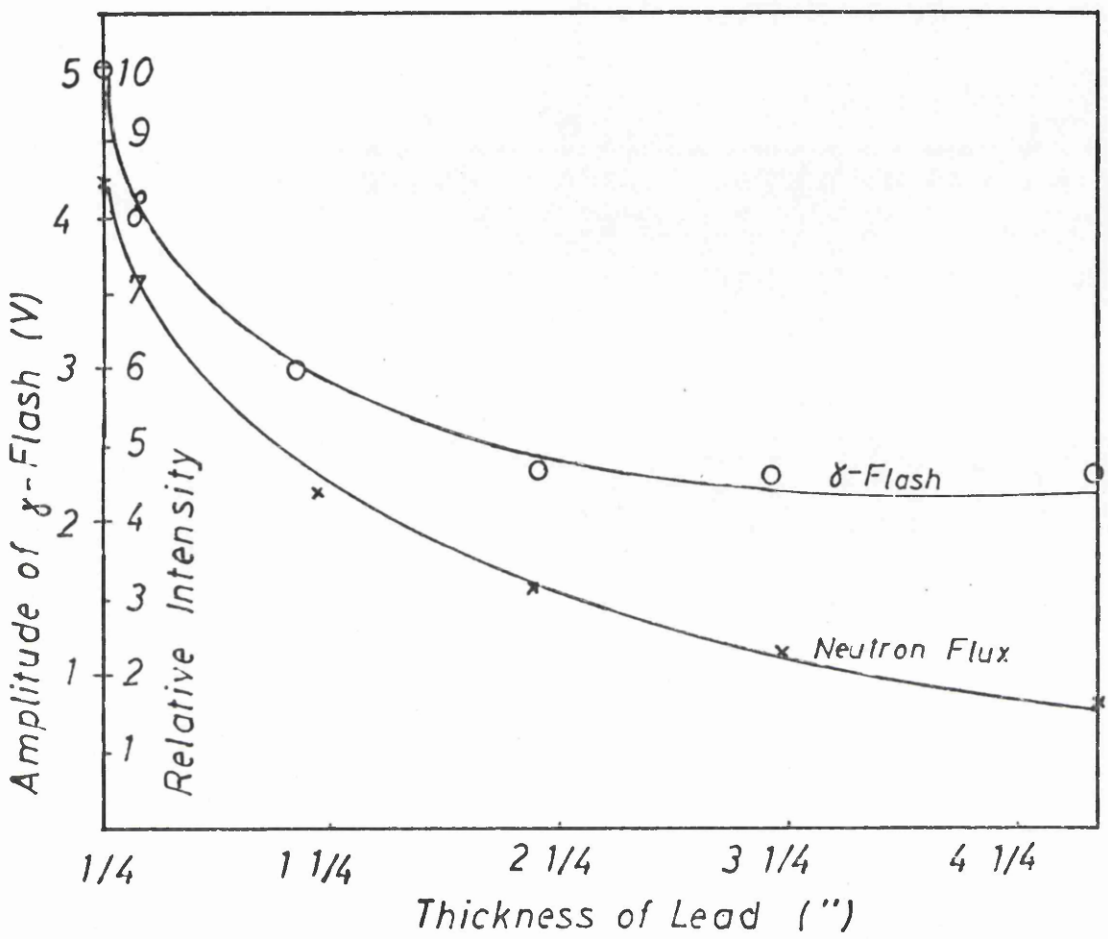

Pict. 23: Absorption of Neutron Flux and γ-Flash

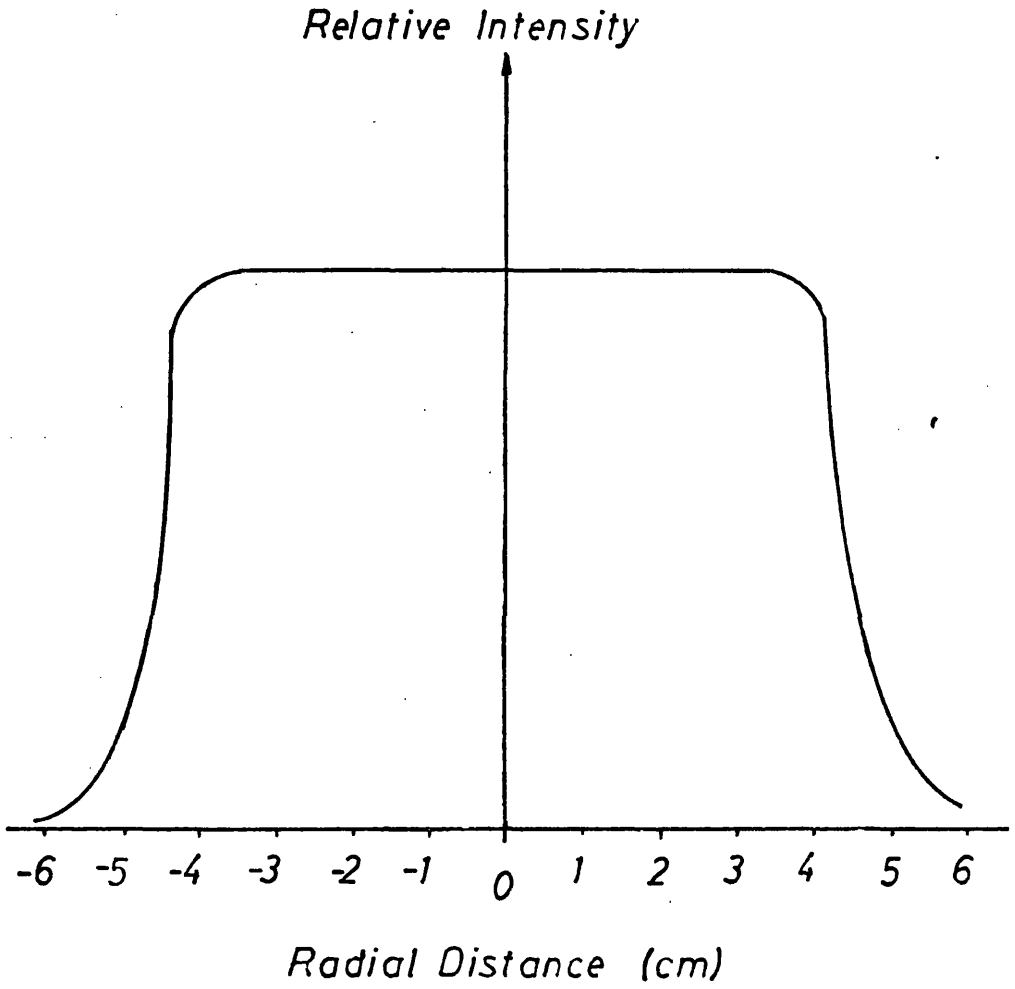

Pict. 24: Beam Profile At 15m Flight Path

Since γ-flash problems played no major role in considering the position of the second monitor, it was placed at the 90° flight path at a distance of 12.0 m. Pict. 25 shows the complete layout of the detector geometry in the North Hall of the Kelvin Laboratory.

3.3 The Electronic System For the Main Detector

Because of the way, the data are accumulated in the online computer, the electronic system for the gas scintillator is slightly different to the set up, used in the test runs. As can be seen from pict. 26, the anode pulse is again fed to a fan-out, providing two separate outputs. One serves as a linear pulse, and the other is for the time logic. The high voltage on the photomultiplier was 1800 V, which gave a pulse height of about 250 mV for α-particles and about 3 V on average for fission fragments, when the detector was operated at 2.0 atm abs gas pressure. The linear pulse was fed through a fast gate, which opened for 10 μsec., when triggered by the output of a gate generator. The input to the latter cam from a fast discriminator, which got its input in turn from a toroid beam pulse. The gate generator output was delayed for about 150 ns after the rise of the γ-flash. The output of the fast gate then went to an integrating amplifier and then through a delay amplifier, where the timing of the linear pulse was adjusted, to be in coincidence with the TAC output in the time circuit, before going to an analog-to-digital-converter (ADC).

The time pulse went straight to a fast discriminator, the threshold of which was set at about 200 mV bias. The discriminator output served as a stop pulse for a TAC, the start pulse of which was derived from another fast discriminator, taking its input from a separate toroid beam pulse.

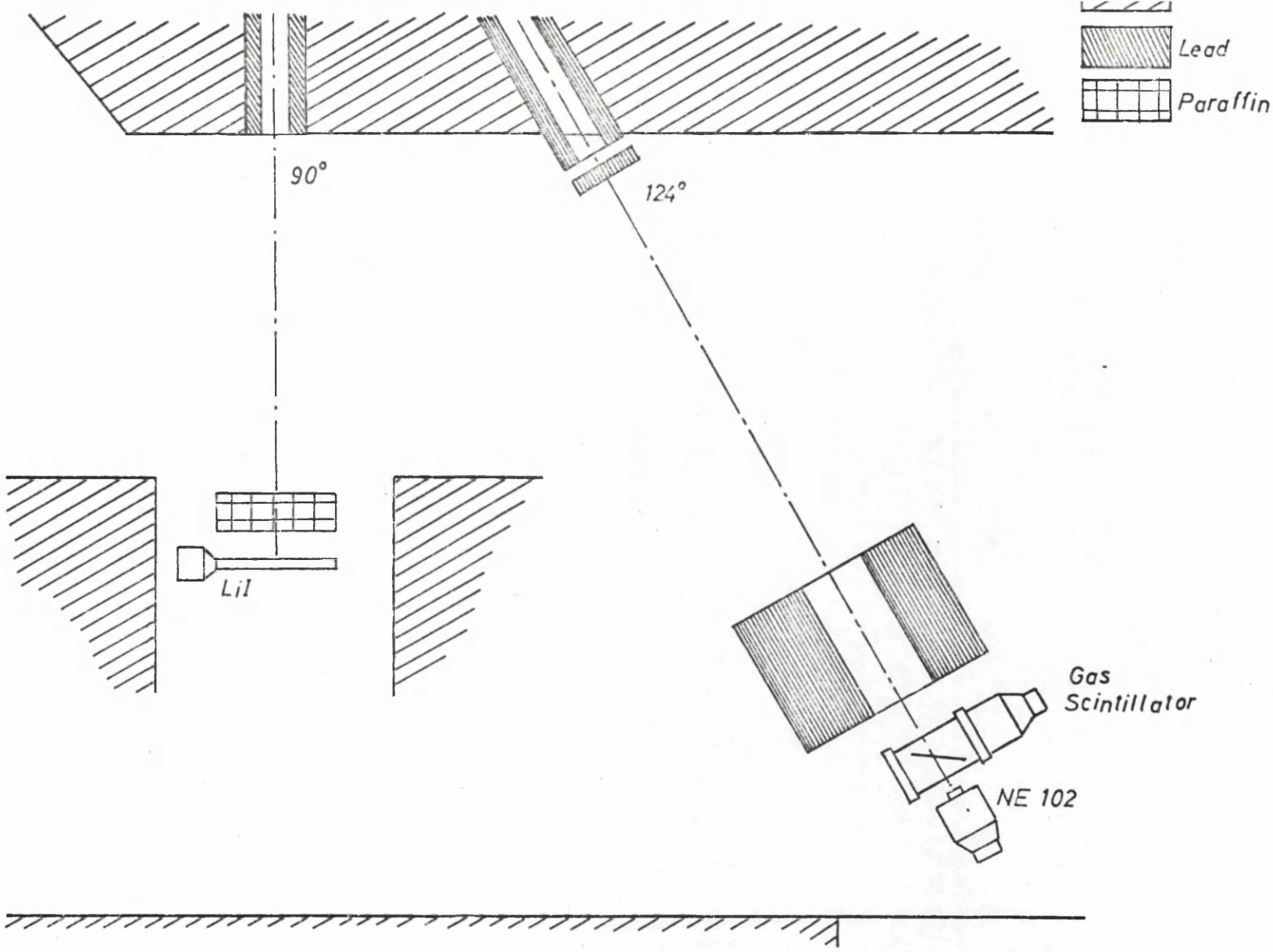

Pict. 25: Flight Path Arrangement

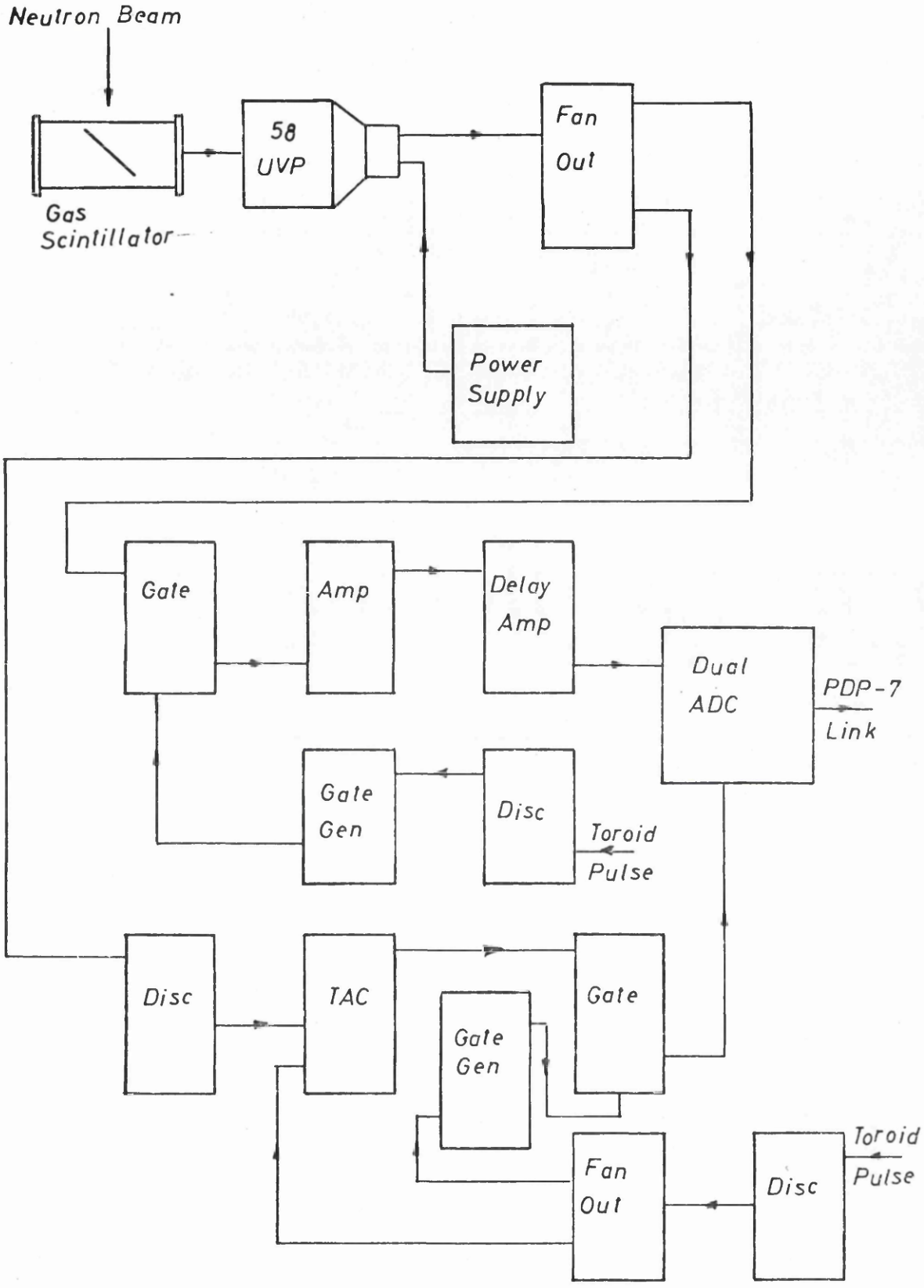

Pict. 26: Electronic Setup For the Main Detector

The output of the TAC then passed through a fast linear gate, which was driven by a gate generator. The gate generator got its driving pulse from the start pulse fan-out, to delay it for 200 ns after the leading edge of the γ-flash. The output of this gate was then matched with the linear pulse as already mentioned, before going into the same dual ADC as the linear one. The ADC was interfaced with a PDP-7 computer. The ADC-mode of data taking will be described in subsection 3.6.

3.4 The Electronic Systems For the Monitor Detectors

Firstly, the main incident flux monitor, the NE 102 plastic scintillator, is considered. The photocathode of this detector was switched, to exclude after pulsing due to γ-flash. The switching pulse came from a gate generator, which got its input from the same fast discriminator, which also provided the driving pulse for the gate generator, to trigger the fast gate for the linear Xenon Chamber pulse. The switching pulse itself was 10 μsec. long and 12 V in amplitude. The anode pulse of the detector then went directly to a fast discriminator, which was set at a threshold of 0.255 MeV neutron energy, to exclude noise. The determination of this threshold is described in the following subsection. The output of this discriminator served as a stop pulse to a TAC. The start pulse of this TAC again came from the start pulse fan-out. The TAC output was gated by a fast linear gate, which was driven by a gate generator output similarly to the main detector circuit, which got its input from the start pulse fanout and delayed it for about 200 ns after the γ-flash. The final gate output then went to a further ADC, which, of course, was interfaced to the PDP-7 computer as well.

The circuits for both monitor detectors can be seen in pict. 27.

The second monitor, the LiI detector, sent its anode signal through a fast linear gate, which was driven by a gate fan-out output, similar to the one for the linear pulse from the gas scintillator, and the output was 10 μsec. long and delayed by about 150 ns after the γ -flash. This period represents the time during which prompt neutrons can be detected,and random events are thereby excluded.

The gate output then went into an amplifier, which finally fed it to an ADC, to go eventually to the PDP-7 computer as a pulse height spectrum.

3.5 Bias Level of the Main Monitor Detector

The discriminator threshold for the anode pulse of the NE 102 scintillator detector had to be set to exclude noise signals. The commonly used method is to use a weak reference source with known energy points, related to neutron energies. The threshold should also not be too high, to extend the useful range of the incident neutron spectrum well to lower energies, in this case lower than 0.5 MeV. The reference source used was an Am-241 gamma source. The complete gamma spectrum of this source is shown in pict. 28. The peak corresponds to 0.5 MeV neutron energy.

To measure the threshold of a discriminator, the electronic setup of pict. 29 was used. The photomultiplier anode pulse is fed through the discriminator, the output of which goes to a gate generator. The gate generator output drives a linear gate. If the

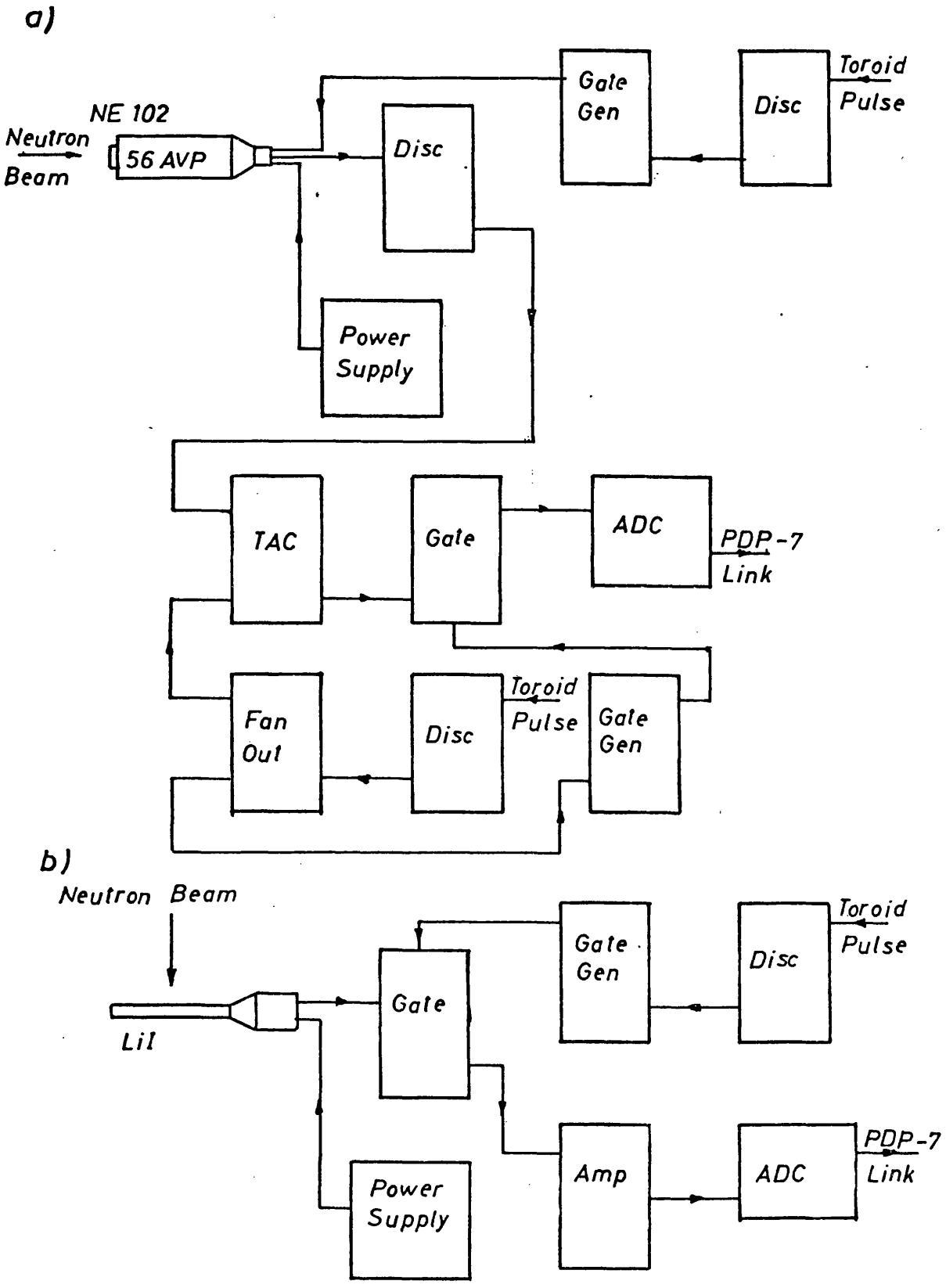

Pict.27: a) Electronic Setup For the Incident Flux Monitor
b) Electronic Setup For the LiI Detector

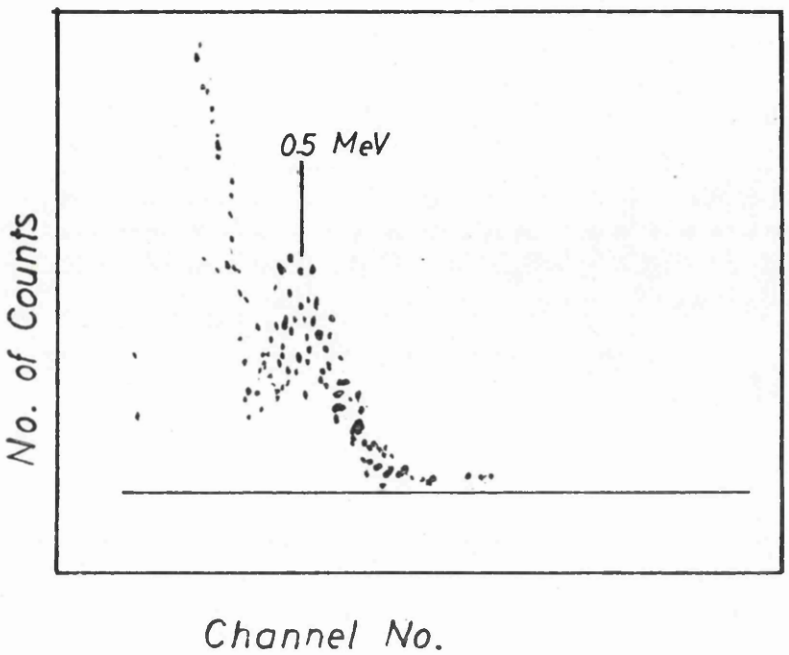

Pict. 28: Ungated Am-241 Pulse Height Spectrum

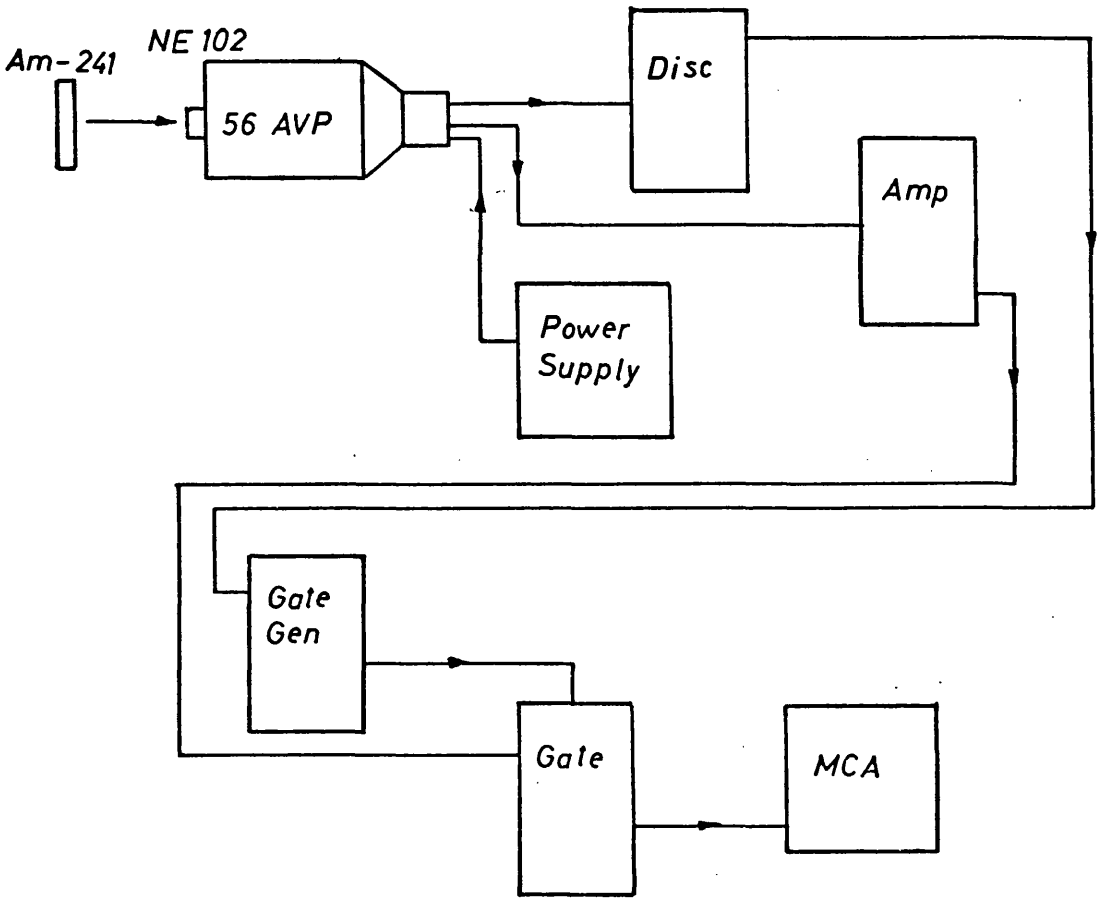

Pict. 29: Electronic Setup For Discriminator Bias Measurement

gate is in operation, it will only let pass ampliefied dynode pulses, exceeding the discriminator bias level. The effect of this can be seen in pict. 30. If the gate is open, a spectrum, according to pict. 28, is accumulated in the pulse height analyzer.

Since the peak energy is known as 0.5 MeV, resp. 60 keV γ-ray or electron energy, the cutoff in the leading edge of the gated spectrum can be calculated. In the present case this channel in the pulse height spectrum corresponded to 11.1 keV electron energy. To convert this to neutron energy, a calibration graph by J. B. Czirr et al.[39] was used, and the corresponding neutron energy for the bias level was 0.255 MeV. This is not only important for the determination of the spectrum range in the incident flux used, but also eventually for the calculation of the monitor detector efficiency.

3.6 Two Parameter Data Storage

The fast discriminator for the gas scintillator time pulse was set to exclude mainly noise, so that α-particles were also counted in the data store together with fission fragments. This was neccessary because it was a priori difficult to decide where to set a threshold. This again necessitated a mode of data taking, which allowed an a posteriori setting of the threshold. The obvious way of doing this, was to collect time pulses in coincidence with their linear pulse amplitude. In this way a matrix would accumulated, and slices of it could later be selected for further analysis. Two conditions for this mode had to be fulfilled. Firstly, the time-and linear pulses, belonging together, had to enter a dual ADC in coincidence. This was

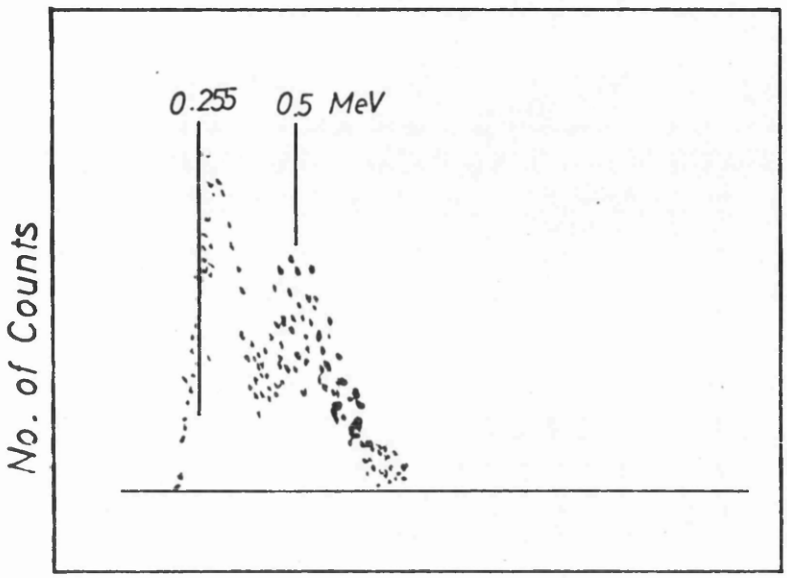

Pict.30: Gated Am-241 Spectrum

achieved by the use of a delay amplifier in the linear circuit. Secondly, a computer facility together with a programme for this mode of data taking had to be available. The computer was a PDP-7, and the programme had been developed previously by J. D. Kellie and G. I. Crawford [40]. This programme must also allow for simultaneous storage of the two monitor spectra in usual multichannel analyzer mode.

Pict. 31 shows the layout of the Kelvin Laboratory PDP-7 computer with its main features. The TAC pulses together with the amplified linear pulses arrive at the same time at the ADC. This ADC accepts only an input in one channel (X), when there is a simultaneous input in the other channel (Y). If only one pulse arrives, it will only wait 8 μsec. for a corresponding pulse, after which the two pulses are then processed to the computer. A prior hardware coincidence of these pulses is therefore necessary. After both pulses have arrived, they are then fed to the buffer to the computer memory. The display is made for the entire X or Y regions, i.e. X in coincidence with all Y channels and vice versa. The pulse amplitude pulses went into 256 channels and the time pulses into 512 channels, so that the total matrix size was X . Y = 256 x 512. When the buffer was filled with 1024 coincidence pulses, its contents was automatically read onto a DEC-tape, where it was stored as the same matrix for later processing. Control of the PDP-7 was exercised from a Console teletype. Further output facilities were a paper tape punch and a fast link to the Kelvin Laboratory PDP-10 computer. To load the programme, a paper tape was read in by the paper tape reader to select it from

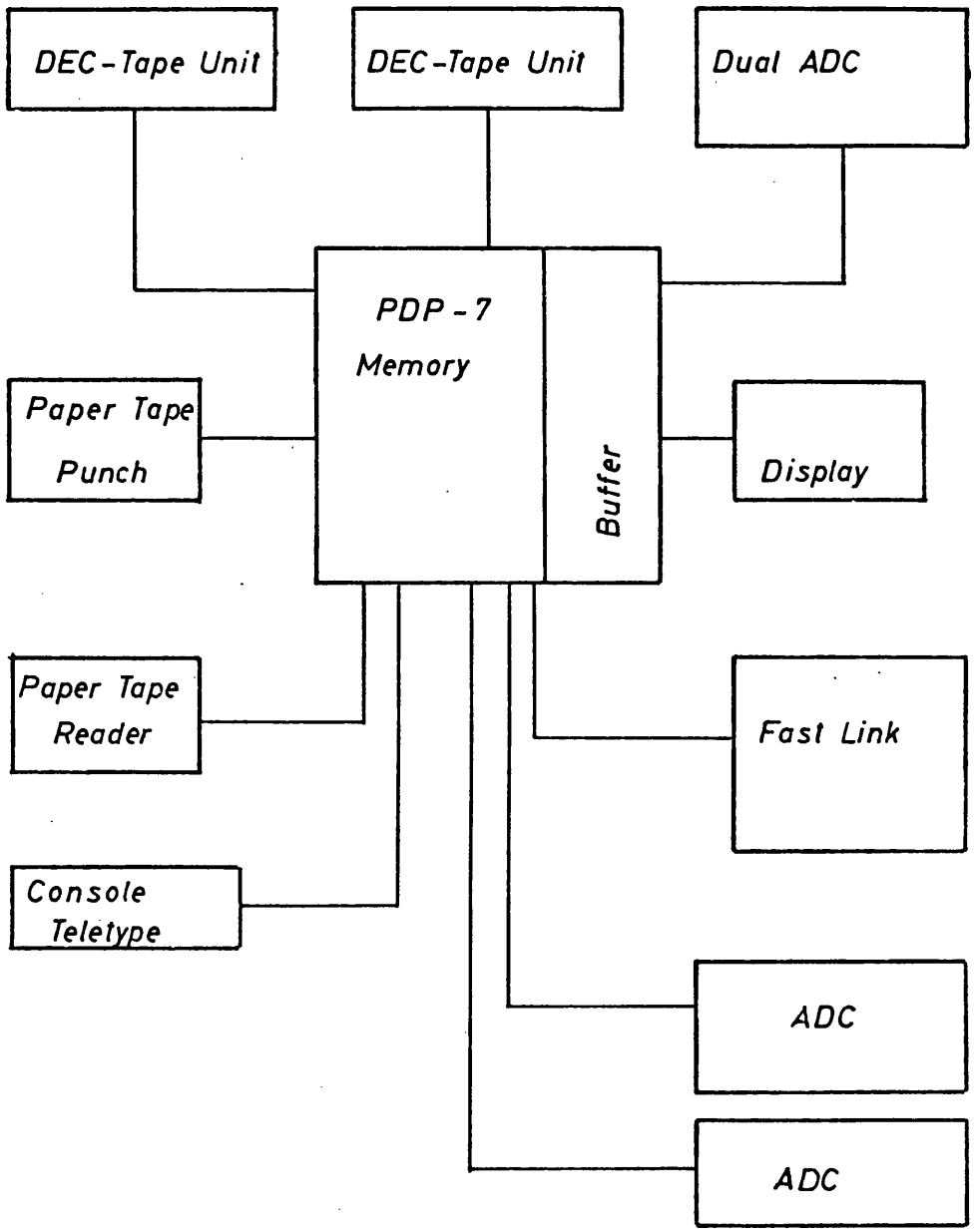

Pict. 31: PDP-7 Layout

another DEC-tape on a separate tape drive. The data DEC-tapes were changed about every 5120 counts, to have separate data stores, and to be secure against accidental interference during storage for the bulk of the data. Pict. 32, 33, 34, and 35 show typical pulse height and time spectra, accumulated during the experiments for U-235 and U-238 fission. The console-teletype itself printed out the number of counts, transferred to the buffer in 1 or 5 min. intervals. This was neccessary for check of operation and for normalization during later analysis.

As already indicated, the memory of the PDP-7 accepted also the monitor spectra from separate ADCs in conventional multichannel data storage into different data regions, each consisting out of 1024 channels, but not on DEC-tape. To release these data, the other peripheral installations had to be used. Pict. 36 and 37 show the monitor spectra. Since the count rates of the monitors were also printed out by the teletype, a true running time comparison for them and the fission spectra was not necessary, after sufficient statistics had been arrived at. The different running times for the main detector and the flux spectrum monitor could be normalized against each other by taking the outprint times into account later.

To exclude electronic noise from the TAC's, thresholds could be set at the ADC's themselves. Both TAC's were set at a pulse amplitude range of 8 V, corresponding to 4 μsec. for the gas scintillator TAC and 8 μsec. for the main monitor TAC. This gave

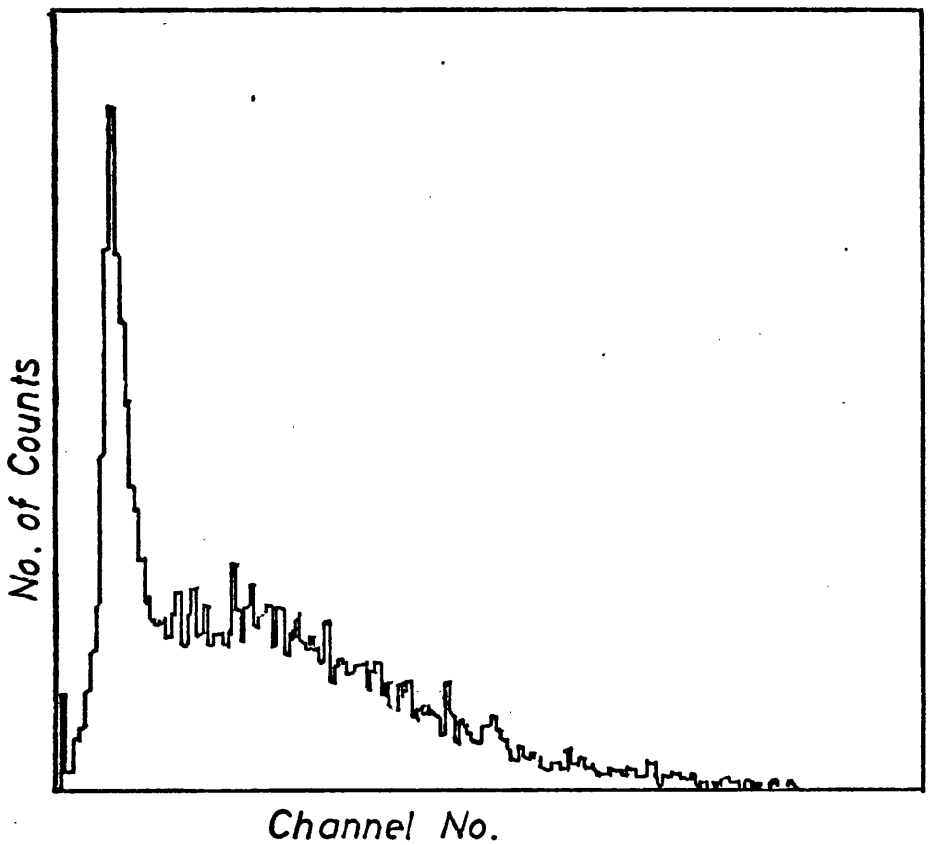

Pict. 32: U-235 Pulse Height Spectrum

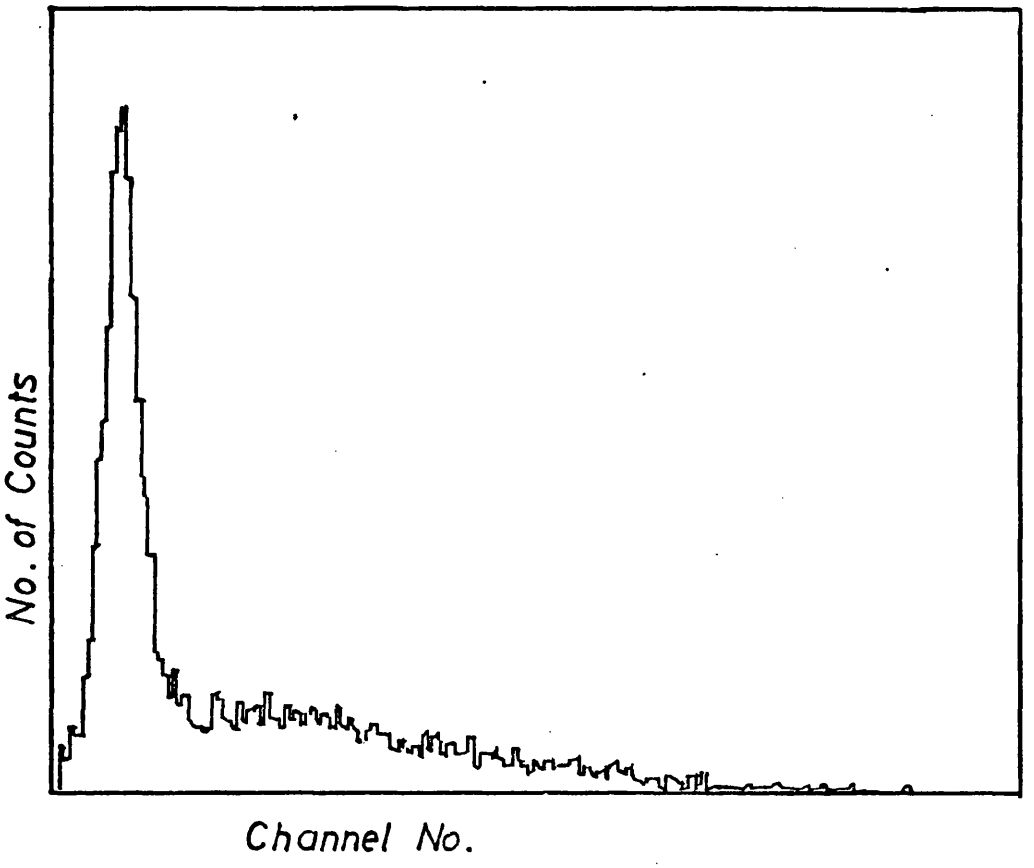

Pict.33: U-238 Pulse Height Spectrum

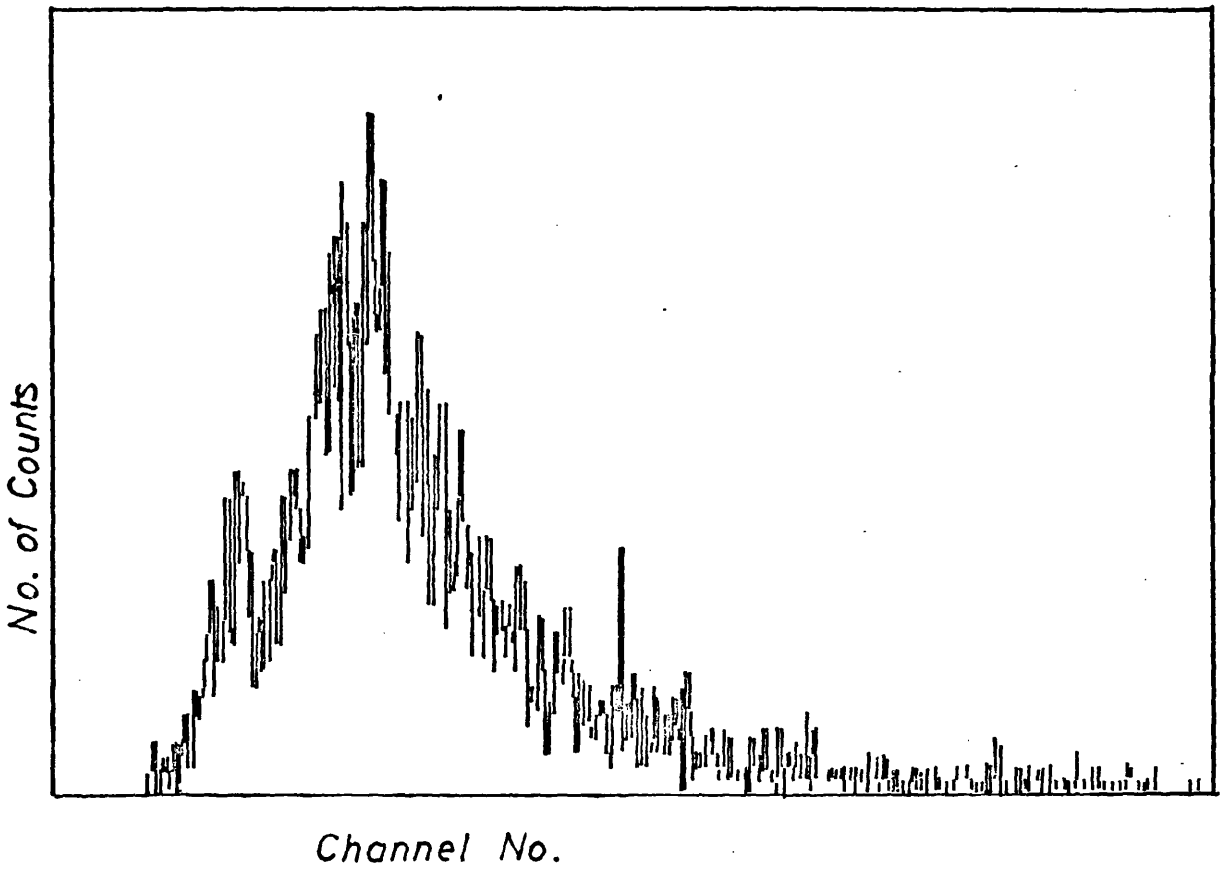

Pict. 34: U-235 Time Spectrum

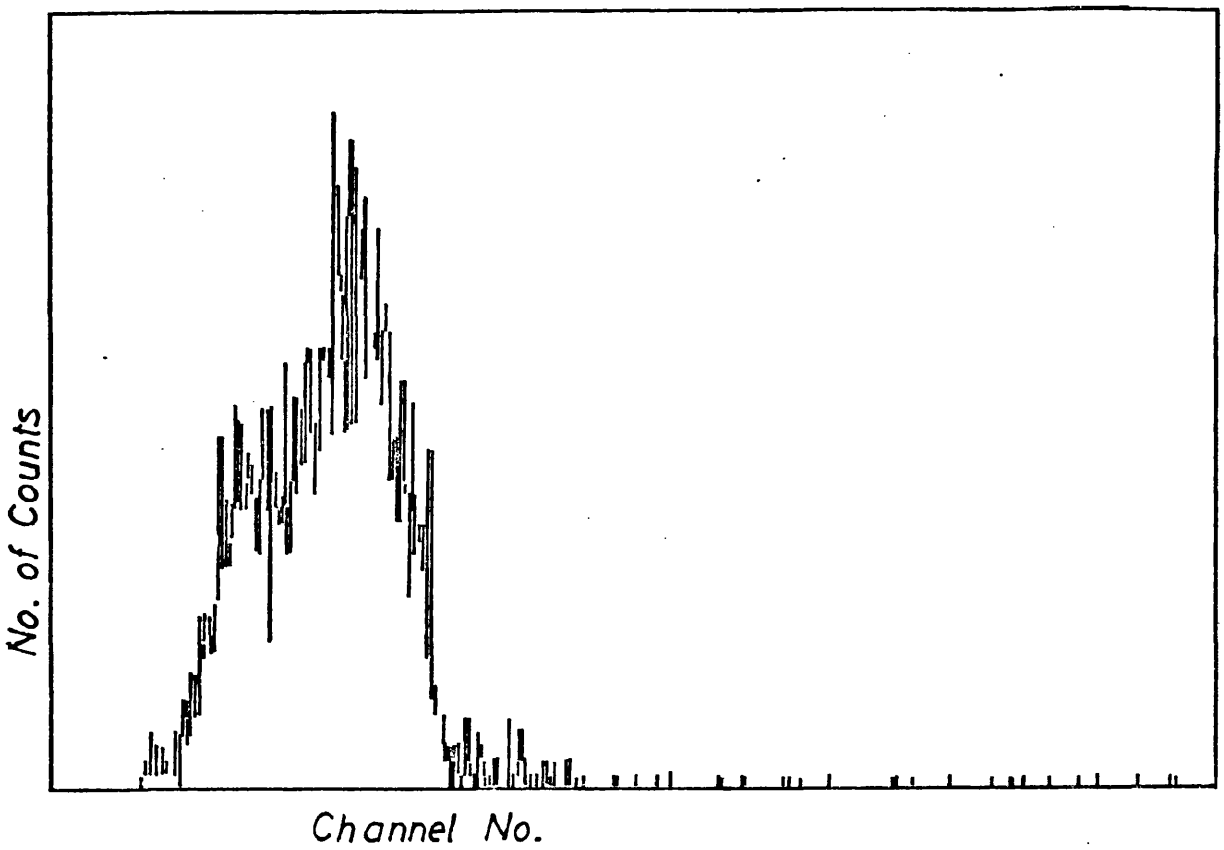

Pict. 35: U-238 Time Spectrum

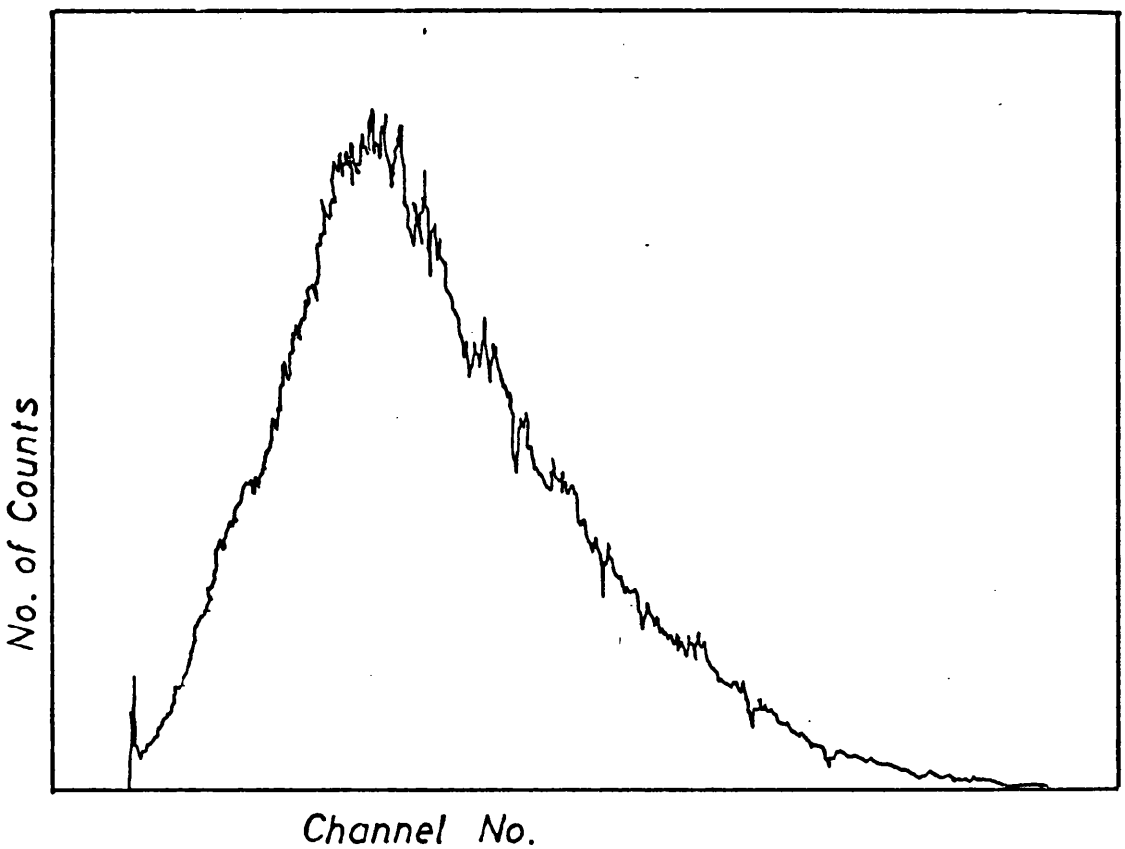

Pict.36 : Incident Neutron Flux

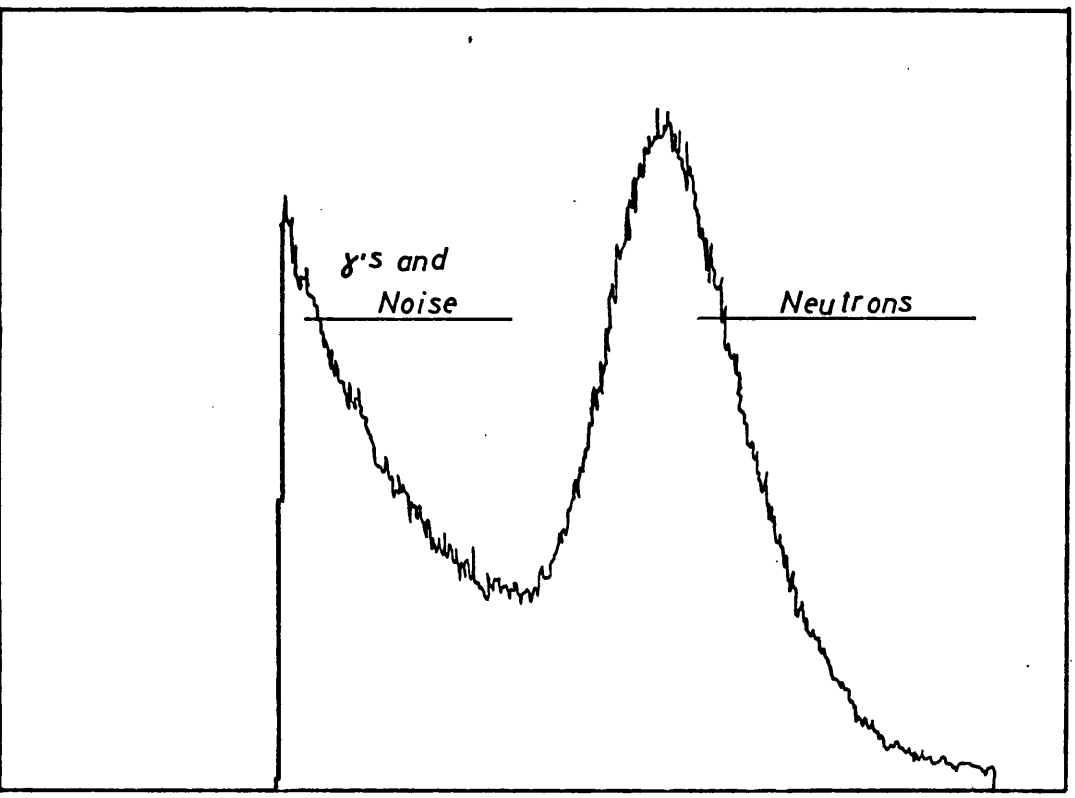

Pict.37: Neutron Pulse Height Spectrum Measured By the LiI-Detector

a rough estimate of the time calibration of the multichannel data region.

The processing of the bidimensional fission event matrix will be described in the following chapter.

3.7 Time Resolution of the System

When considering the time resolution, one has to take into account both the resolution of the flux monitor and that of the gas scintillator. The important one, however, is the one for the gas scintillator, because the number of counts in the fission time spectra were far less than the number of counts in the monitor spectrum. It was therefore necessary to increase the bin-width of the data region for the fission counts, to increase its statistical accuracy. This meant, that the resolution of the fission time spectrum was well within that of the monitor spectrum, and the resolution of the final cross section was mainly determined by the gas scintillator contribution. The individual contributions were as follows:

a) the neutron flux monitor detector:
previous experience[24] shows that

$$\Delta t_{Mo} = (\sigma t_{bp}^2 + \sigma t_{de}^2 + \sigma t_{cw}^2)^{1/2} \qquad (3.7.1)$$

where Δt_{Mo} is the total FWHM for the monitor detector; σt_{bp} is the

width of the accelerator beam pulse, which was taken as 3.5 ns; δt_{de} was the spread due to the detector and electronics, taken as 1.5 ns, and δt_{cw} was the channel width of the multi-channel data region, and this was 3.13 ns. So the total FWHM was about 4.9 ns.

b) the gas scintillator circuit:

$$\Delta t_{gs} = (\delta t_{bp}^2 + \delta t_d^2 + \delta t_e^2 + \delta t_{cw}^2)^{1/2} \qquad (3.7.2)$$

where δt_d is the detector spread; δt_e is the spread due to electronics. A measurement of the time distribution of the γ-flash revealed, that Δt_{gs} could not be higher than 7.9 ns.

The impact of the time resolution on the energy resolution will be discussed in the following chapter.

3.8 Alpha-Background and Afterpulsing

Although every care was taken to reduce the γ-flash signal in the gas scintillator as much as possible, its intensity still was sufficient to produce a small amount of afterpulsing in the 58 UVP photomultiplier. This can clearly be seen from pict. 34 and 35, where the first peak represents after-pulsing in the time spectra. There was, however, no clear evidence of it from the total pulse height spectrum. To determine its pulse amplitude, a background run was undertaken with the Cf-252 source in position. Because of the accelerator duty cycle very few natural fission events from this source could be recorded

during accumulation. The amount of neutron-induced fission in the source, which had only a mass of 1 $\mu g/cm^2$ and a diameter of 1", was also negligible. The result of the background run is presented in pict. 38. The time spectrum shows a typical after-pulsing distribution, which is related to a rather narrow small amplitude region, submerged in the α-peak. Thus it would be possible to subtract these pulses during later analysis.

During the experimental run the α-countrate was much smaller than the actual decay rate of the target material because of the accelerator duty cycle. Also, the α-particles are clearly separated from the fission fragments, to enable later discrimination against them, because they also appear in the time spectrum randomly distributed.

3.9 Time Calibrations

For the conversion from time to energy in later analysis it was neccessary to know the time scale of the TAC-multichannel data region system.

As a rough guide the TAC settings could be taken. They were 4 μsec. for both TAC's, and from those about 4 ns per channel was expected for the main monitor detector region, which covered 1,024 channels and about 8 ns per channel for the gas scintillator region, spreading over 512 time channels. However, a precise time calibration was required. This was done with a Tennelec (TC-850) Precision Time Calibrator, which uses correlated pulse pairs and has been described by other authors [41].

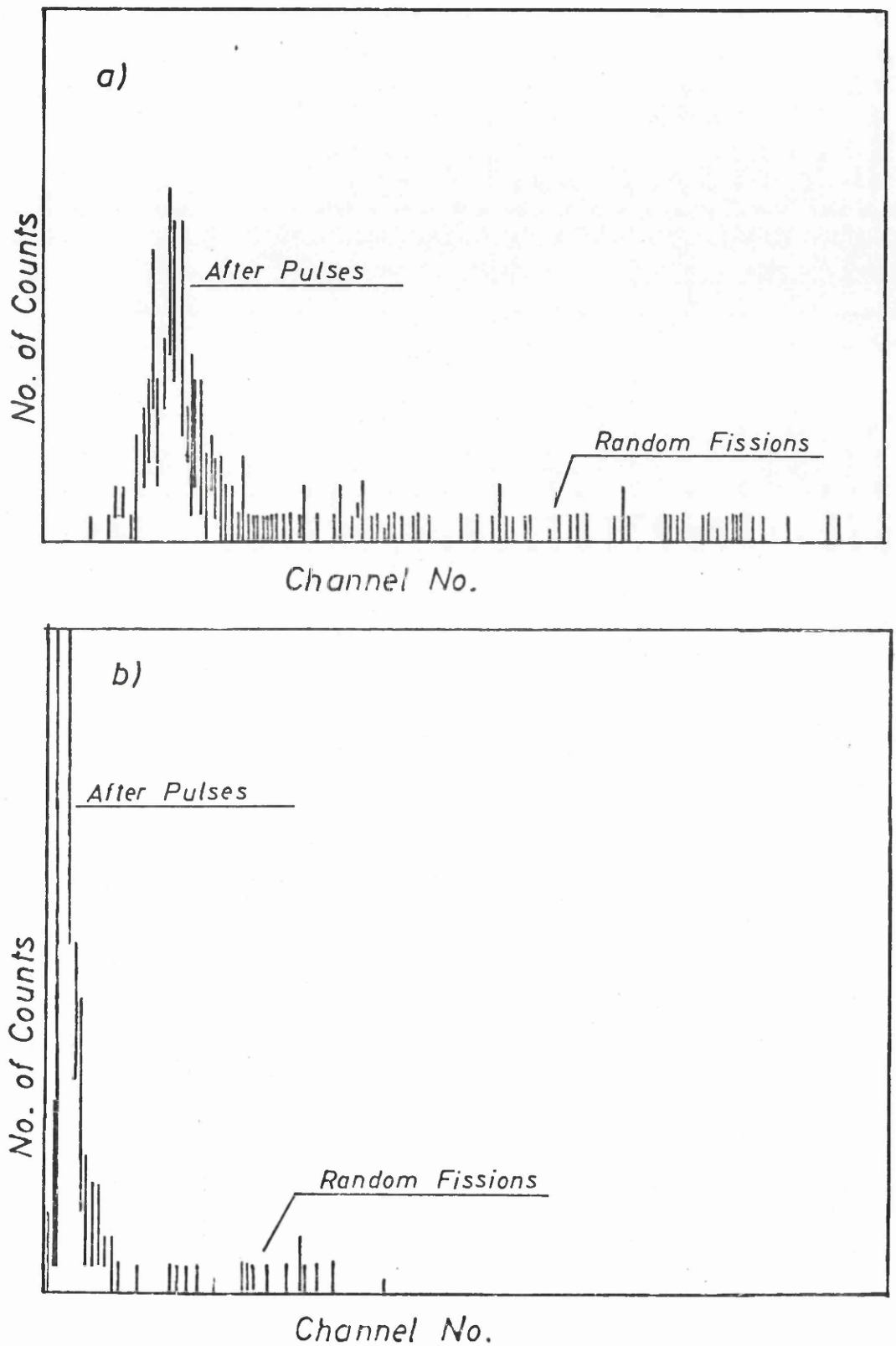

Pict. 38: Background Spectra
a) Time
b) Pulse Height

The Tennelec Calibrator is mainly a quartz oscillator and provides a start and a stop pulse for a TAC, which are synchronized and are produced periodically, separated by a selectable period. Each integral multiple of this period gives a peak in the calibration spectrum. Pict. 39 shows such a spectrum. The setting of the calibrator was 160 ns per period. From the peak spacing thus the time per channel could be calculated and it was 3.13 ns per channel for the monitor region and 7.9 ns per channel for the gas scintillator detector region. The absolute calibration is described in the following section.

3.10 Absolute Energy Calibration

For the transformation of time spectra to energy spectra it is not only essential, to know the time calibration of the spectra, but also at least one particular channel to which an absolute energy point can be related. For the two detectors there were two different methods, by which this could be achieved:

a) the neutron flux detector:

in this case a so called Carbon-calibration was obtained. A thick 12 cm piece of Carbon was put in the neutron beam right in front of the detector, and a time spectrum of the neutron flux, reaching the detector, was taken, until the well-known [42,43] Carbon absorption lines appeared. This spectrum is shown in pict. 40. It was then possible, to identify sufficient lines to relate a particular energy to a certain channel.

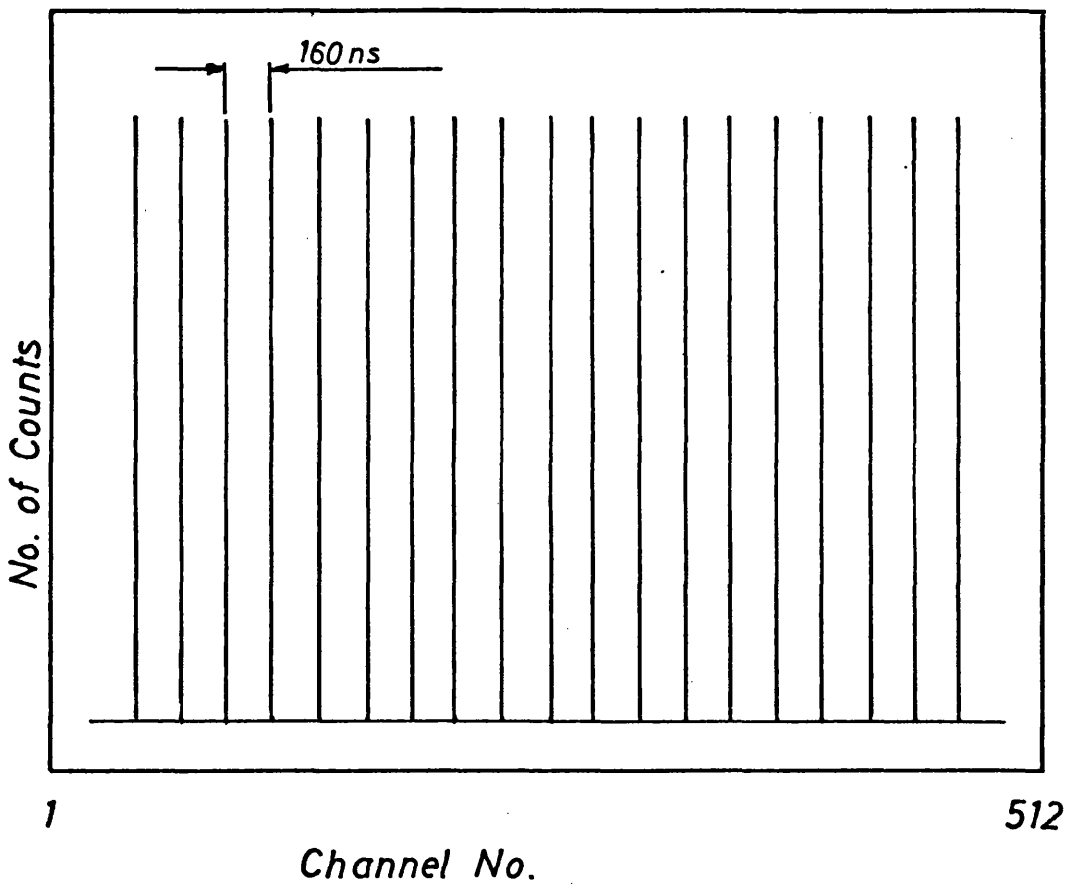

Pict. 39: Time Calibration of the Gas Scintillator Data Region

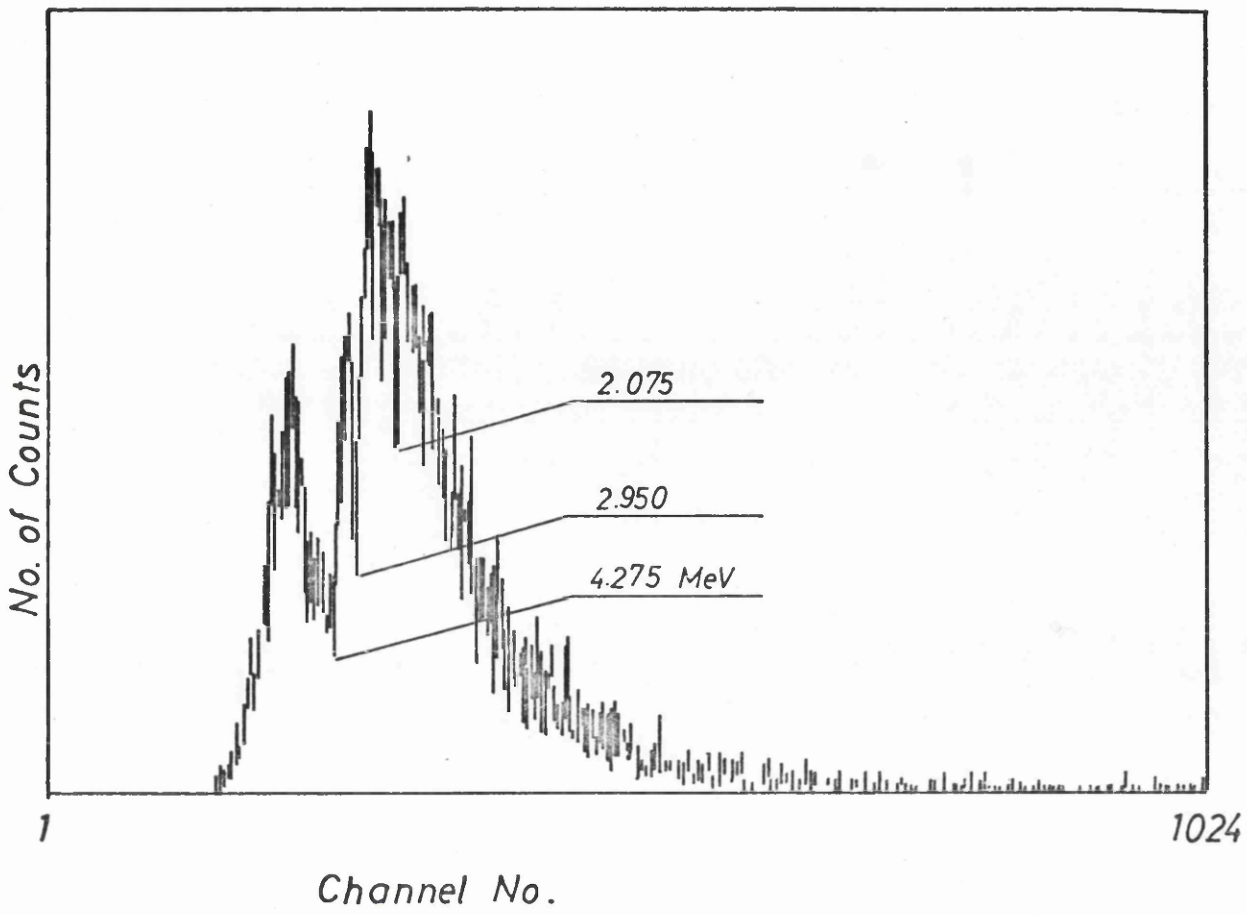

Pict.40: Carbon Calibration of the Incident Flux Monitor Detector

b) the gas scintillator detector:

since the counting rate for the fission spectra was so low, that a Carbon calibration would have taken the equivalent of the time of the experiment itself, other means of determining energy points had to be resorted to. This was done with the help of the γ -flash. Firstly, all gates were opened, to let the γ -flash pass. It was recorded in an early channel in the time spectrum. Knowing the length of the flight path, the absolute time for the γ -flash channel could be calculated. The channel was no. 20, and the time was 65.87 ns. To check this, a calibrated cable, providing a known delay, namely 450.5 ns, was introduced, through which the stop pulse - in this case the γ -flash - had to pass. This gave a second channel in the time spectrum, in which the γ -flash appeared, channel 77. corresponding to a time of 516,37 ns. From the channel and the time spacing between the two γ -flash channels the time-calibration with the Tennelec unit could be checked.

How to relate these absolute time channels to energy, will be shown in the following chapter. Pict. 41 shows the gas scintillator region absolute time calibration.

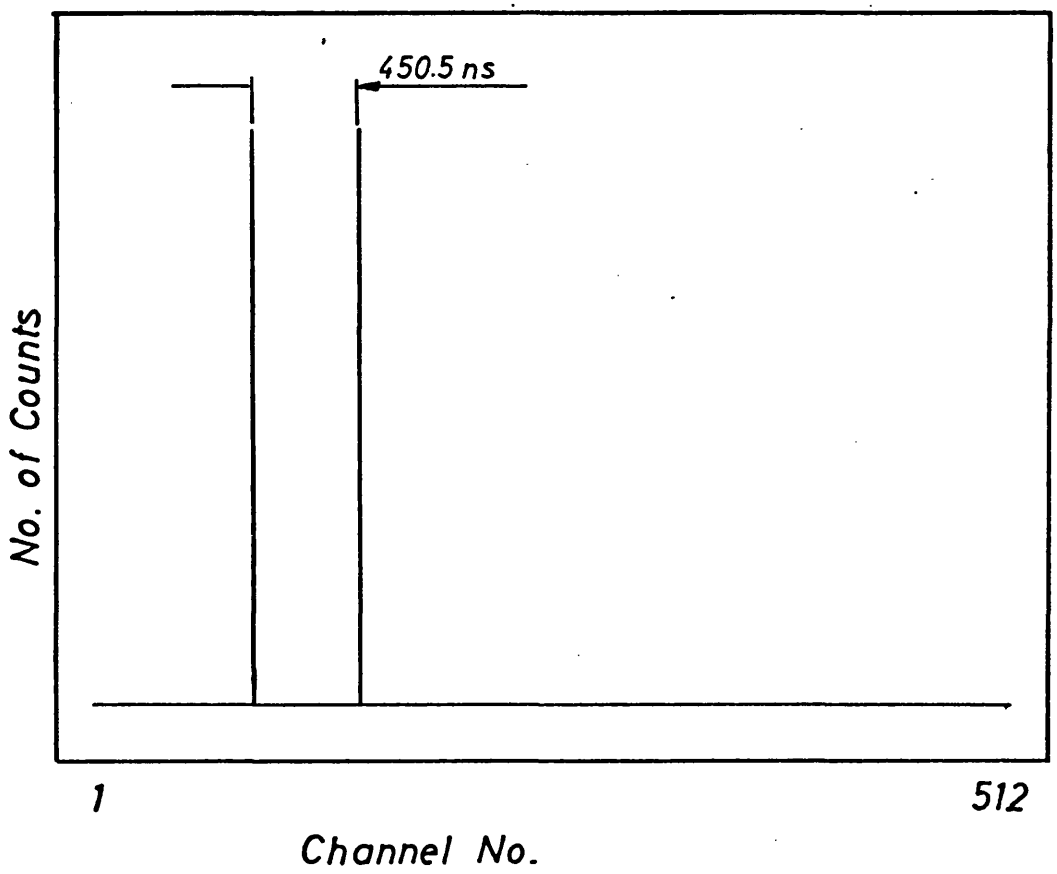

Pict.41: Absolute Time Calibration With the γ-Flash of the Gas Scintillator

CHAPTER IV

4.1 Introduction

The analysis of the data was very much determined by the way of data taking and did therefore not follow normal procedures for direct time-of-flight measurements. Important was the bidimensional accumulation of the fission spectra, and that there were no alternate target-in-target-out runs as for example in total cross section measurements. Because of the low attenuation in the fission detector, the incident flux could be monitored at the same time as the fission events. These two factors determined mainly the way of eliminating background and the final calculation of the cross sections.

For general data handling and all calculations the large PDP-10 computer network of the Kelvin Laboratory was available, although part of the background subtraction was done on the PDP-7 computer itself. The conversion from time to energy was the only standard procedure of the whole analysis. In addition to the pure calculation of the cross sections by a standard formalism a normalization had to be made for the detector geometry. To estimate the absolute value of the cross sections, an estimate of the number of lost fragments due to straggling and absorption in the target foils had to be made. The other important contribution to the final cross sections was the efficiency of the flux monitor detector. After all corrections the calculation of statistical errors and energy resolution could be made. A final normalization proved to be necessary, before the cross section could be presented.

4.2 The PDP-10 Computer Net Work

Except for background subtraction, which was done on the small PDP-7 computer, all data analysis was done on the Kelvin Laboratory PDP-10 computer. The complete system is shown in pict. 42. The small PDP-7 and PDP-8 computers are connected to the PDP-10 via fast links, as described by A. D. Wilkinson et al.[44]. These links are necessary to transfer large amounts of data, for which paper tapes become impractical.

During the normal course of data handling and analysis the original data are stored on DEC-tapes, as described in subsection 3.6. After background subtraction the resultant files are then transferred onto the user's disk-area to the PDP-10. There the further procedure of analysis takes place. Intermediate data storage can be done on magnetic tapes or simply on the disk-area itself. Programming and data handling is done directly from the keyboard of visual display units (VDU's) or teletypes. A systems routine named CUPID enables the immediate plotting and display of data on the VDU's, when the data are in the specified format. The VDU display can be directly preserved by a hard copier.

The interaction between user and PDP-10 computer is organized by a time-sharing system[45], which enables the simultaneous use of the computer by several users. According to a priority key, users are swapped in and out of the core during attachment to the system, so that a maximum amount of core is available to everyone at a time. The use of the peripherals is organized in the same way.

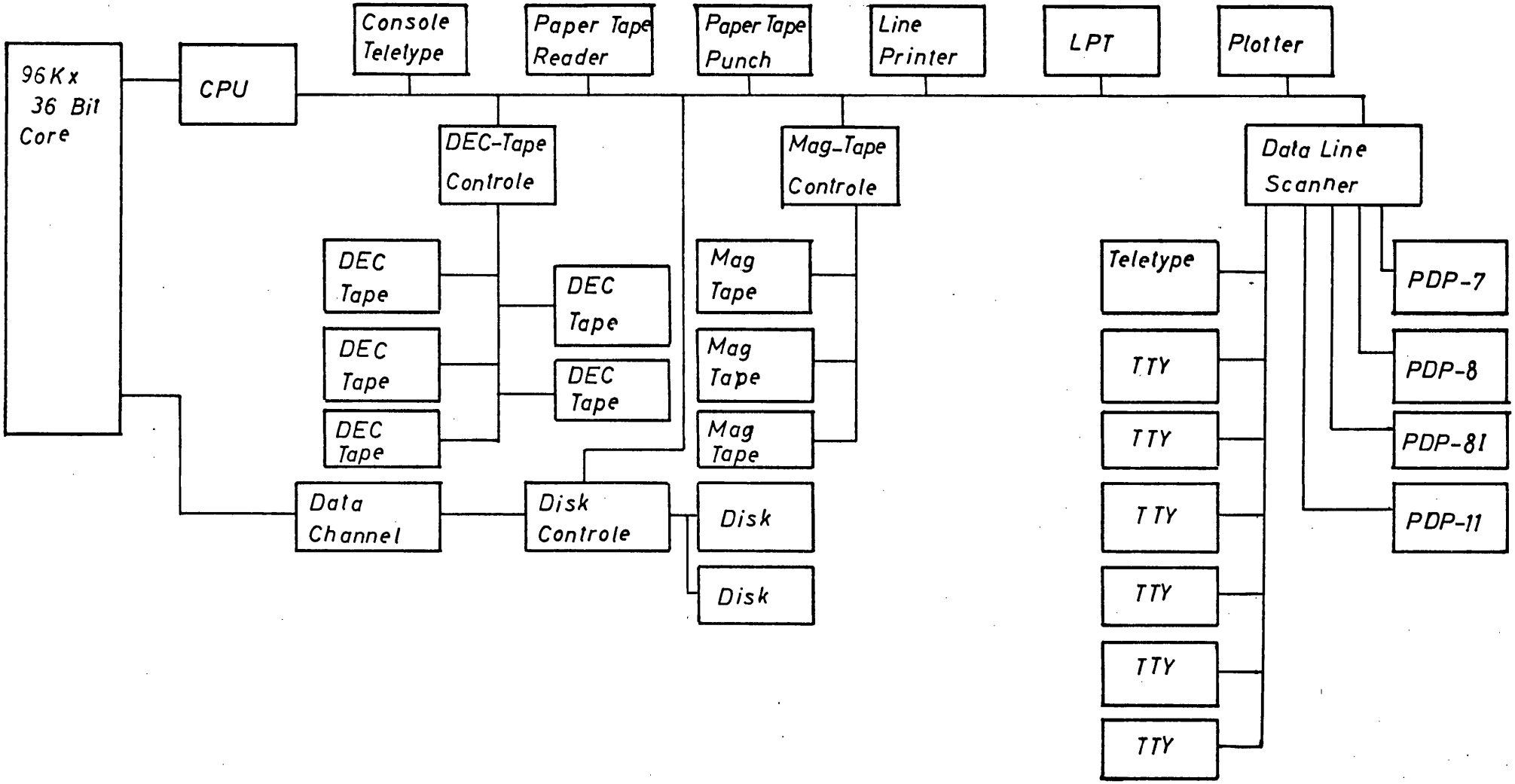

Pict.42: The PDP-10 Computer Network

If programmes are to be operated which take a large amount of central processor time, they can be run without attachment to a teletype or VDU by a system, called BATCH, which gives low priority to the user's programme, but runs it via a control-file, previously created by the user.

All final data, of course, can be printed out on a fast line printer or plotted by a calcomp plotter on graph paper.

4.3 Elimination of Background

The main sources for background were α-particles and after-pulses, as shown in pict. 43a. Both were confined to small amplitudes. The α-particle signals were randomly distributed over the time spectrum, whereas the after-pulses were confined to the beginning of the time spectrum. The obvious way of elimination of these disturbances was to only select time pulses, which were definitly in coincidence with large pulse amplitudes. This effectively sets a threshold in the pulse height spectrum. To exclude background, this threshold in principle could be anywhere in the region of the fission fragment amplitudes. However, it was desirable, to set it as low as possible, to gain the maximum information from the data files by including all fission events. Setting the threshold low, however, brought about the danger of accepting α's or after-pulses, being in the"tail-end" of their amplitude distribution.

It was decided, to define limits between which the required threshold definitely had to be. The lower pulse amplitude limit was the tailing-off

flank of the small pulses, as can be seen from pict 43b, and the upper limit was well above the valley, separating fissions and small pulses. This so defined region was then divided into sections, two channels wide each, thus increasing the lower limit steadily, until it coincided with the upper one. In this way a series of time spectra was obtained for steadily increasing threshold settings in the pulse amplitude spectrum. Since the data were stored in matrix form, it was possible to select these matrix slices by a special processing programme, earlier developed by J. D. Kellie [46].

The criterion, according to which the correct, i.e. the lowest possible threshold, was obtained, was the shape of the time spectra. Since the after-pulses tail-end was extending somewhat higher in amplitude than the α-signals, the correct threshold was reached when no further change in shape of the time spectrum occurred, when increasing the threshold setting. This could be investigated quantitatively, according to pict. 44. The time spectrum consisted of a major peak, and a smaller preceding one. The smaller peak was a mixture of true fission pulses and after pulses. When increasing the threshold in the pulse amplitude spectrum, the first peak decreases, whereas the main peak stays constant. For each threshold the ratio of the two peaks was taken. After this ratio remained constant, it was assumed that all after-pulses were excluded. To have a safe margin, the actual threshold, to be used for time spectrum for further analysis, was selected as two channels above the one, from which onwards the peak ratio stayed constant.

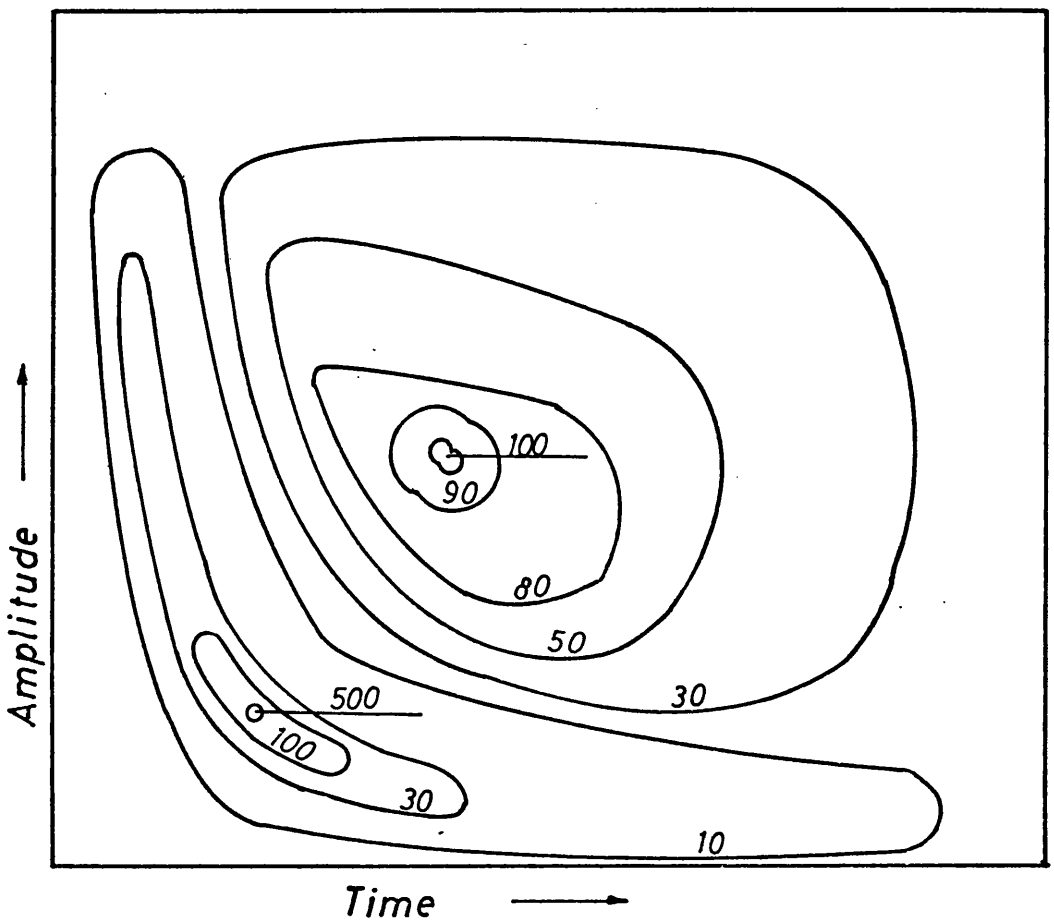

Pict. 43 a): Example of Linear Pulse Height Versus Time For a Fission Spectrum (Connected Lines Refer To Equal No. of Counts)

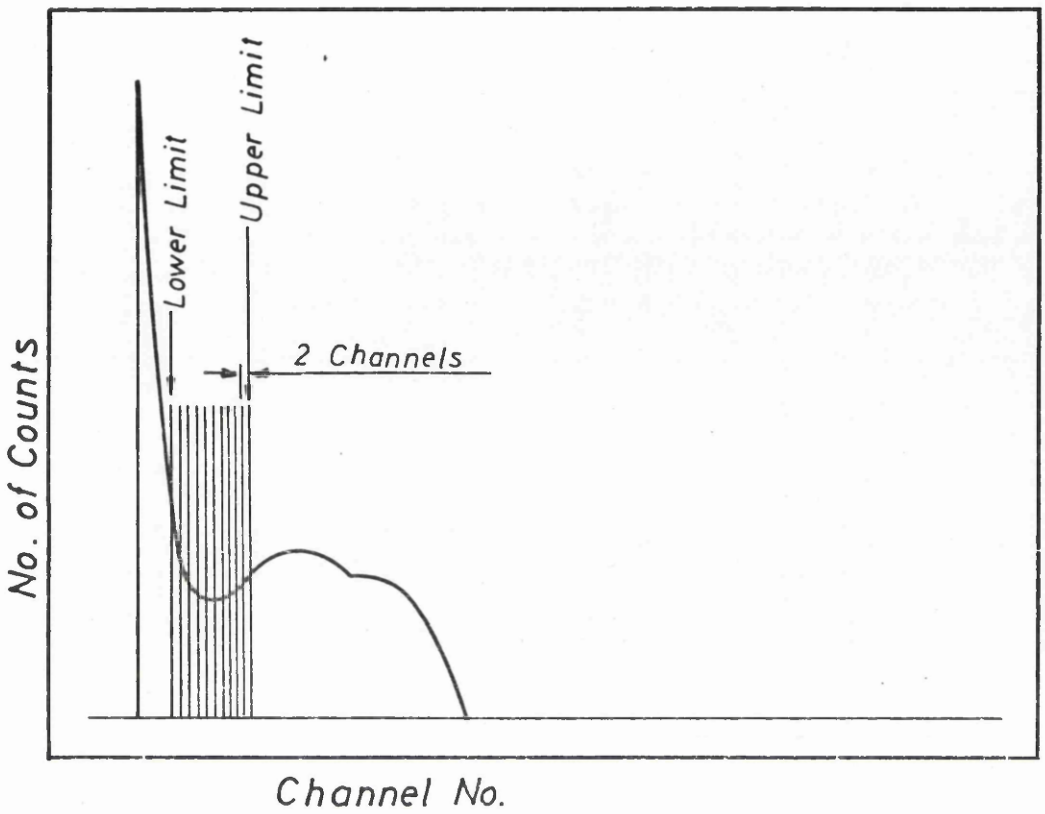

Pict. 43b): Illustration of Threshold Selection

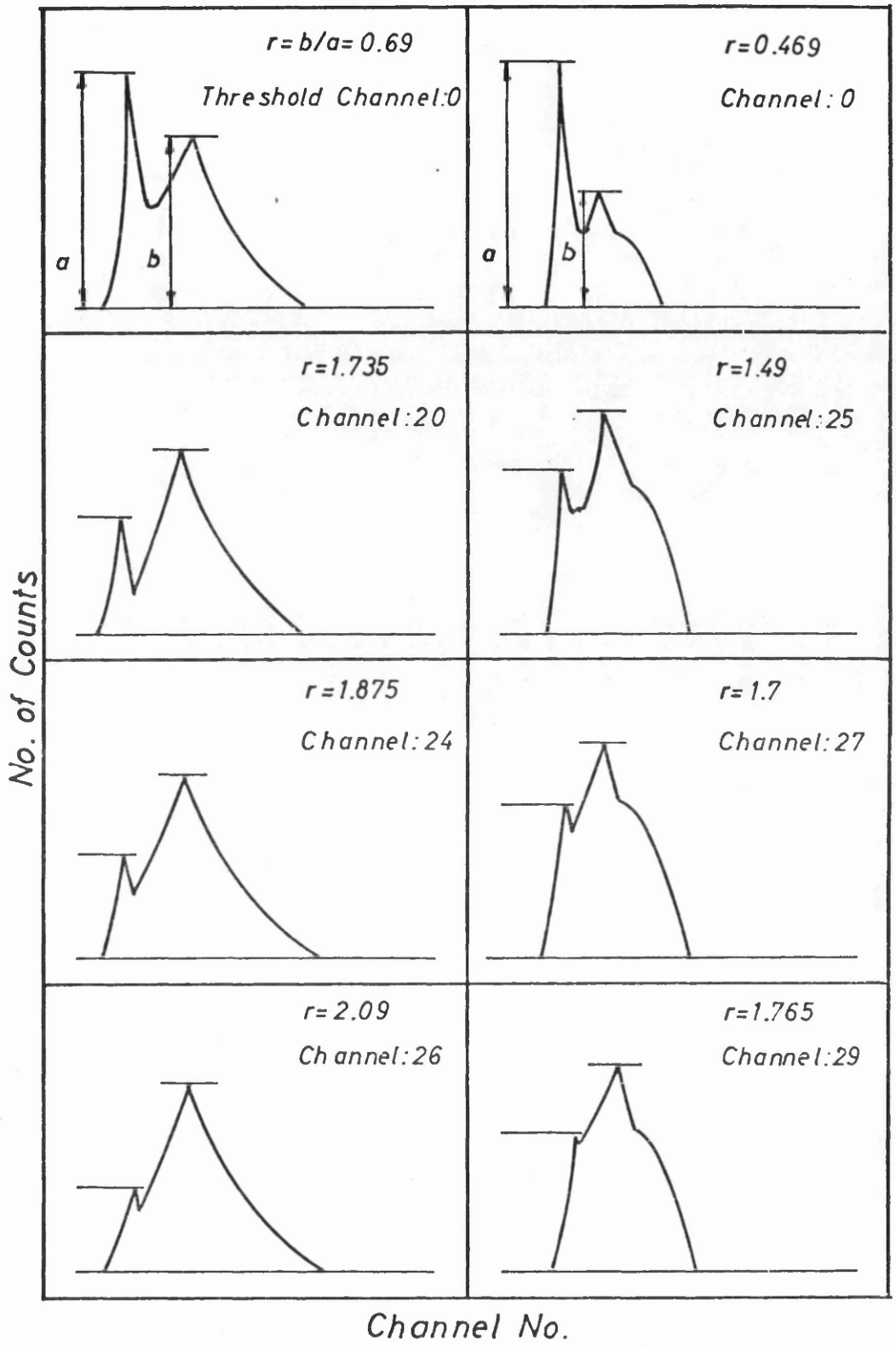

Pict.44: Fission Time Spectra In Coincidence With Different Pulse Amplitude Threshold Settings (Left: U-235, Right: U-238)

The thresholds were different for the U-235 in respect to the U-238 spectra. It was channel 26 for the U-235 spectrum and channel 29 for the U-238 one. Since the identical electronic settings were used for both isotopes, the only source of shift in pulse amplitude - apart from different α-energies (which plays no part in the shape of the time spectrum), can be slightly different gas conditions after target change, when a fresh gas filling had to be used. A change of 3 % in gas pressure, which was within the margin due to temperature variations, must account for a three channel shift in a pulse amplitude spectrum, covering more than 200 channels, due to the reaction of the γ-flash with the gas.

4.4 Conversion From Time to Energy

For the conversion of the background-subtracted time files to energy spectra a standard programme, called BIGEN, previously developed by J. D. Kellie[47], was used. It required as main input information besides the data file itself the number of nano-seconds per channel from the Tennelec time calibration, one specified channel with a particular energy from either the Carbon or the γ-flash calibration and the length of the flight path. The formula used was derived from the relationship between kinetic energy and velocity of a particle,

$$E_{kin} = \frac{1}{2} m v^2 \quad . \tag{4.4.1}$$

From this for a known path the energy is related to the time as

$$E = \frac{m d^2}{2 t^2} \tag{4.4.2}$$

Taking m as the neutron mass as 1.67482×10^{-24} g, d in m, t in ns, and converting this to MeV, E becomes

$$E = \left(\frac{72.3 \times d}{t}\right)^2 \qquad (4.4.3)$$

BIGEN was capable of producing energy bins, related to a required time resolution. The proper relationsh-ip between time and energy resolution will be discussed in subsection 4.10. Since, however, statistical differences were obvious for different energy regions, due to the shape of the incident flux and the shape of the cross section, it was decided, to define three regions with different resolutions, for the final presentation of the cross sections.

The first region extended between 0.3 and 0.7 MeV. It was not possible, to go much below 0.3 MeV in energy, because of the monitor discriminator threshold setting required to exclude noise, and because of the lack of many neutrons at that energy in the incident flux, which was a Maxwellian, peaking at about 2.0 MeV. Because of this lack the statistics per channel between 0.3 and 0.7 MeV were also poor for a binwidth of about 8 ns in the time spectrum, so that large fluctuations without any structural meaning would dominate the energy spectrum. Therefore the time resolution in this region was made 40.0 ns, integrating 5 channels at a time. Because there is no fission cross section for U-238 in this region, no data file for this isotope was of course created here.

The second region was between 0.7 and 2.5 MeV, and its time resolution was

20.0 ns, because the statistics were much better here, and this resolution was well above the instrumental one of 7.9 ns.

Although for higher energies the incident flux tails off again, and thus the statistical precision worsens, although not so rapidly as towards the lower energy end of the spectrum, it was decided, to halve the time resolution further, mainly because a large increment in time becomes a much larger increment in energy towards higher energies. Therefore, not to have too few energy points, statistical fluctuations were more readily accepted, and the time resolution of 10.0 ns between 2.5 and 12.5 MeV introduced. The upper limit of the energy range is entirely determined by the lack of a meaningful number of neutrons above this limit in the incident flux.

These three energy ranges and their respective time resolutions were entirely determined by the fission files, because no statistical problems existed with the numerical content of the monitor spectra.

4.5 Calculation of the Fission Cross Sections

The calculations of the fission cross sections was done in two steps. Firstly, it is considered, that an incident flux ϕ ($cm^{-2} s^{-1}$) strikes a target, containing N number of nuclei, and the cross section for the investigated reaction - in this case fission - is σ_f. The flux and the cross section are energy dependent. Then the reaction rate R (s^{-1}) is

$$R = \sigma_f N \phi . \qquad (4.5.1)$$

In these particular experiments N is the number of nuclei or atoms of U-235 or U-238 in the target foil, ϕ is respresented by the number of the events recorded in the monitor spectrum, and R by the number of fission events. However, some of the fission fragments are lost due to straggling and absorption in the foils, the targets were at an angle to the incident flux, the fission foils were larger in area than the face of the plastic scintillator, and monitor detector and gas scintillator were at different length of flight path. This all requires corrections and normalizations, grouped together in a single correction factor C. On the other hand the monitor had a certain efficiency E_{ff}, depending on the energy of the neutrons to be detected, i.e. the scintillator was only recording a fraction of the true flux, depending on the chance of interaction of an incident neutron with it, which in turn depends on the energy of this neutron. The various corrections and normalizations as well as the calculations of the NE 102 detector efficiency is presented in the following subsections. The final formula for the cross sections, however, is

$$\sigma_f(E) = \frac{N_{Xe}(E)}{N_{Mo}(E) N E_{ff}(E)} \times C \,. \qquad (4.5.2)$$

where N_{Xe} and N_{Mo} are the number of counts, recorded in the Xenon chamber and in the monitor detector resp.. C also contains a normalization, regarding the different times, for which both spectra were taken. The first step in calculating the cross section was, doing it without taking regard of the monitor efficiency. The

monitor efficiency was calculated separately and folded in later. It was not neccessary to correct for absorption in air or lead filters, because in the process of calculating the cross section, these effects cancelled out.

4.6 Normalization for Detector Geometry

As mentioned earlier, monitor detector and target chamber were at different lengths of flight-path. The target was also at an angle to the direction of the neutron beam, and the monitor scintillator face and target had different areas. Pict. 45 shows the complete geometry of the setup.

a) different length of flight-path:

since the intensity of the incident neutron flux was measured at a longer distance away from the centre of the neutron cell than the position of the target, this flux was more intense at the position of the target than the measured value. This intensity falls off in proportion to one over the distance squared. Therefore the ratio on the right hand side in equation (4.5.2) has to be multiplied by the square of the ratio of the Xenon chamber flight-path to the monitor detector flight-path.

b) angle of the target:

the incident flux is measured as neutrons per unit time and integrated over the area of the target. Since the target is at an angle of 45^{o} to the normal to the flux direction, its projection normal to the flux direction is that of an ellipse.

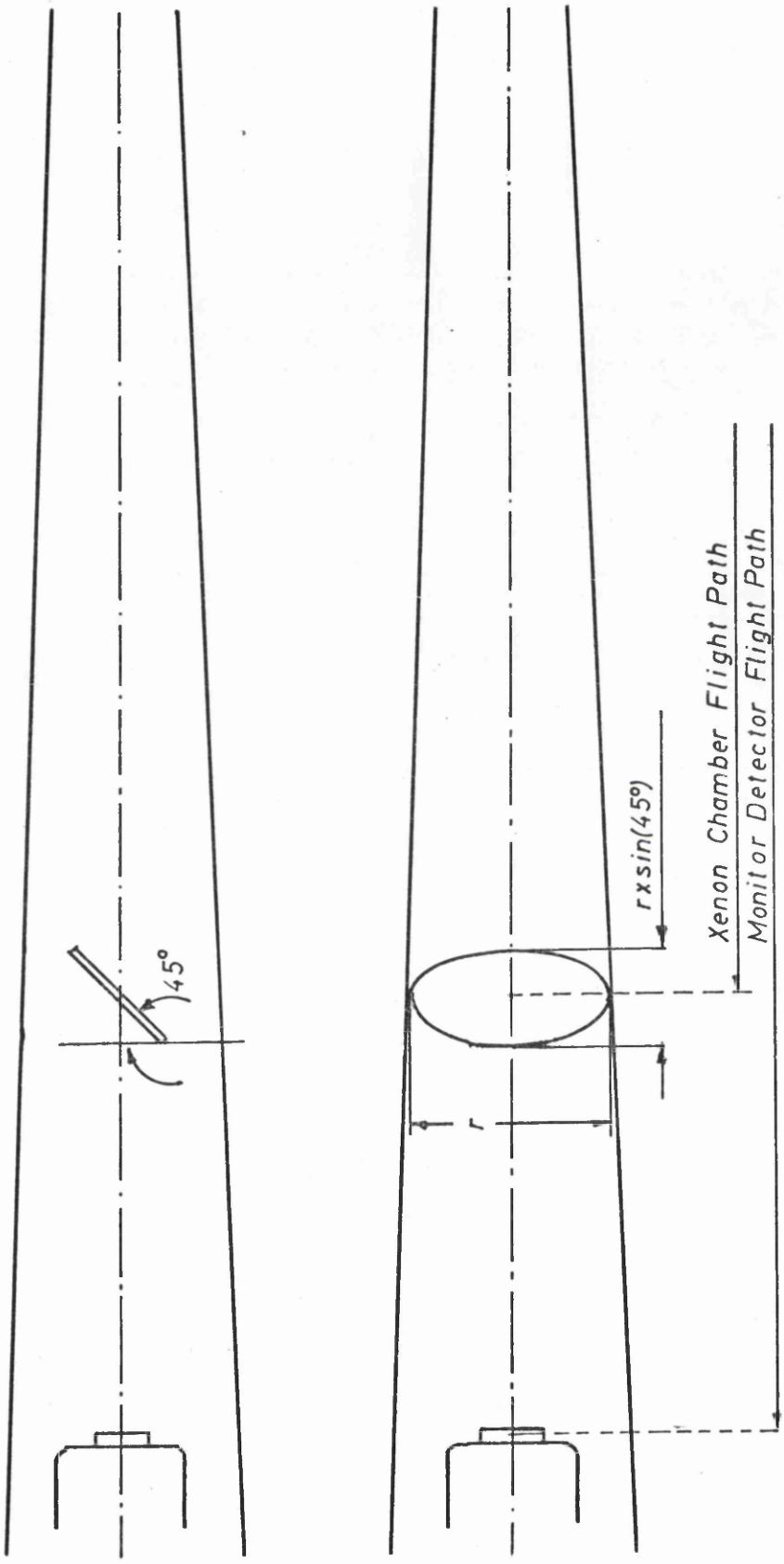

Pict.45: Detector Geometry

The area of this ellipse is given by the product of the two half axes times π . One of the half axes is the radius of the foil, the other the radius times sin (45^{o}). A second correction on the right hand side of equation (4.5.2) is therefore a division by sin (45^{o}) = 0.7071.

c) different target areas:

as mentioned under b), the flux is either integrated over a specific area or measured per unit time and per unit area. In both cases equation (4.5.2) has finally to be multiplied by the square of the ratio of the radius of the monitor scintillator face and the radius of the target foil, taking into account the correction for the angle of the foil to the beam under b).

All three normalizations make up for the factor C in equation (4.5.2)

4.7 Corrections For Lost Fragments

Since the target foils had a finite thickness, the fragments, escaping from them, loøse energy, except for those generated at the surface of the foil. Indeed, some of the fragments will loøse so much energy during the passage through the layer of target material, that they will not have enough energy left, to escape from the foil altogether. This is in particular true for the backing of the foil, which was so thick as not to let fragments escape at all. Here are the specifications of the foils:

U-235:

active diameter:	6.9 cm
thickness:	0.75 mg/cm^2 of 96 % U-235 as U_3O_8
backing:	3-4 thou." thick Platinum substrate

U-238:

active diameter:	7.6 cm
thickness:	1.0 mg/cm^2 of 100 % U-238 metal
backing:	0.1 mm thick stainless steel

Because the backing itself is in both cases thick enough, to stop all fragments escaping in that direction, the remaining concern is the loss of fragments in the active target layer itself.

There have been many calculations, regarding the loss of energy by a charged particle over varying distances in different media[27,28,29,48]. All developed formalisms include a certain number of uncertainties, and therefore a simple Bohr theory calculation, leading to an estimate of the number of fragment lost, as proposed by the California Radiation Laboratory[48], was adopted.

$$-\frac{dE}{dx}=\frac{4\pi e^4 Z^2}{mv^2}NZ\left[\ln\frac{2mv^2}{I}-\ln(1-\beta^2)-\beta^2\right], \qquad (4.7.1)$$

with

e = elctron charge

m = electron mass

Z = charge of the ion

NZ = number of electrons per unit volume of stopping material

$$\beta = v/c \qquad (4.7.1.1)$$

where

c = velocity of light

v = velocity of ion, and

I = mean excitation energy of the stopping atoms or molecules.

An integration over a specific distance, travelled by the ion in the material, gives the total energy loss over this distance. Knowing the initial energy of the fragments, it can be determined whether there is any energy left, or whether the fragment is stopped within the medium.

The whole calculation was done in a Monte Carlo programme, called KINEG or KINET for U-238. The target foil was assumed to be at 45^{o} to the beam. The target thickness was then subdivided into 100 small layers, starting with 1/100 th of the total thickness and subsequently increasing this step by step. At each layer fission events were assumed, randomly distributed over the total area of this layer. The fragments had an initial mass distribution as taken from measurements by W. N. Reisdorf et al.[49] for U-235 and M. J. Bennett and W. E. Stein[50] for U-238. These distributions assigned weighting factors to fragments with varying mass. For each ratio of light to heavy fragments of a particular event there is a total kinetic

energy release in this event, thus providing a corresponding initial kinetic energy distribution to the mass distribution[51,52,53,54,55]. From simple law of conservation of momentum the kinetic energies for single fragments were calculated. Although there is contradicting evidence about angular anisotropy of fission fragments to the direction of the incident neutron beam[56], more recent measurements have shown a certain angular dependence. This has been shown by R. H. Iyr and M. L. Sagu[57,58]. The authors proposed a formula, fitted to their observed data, to express the angular distribution of fragments:

$$W(\Theta)=A+B\cos^2\Theta+C\cos^4\Theta \,, \qquad (4.7.2)$$

where A, B and C are fitting parameters. For U-235 they are

A = 171.013

B = 267.921

C = -153.000

and for U-238

A = 132.129

B = 91.9328

C = -5.06948

The anisotropy factor is then defined as

$$F_a = W(0°)/W(\Theta) \qquad (4.7.3)$$

for each possible angle.

In this way the Monte Carlo calculation depended on the variation of the following parameters: fragment mass with a relative probability, according to their measured distribution, corresponding kinetic energy for a certain mass, angle relative to the neutron beam with a probability according to the anisotropies. The angle gave the length of the path in the material, which the fragments had to penetrate, to reach the surface of the foil. This path was further determined by the variation of thickness, according to the division of the total thickness into 100 layers.

The results of these Monte Carlo calculations were a loss of 31.2 % for the U-235 and 37.7 % for the U-238 foil.

However, the validity of these results is somewhat doubtful, regarding two parameters in equation(4.7.1):Z and I. Investigations of the initial charge distribution of fission fragments have shown[59], that there is little dependence of the inititial charge on the mass of the fragment, and that a value of 20 for this charge is a good average. This initial charge, however, is depleted during the transition of the fragment through matter, until, what is called an equilibrium charge, is reached[60]. This equilibrium charge is entirely dependent on the medium of passage and can assume values as low as 2 for fission fragments. The general relationship between charge and distance travelled at a particular initial energy for ions in solids is not fully known, and therefore an average ion charge of 11 was assumed for the calculation, neglecting the fact that the

energy loss is most significant for a high ion charge at the very beginning of the transition path.

The second factor of uncertainty is the excitation potential of Uranium or Uranium-Oxides. There are virtually no studies about the behaviour of outer shell electrons for Uranium or similar high Z elements. Apart from a few single absorption lines very little else has been measured. The only useful value, to be found, was 4.0 eV for Uranium in The American Insitute of Physics Handbook.[61] However, the mean excitation of an element has to be averaged or integrated over at least the outer shell electrons, if not including part of the electrons of a lower partly filled shell, which are more loosely bound for high Z elements. But since only single values of excitation levels are known, the value for the excitation potential, used in the present calculations, must be regarded as extremely doubtful.

Nevertheless, for an estimate of the number of lost fragments and therefore for the correction, to be applied to the cross section, the two discussed uncertainties were obviously acceptable.

4.8 Calculation of the Monitor Efficiency

The determination of the efficiency of the NE102 plastic scintillator is necessary to correct for the number of incident neutrons, not recorded by this detector due to finite reaction probabilities with neutrons as a function of energy. The main constituents of the detector, with which a reaction, an (n,p)-reaction, takes place, are the Hydrogen atoms,making up a high proportion of the organic scintillator compound. The reaction probability is therefore mainly

determined by the (n,p) scattering cross section. The other main partner in an organic molecule is Carbon, so that the total scattering Carbon cross section contributes also to reaction probabilities. Since a bias is set at the discriminator for this scintillator, to exclude small pulses, a portion of the recoil protons will produce pulses, large enough, to exceed this bias, whereas the remainder are ignored. Since the dimensions of the scintillator were small, multiple scattering effects could be ignored.

The model used to calculate the efficiency of this particular scintillator at this particular bias setting, was the one by O'Dell et al.[62]. This is the formula used:

$$E_{ff}(E) = \left\{ n_H \sigma_H(E) / (n_H \sigma_H(E) + n_C \sigma_C(E)) \right\}$$

$$\times \left\{ 1 - \exp\left[-(n_H \sigma_H(E) + n_C \sigma_C(E)) t \right] \right\} \left\{ 1 - (B/E) \right\} , \qquad (4.8.1)$$

where

n_H = Hydrogen atoms per cm^3

n_C = Carbon atoms per cm^3

$\sigma_H(E)$ = total (n,p) cross section

$\sigma_C(E)$ = total inelastic Carbon cross section

t = average scintillator thickness

B = Neutron energy bias

E = Neutron energy.

Pict. 46 shows the efficiency, calculated for a bias level of 0.3 MeV neutron energy for a NE102 plastic scintillator.

4.9 Calculation of Errors

The errors in the value of the cross section itself fall into two categories: the absolute error, being determined by the systematics of the experiment, and the relative statistical deviations. The systematic error will be discussed in the following subsection . There are also the energy resolutions.

a) statistical errors:

The incident monitor spectrum could be measured to any desired statistical accuracy, only limited by the fact, that the multichannel storage facilities would not accept more than 250,000 counts in one channel in a single run. The predominant source for the statistical uncertainties in the cross section was the fission spectrum, accumulated at a much lower count rate. As already pointed out, to increase the statistical accuracy over a given energy interval, several time channels were integrated. Taking this into account, the statistical deviations were calculated in the usual way as

$$\Delta\sigma = \sqrt{\sigma} \qquad (4.9.1)$$

The percentual error is then

$$f(\%) = \frac{100}{\sqrt{\sigma}} \qquad (4.9.2)$$

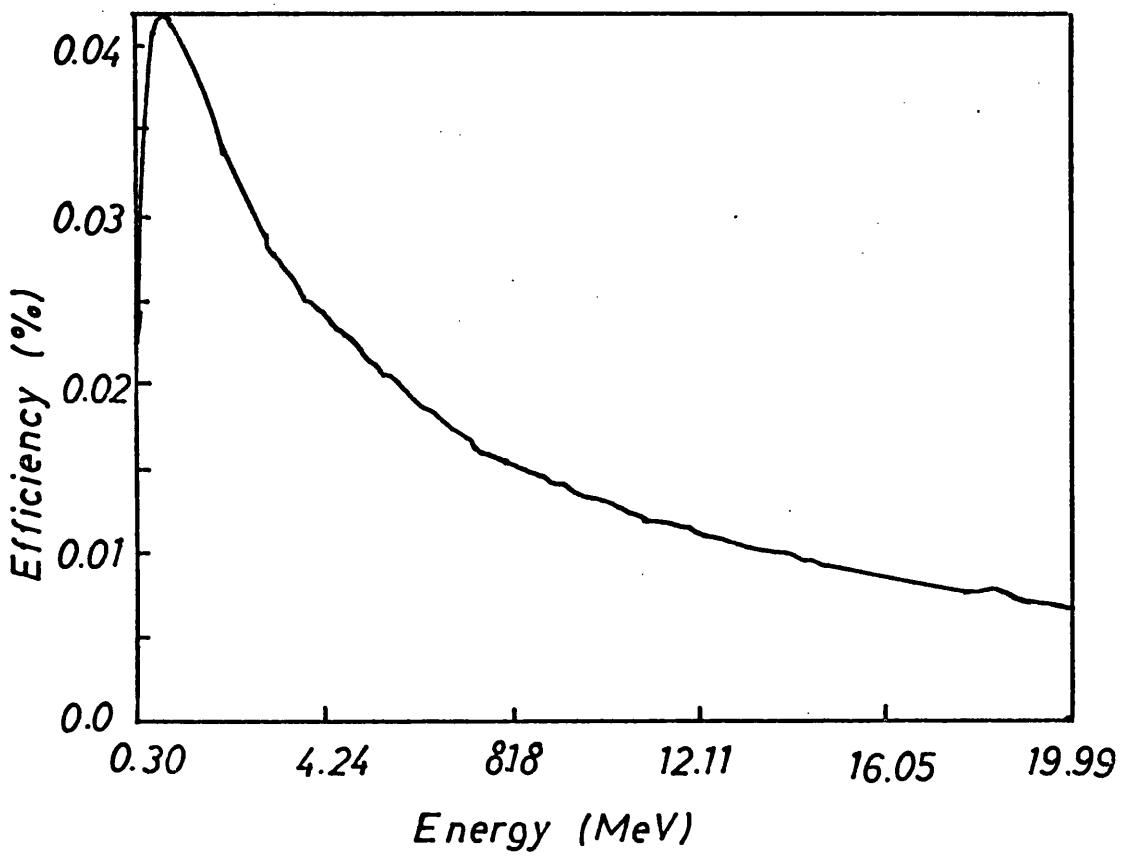

Pict.46. Example of an NE102 Efficiency
(Ø1.27x0.28cmxcm, 0.3MeV Bias)

b) energy resolution:

the relationship between energy resolution and time resolution can be determined by forming the first derivative of the energy over the time-of-flight-equation (4.4.3)

$$\frac{dE}{dt} = \frac{2E^{3/2}}{72.3\,d} \qquad (4.9.3)$$

and substituting dE and dt by $\triangle E$ and $\triangle t$. The whole expression can be simplified, by splitting $E^{3/2}$ into $E \times E^{1/2}$ and inserting for E the right hand side of the equation (4.4.3). This finally leads to

$$\triangle E = \frac{2\triangle t}{t} E. \qquad (4.9.4)$$

In the calculation care was taken of the fact, that for the crosssectional energy ranges the mathematical time resolutions were greater than the instrumental one. (40, 20 and 10 ns).

The calculated statistical deviations are presented as error bars graphically in the following chapter and listed together with the energy resolutions and the cross section values in appendix D.

4.10 Final Normalization

During analysis it was noted, that a systematic error had been accepted.

This error was a combination of two uncertainties: the uncertainty about the true mass, used in the target foils, and the uncertainty about the number of fission events, not recorded due to loss of fragments in the foils themselves.

a) uncertainty in target mass:
the determination of the target mass and its short-comings will be described in appendix C. In principle there are more accurate methods, but their employment was decided against, once it was discovered, that there was another source of systematic error, which could not be eliminated.

b) uncertainty in number of fragments lost:
this has been dealt with in subsection 4.7, in which an estimate of this number is described. Since this number can only be determined analytically, and since all available models have in common the same or similar uncertainties, this was a source for a systematic error, which could not be eradicated.

The presence of these two systematic errors led to the decision, to normalize the measured cross sections against a most recent available good absolute measurement of the fission cross section for U-235 and the ratio of the fission cross sections of U-238 to U-235 against other available data, to obtain absolute values. The normalization reference for the U-235 neutron fission

cross section was a measurement by G. S. Sidhu and J. B. Czirr[63]. This was the most recent measurement available with good statistics and resolutions. As a reference for the ratio of the neutron fission cross sections of U-238 to U-235 the evaluation of M. G. Sowerby et al.[19], was taken. From the ratio and the absolute fission cross section of U-235 the absolute fission cross section of U-238 was finally determined.

CHAPTER V

I. Presentation and Interpretation of the Data

5.1 Introduction

The first half of this final chapter will contain the final neutron fission cross sections for U-235 and U-238 as graphs, as measured and analyzed as part of this research project. The listing of the numerical values of the cross sections, the corresponding energies, the resolutions and statistical errors can be found in appendix D.

The interpretation of the cross section requires at first a look at the general shape. It will be shown, that related phenomena account for the very different shapes of both cross sections. Firstly, U-235 is discussed and then U-238, requiring a somewhat simpler interpretation. The U-235 data show some structure, and the significance of this at those particular energies is discussed. The first half of this chapter is then concluded by a comparison with the previous work of other authors.

5.2 Presentation of the Neutron Fission Cross Sections of U-235 and U-238 and Their Ratio

Pict. 47 shows the neutron fission cross section of U-235 in the energy range 0.3 - 12.5 MeV as a continuous graph. As has been pointed out in the previous chapter, the time resolutions are

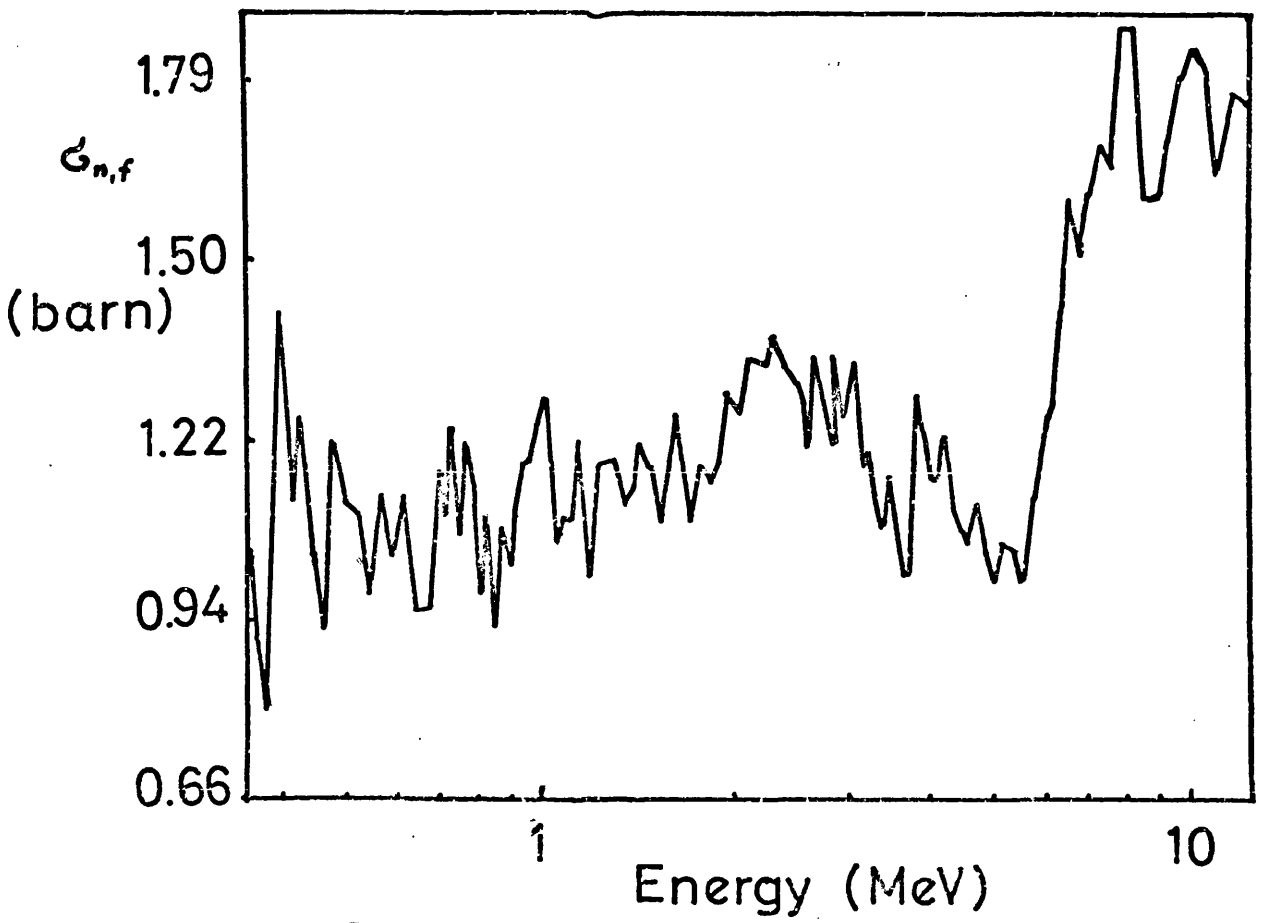

Pict. 47: Neutron Fission Cross Section of U-235

different in three regions: 0.3 - 0.7 MeV with 40 ns wide bins, 0.7 - 2.5 MeV with 20 ns wide bins and 2.5 - 12.5 MeV with 10 ns wide bins. Pict. 48 shows the same cross section as a succession of the measured individual energy points and shows the statistical errors and energy resolutions of every third point.

Pict. 49 presents the neutron fission cross section of U-238 in the energy range 0.7 - 12.5 MeV as a continuous graph. This is also divided into two separate time resolution regions: 0.7 - 2.5 MeV with 20 ns wide bins and 2.5 - 12.5 MeV in 10 ns wide bins. Pict. 50 gives the same cross section again as individual data points with every third one accompanied by error and resolution bars.

Finally, in pict. 51, the ratio of the neutron fission cross section of U-238 to the one of U-235 is presented. The range is between 0.7 - 12.5 MeV. Pict. 52 shows the same data as successive data points, every third one of which carries error and resolution bars.

5.3 Interpretation of the General Shape of the Cross Sections

Neutron fission cross sections of actinide nuclei can be basically divided into two groups, regarding their general shape: those which have a thermal fission threshold, and those, which have a threshold at some other fixed energy. In both cases this principal feature of the cross section is determined by pairing effects of the nucleons.

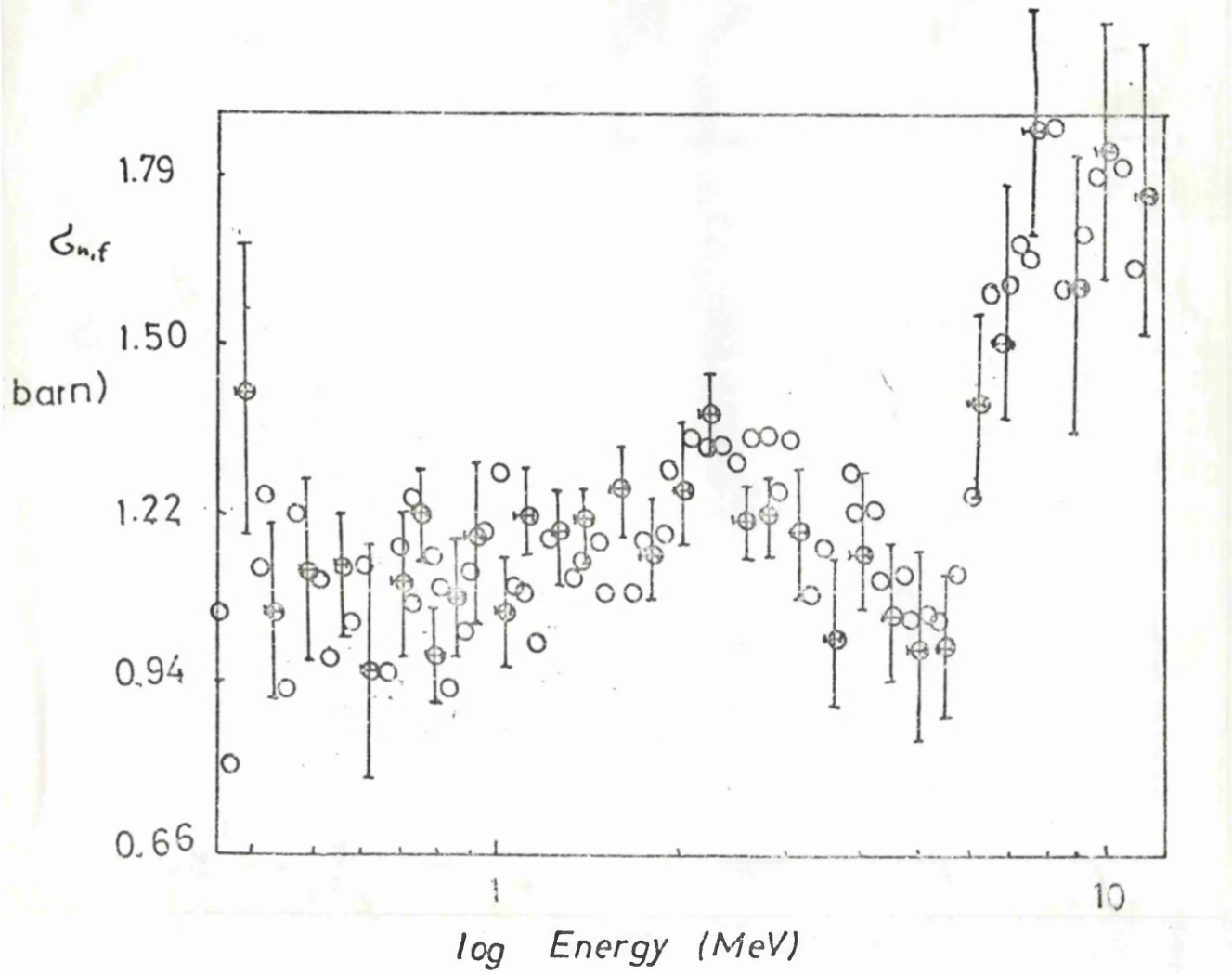

Pict.48: Neutron Fission Cross Section of U-235

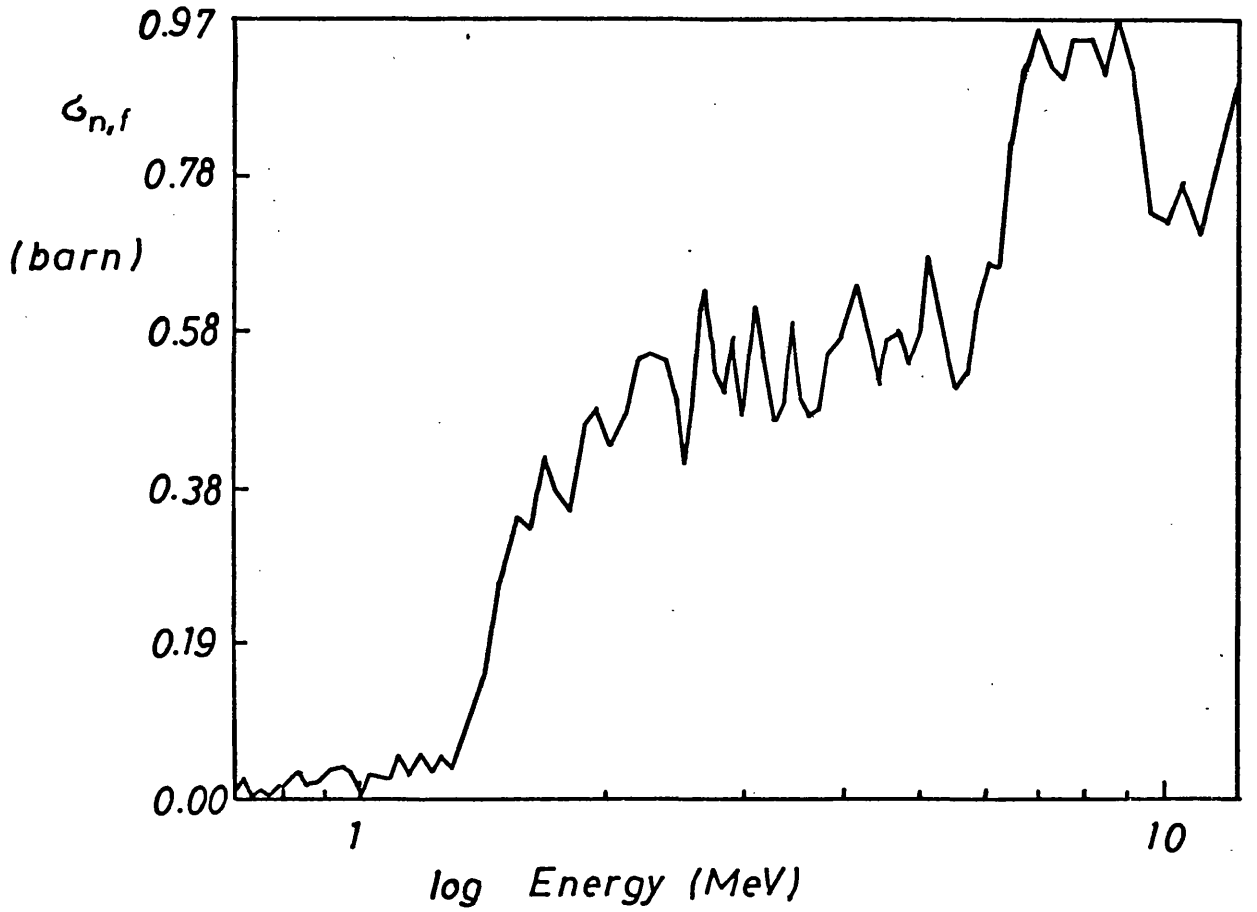

Pict.49: Neutron Fission Cross Section of U-238

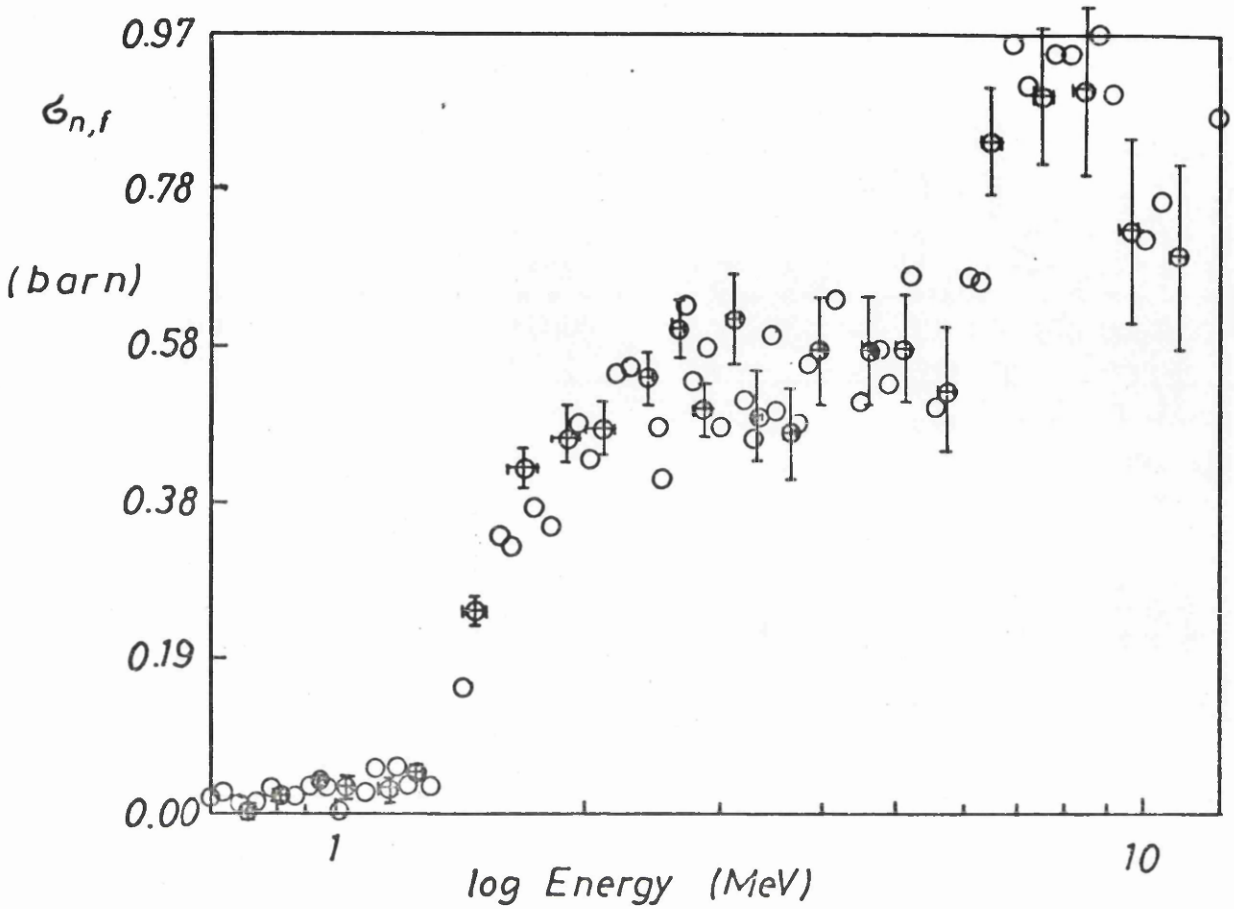

Pict.50: Neutron Fission Cross Section of U-238

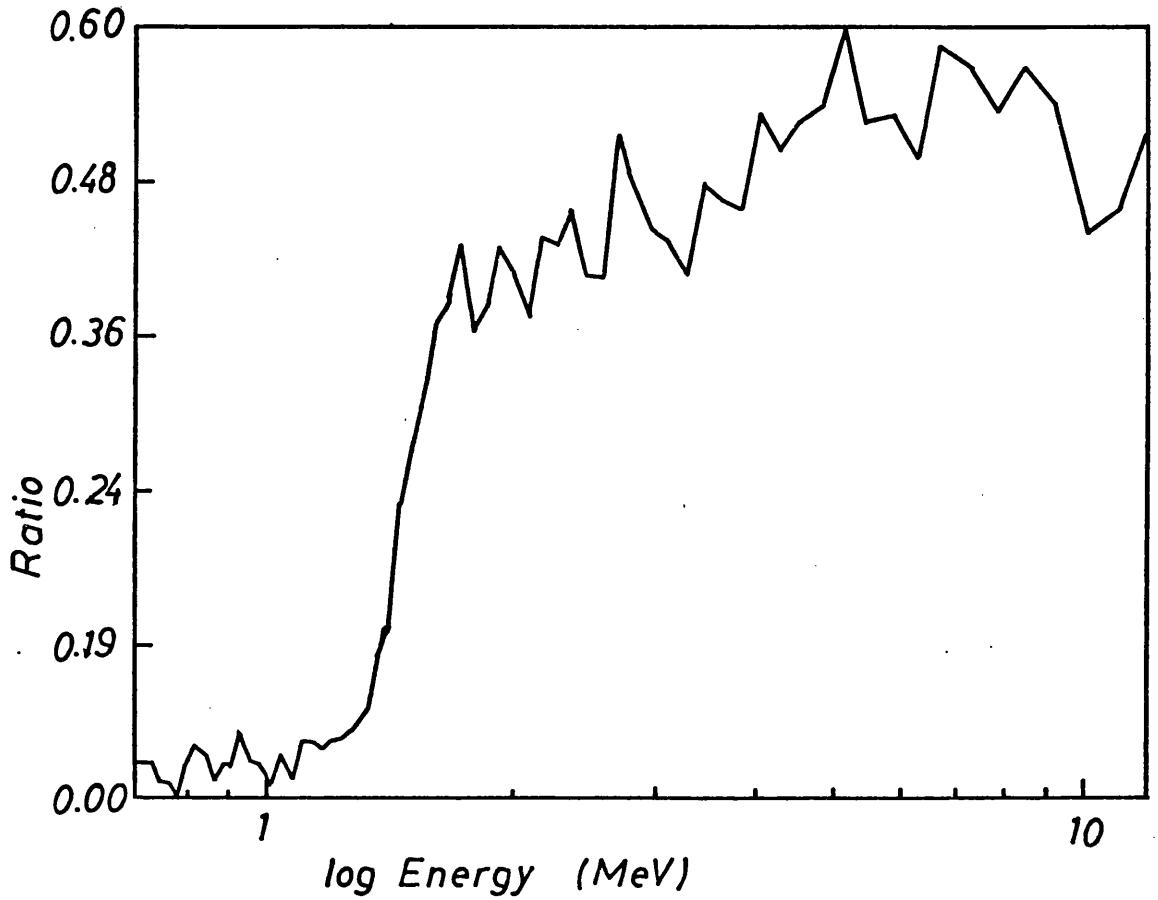

Pict.51: Ratio of the Neutron Fission Cross Sections of U-238/U-235

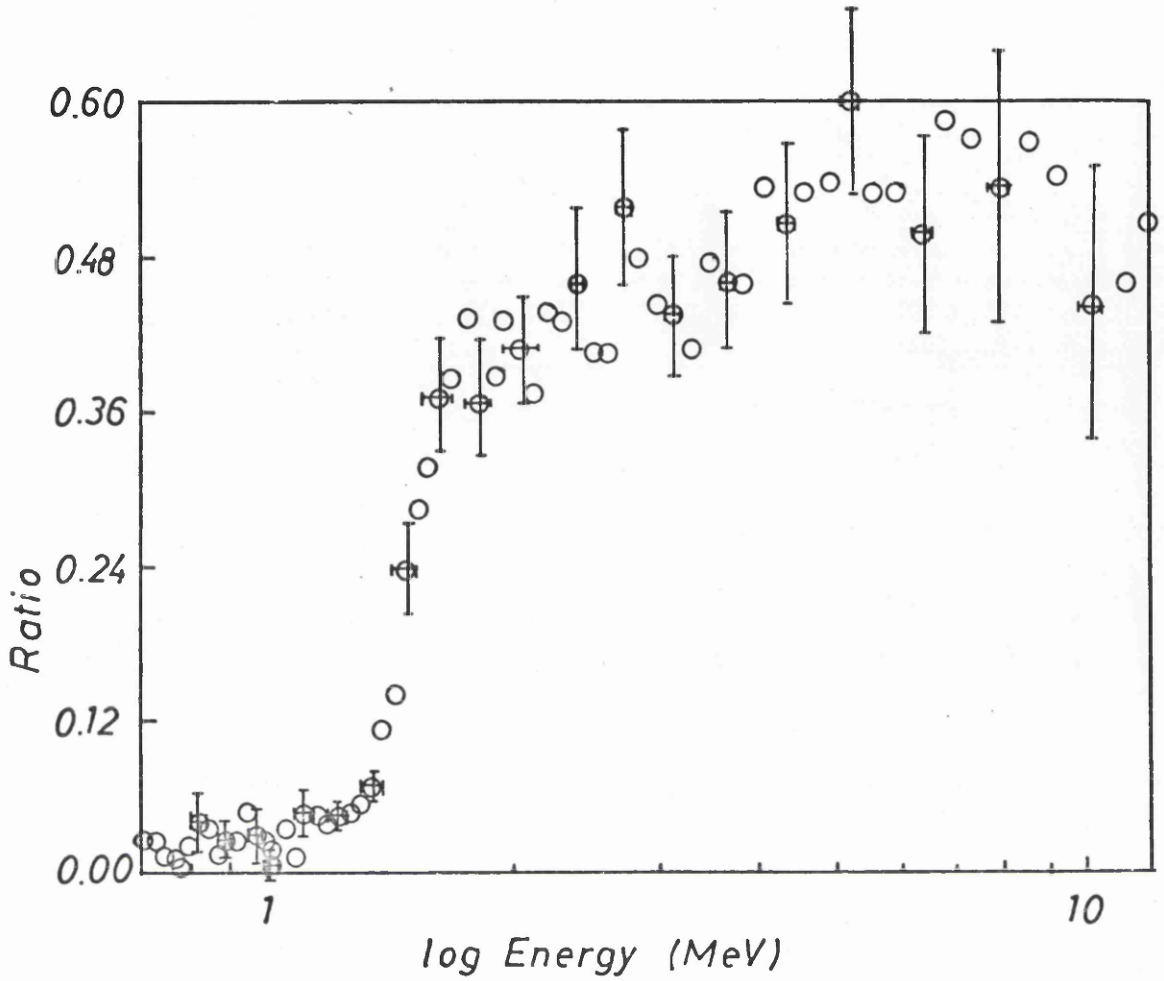

Pict.52: Ratio of the Neutron Fission Cross Section of U-238/U-235

5.31 U-235

U-235 has a thermal cross section, which means that, when a neutron is captured at thermal energy, i.e. when it is in equilibrium with its environment; the binding energy then released during the capture of this neutron, is sufficient to excite the nucleus, to surpass the fission threshold and split. Since U-235 is an odd-A nucleus, but has an even Z number, there is one neutron not bound in a subshell, paired either with a proton or with another neutron of opposite spin. It is only loosely attached to the nucleus. If on the other hand a single neutron enters the nucleus, this one and the unpaired one will form a strongly bound subshell, releasing the full binding energy of 6.536 MeV, well above both barriers, being at 5.63 MeV and 5.53 MeV resp. Therefore, even if the incoming neutron does not carry any more kinetic energy with it, the nucleus is excited enough to undergo fission.

The cross section then decreases as 1/v from thermal to higher energies, until it reaches about 0.65 MeV. From thereon it starts to rise again. As the theoretical calculations (equation (5.11.1)) in the second half of this chapter will show, this is due to a relative decrease in the probabilities of the competing reactions to fission, in particular neutron-capture- γ-ray-emission, which becomes negligible at these energies. After reaching an intermediate maximum at about 2.5 MeV, the cross section then

decreases again, following the 1/v-trend, which becomes again more dominant after being in equilibrium with the rising trend at the maximum.

At about 5 MeV the cross section rises fast to a maximum. This is due to an effect, called second try fission. Here the nucleus is still sufficiently excited, even after a previous decay via a competing channel, to split up, thus enchancing the chances of fission considerably. After reaching a peak at about 7 MeV, there is again a decrease of the cross section due to 1/v-behaviour.

5.3.2 U-238

U-238 is an even-A, even-Z nucleus with all nucleons paired in subshells and therefore with no thermal neutron fission cross section at all. If a thermal neutron enters the nucleus, it will be bound only very loosely, if at all. The energy release in this process,the binding energy of the additional neutron, is 4.86 MeV, well below both barriers of 6.46 and 6.16 MeV, so that this binding energy in itself is not sufficient to excite the compound nucleus above the fission threshold. It is therefore necessary, to supply a minimum of kinetic energy by the incoming neutron, to cause fission at all. This seems to be about 1.3 MeV. Below this energy the fission cross section is virtually zero, and it starts to rise rapidly above 1.3 MeV to a maximum value. Again, between 5 and 6 MeV the region of second try fission is approached, so that the cross section rises again very suddenly to a new maximum. From this it decreases in 1/v-fashion.

5.4 Interpretation of Possible Intermediate Structure in the U-235 Fission Cross Section

As mentioned in chapter I already, the important region to look for structure in support of the double-hump barrier, is the sub-threshold region or the region just below the second-try rise in the fission cross section. As will be explained presently, in the presence of a secondary potential well the cross section should show some structure as distinct from that related to the first potential well [8]. In any case, the cross section should cease to be a smoothly varying function with energy due to overlapping vibrational resonances of one single potential well. It should also show a distinct vibrational band associated with the second potential well.

The results in pict. 48 suggest the existence of a broad resonance between 3.5 and 5.0 MeV of an observed width of 1.5 MeV which is a strong candidate for such a band. The strength of the peak above the slowly decreasing trend of the cross section is about 0.25 barn and therefore well above the statistical uncertainty of 0.105 barn at the height of the peak. To explain this variation from the 1/v-behavour of the cross section with competing reactions of other natures is not possible. It must therefore be concluded, that such intermediate structure would be further evidence for the existence of a double-hump-fission-barrier of the compound nucleus U-236.

The sudden rise of the cross section at about 3.5 MeV could then be explained by the fact, that the second potential well is assumed to be lower than the primary one. This enhances the possibility of second-try-fission at an earlier stage than for a reaction, which

involves the main or both potential wells. Similar structure has been observed for example for the compound nucleus Th-231 [64,65,66] in the subthreshold region. A direct comparison with this isotope, however, is not possible, since Th-230 has a relatively high fission threshold (1.14 MeV) and no thermal cross section. Therefore, its subthreshold region can be investigated, whereas in the case of U-235 the second-try-fission-region has to be studied. In both cases, however, the observed vibrational bands are related to the same phenomenon.

5.5 Comparison With Previous Measurements

As already said in chapter I, a variety of measurements of these two cross sections had been performed at earlier stages by different authors. It would exceed the scope of this thesis to discuss all or even most of them in connection with the presented ones. However, it can be said that both the U-235 and U-238 neutron fission cross sections as measured, and therefore of course also their ratio, are in excellent agreement with past published work, regarding their principal features.

To compare individual data with the presented ones, it seemed most useful to choose an evaluation, including a selection of the best past experiments for the absolute values of σ (n,f) of U-235 and U-238 and the most recent available experimental data for the absolute value of σ (n,f) of U-235 and the ratio of σ (n,f) of U-238 to U-235. The evaluation is the one by M. G. Sowerby et al.[19], and the newly measured data are by G. S. Sidhu and J. B. Czirr[63] and J. W. Behrens et al.[67] respectively. These data are presented in comparative graphs with the measured ones of this research project in pict. 53,54,55.

Comparing the U-235 data with the evaluation shows that there is a difference in the depth of the valley in the cross section between 0.3 and 2.0 MeV. The difference is about 0.3 barns at the deepest point of the valley, the newly measured data being lower. All other significant points, however, agree very well: the intermediate maximum at about 2.0MeV, the depth of the valley in the sub-second-try-fission region and the second-try maximum at about 8 MeV. There is also no structure between 3.5 and 5 MeV present in the evaluation, as observed in this measurement. It must also be said, that the evaluation in the region 0.3 - 12.5 MeV is based on only few data points.

A comparison of the U-235 cross section with the experimental one by G. S. Sidhu and J. B. Czirr[63] reveals no significant difference,

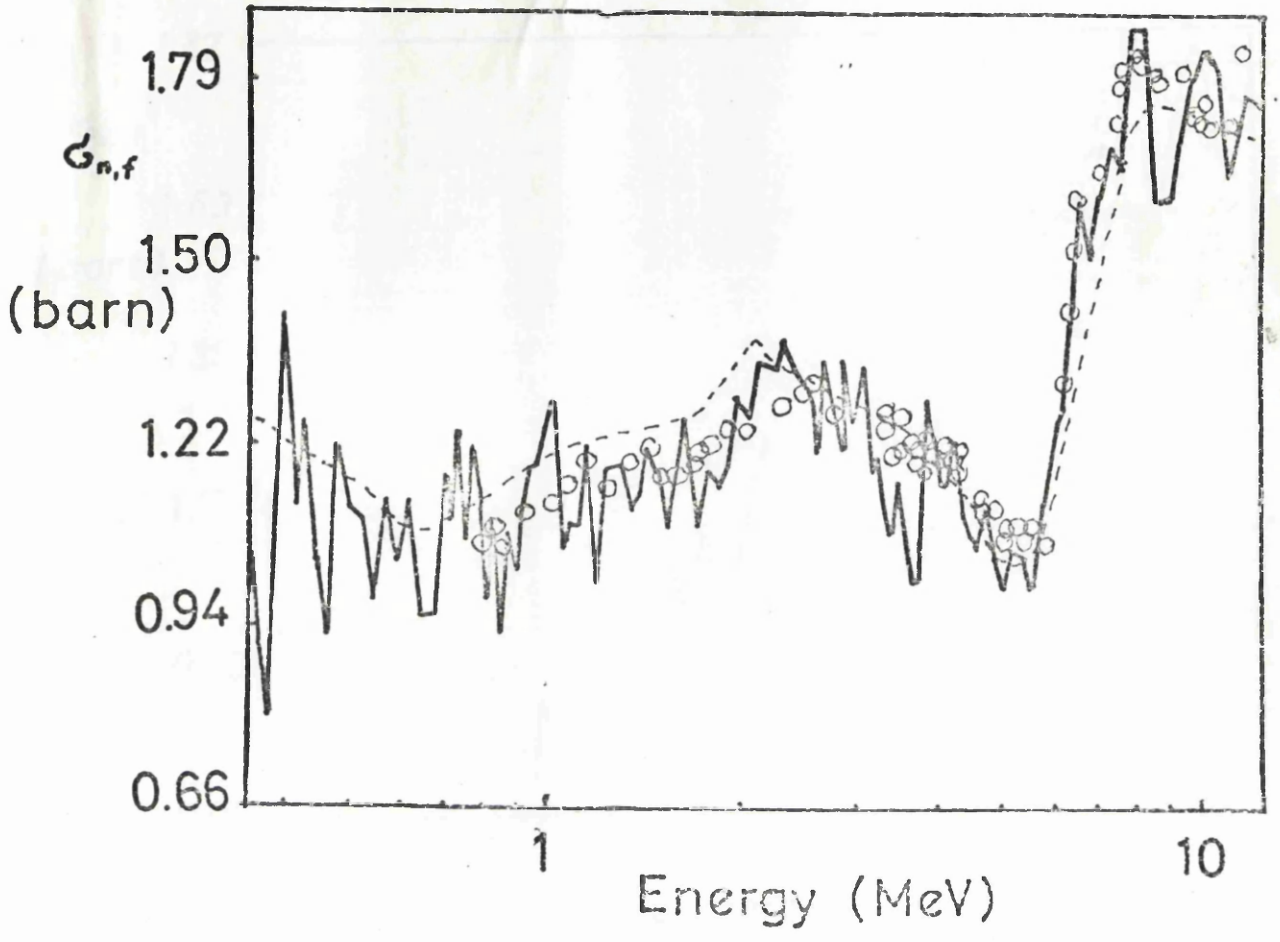

Pict.53: Comparison of the U-235 Fission Cross Section With Other Data

——— *Present Experiment*

– – – – *Evaluation By M. G. Sowerby et al.*

o *Experiment By G. S. Sidhu and J. B. Czirr*

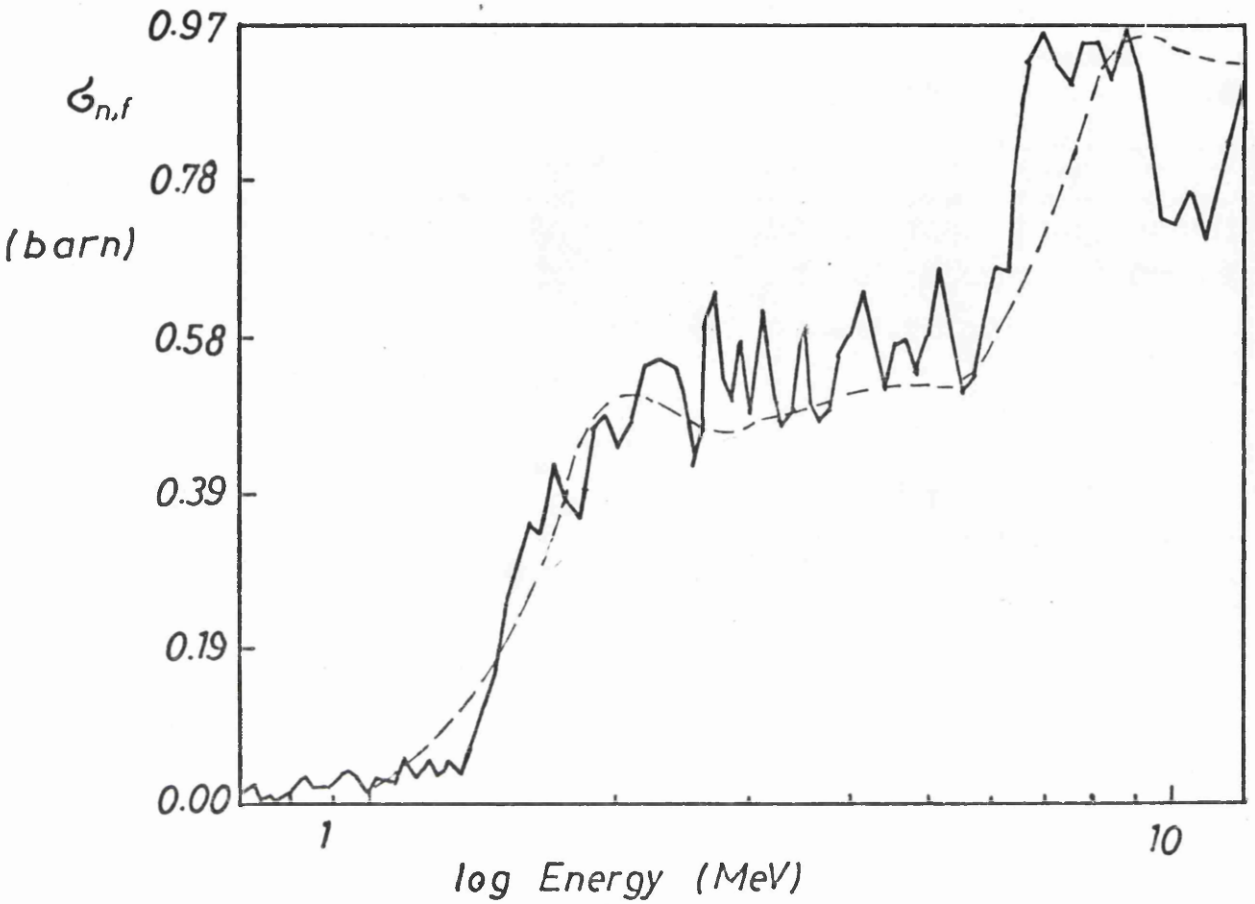

Pict.54: Comparison of the U-238 Neutron Fission Cross Section With Other Data

——— *Present Experiment*

– – – *Evaluation By M. G. Sowerby et al.*

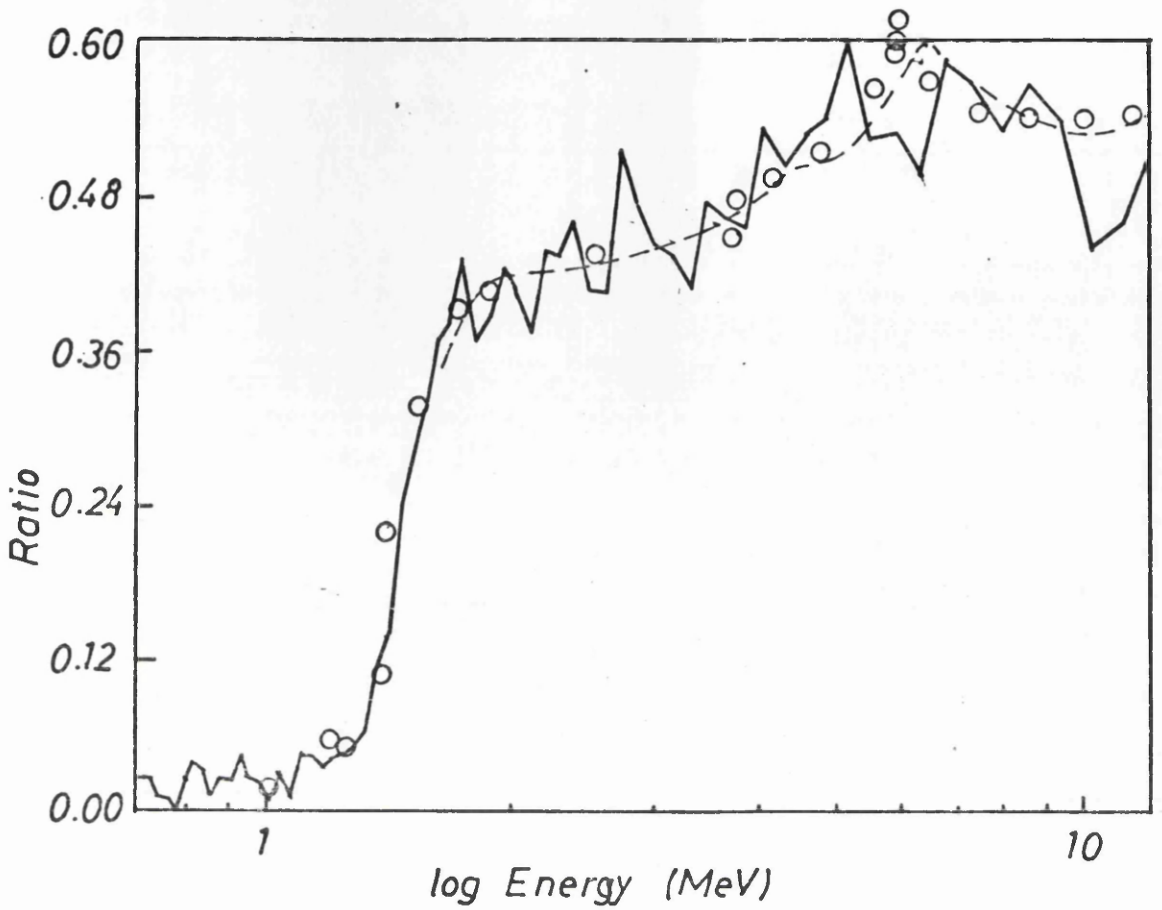

Pict.55: Comparison of the U-238/U-235 Neutron Fission Cross Section Ratio With Other Data

——— Present Experiment

– – – Evaluation By M.G. Sowerby et al.

o Experiment By J.W. Behrens et al.

As in the evaluation all maxima and minima are consistent with the present data. There is even a weak indication of intermediate structure in the sub-second-try-region as observed in the present measurement. The energy range in the experimental comparison data does, however, not extend below 0.7 MeV. The present data show excellent agreement with the evaluation and the other experiment at all significant points.

The evaluation of the U-238 data is also only based on a few data points. On the other hand, the present data are of greater statistical uncertainty than the ones for U-235. It is therefore not possible to interpret the variations in this cross section as genuine structure. The statistics get worse at higher energies particularly above 10 MeV, where there is a drop in the cross section. Apart from the general shape the fission threshold, as it appears when the cross section increases at a certain energy, is also in agreement at 1.3 MeV.

Much the same that has been said for the U-238 data can be said when comparing the ratio with evaluated and measured data. Below the fission threshold of U-238 the value is insignificant. In the present data the statistics are dominated by the one of the U-238 measurement. The evaluation, again based on not many points, shows a more smooth behaviour than both the present data and the measurement by J. W. Behrens et al.[67]. Both experimental

data, however, agree excellently, particularly at the intermediate peak at about 6 MeV.

Concluding it can be said, that previously observed features have been confirmed, and that some new light is thrown on the region 0.3 - 2.0 MeV. The observed structure is more clearly seen than the weak indications of the same in a most recent measurement, whereas it is missing in other previous data.

II. Theoretical Calculations

5.6 Introduction

The theoretical calculations of the neutron fission cross sections for U-235 and U-238 were carried out, according to the statistical model discussed in Chapter I, and the main part of these calculations are only valid between 1 and 5 MeV. The lower limit is determined by the fact, that below 1 MeV details of individual levels of the compound nucleus in question have to be known from experiments, whereas above this value level density distributions can be employed. The upper limit is determined by the fact, that the calculations do not provide for second-try-fission effects.

As main parameters the fission transmission coefficients were calculated, based on tunnel effect theory. Then for the least important competing channel, the neutron-capture-γ-ray-emission, transmission coefficients were calculated according to the giant resonance model. The main competing reactions are elastic and inelastic scattering, for which the total transmission coefficients were determined, using the compound nucleus formation probabilities. For the calculation of the incoming wave transmission coefficients a separate procedure was adopted, based on an optical model calculation by J. D. Kellie [68]. For the final calculation of the cross sections the two separate fission transmission coefficients, representing the two barriers, had to be combined in a suitable way. The theoretical data are then presented and discussed in comparison with the experimental results.

5.7 The Fission Transmission Coefficients

For the explanation of α-decay the theory of tunnel effect has been developed by Gamow. In this it is postulated that particles may pass through a potential barrier, even when their energy states are not high enough, to pass over it. This is explained in optical terms by assigning optical qualities to the barrier, such as reflection and transmission. Therefore a transmission probability of a certain particle at a certain state through a barrier can be determined.
N. Bohr and J. A. Wheeler[3] have proposed an adaptation of this theory to nuclear fission to determine a fission transmission coefficient through a potential barrier. For a single channel this coefficient becomes:

$$T_{(f)} = \frac{1}{1+\exp\left[-\frac{2\pi(E-E_f)}{\hbar\omega_f}\right]} , \qquad (5.7.1)$$

where E_f is the height of the barrer, and $\hbar\omega_f$ describes the shape characteristic of this barrier. To determine the total transmission coefficient for all possible channels, one has to integrate over all individual channels, leading to

$$T_{J\pi(F)}(E) = \int_0^\infty d\varepsilon \rho^{(F)}(\varepsilon, J^\pi) \frac{1}{1+\exp\left[-\frac{2\pi(E-V_F-\varepsilon)}{\hbar\omega_F}\right]} , \qquad (5.7.2)$$

where $T_{J^\pi\,(F)}(E)$ is the total fission transmission coefficient for this particular barrier at channel spin J and parity π as a function of excitation energy, $\rho^{(F)}(\varepsilon, J^\pi)$ the level density distribution with

respect to fission states and V_F the peak barrier deformation energy. This distribution can be expressed as

$$\rho_F(E, J^\pi) = (2J+1) e^{-(J+1/2)^2/2\sigma^2} \times C_F e^{E/\Theta_F} \quad (5.7.3)$$

with σ called a spin dispersion coefficient, C_F is a constant and Θ_F a temperature factor. σ, C_F and Θ_F are all energy dependent and can be obtained from data tables, which summarise experimental measurements and liquid drop calculations. V_F, ω_F can also be obtained in this way. In this way the fission transmission coefficients for U-236 and U-239 for two barriers have been calculated. The results are presented in pict. 56.

5.8 The Neutron-Capture-γ-Ray-Emission Transmission Coefficients

The transmission coefficient for the emission of a single γ-ray of energy ε_γ from excitation E can be described as

$$T_{J\pi(\gamma)}(E) = \frac{2\pi \overline{\Gamma_{J\pi(\gamma)}}}{D_{J\pi}} = 2\pi f(E, \varepsilon_\gamma) \quad (5.8.1)$$

in dependence of J and π, where Γ and D are as usual and f (E, ε_γ) is called the spectral factor, containing information about the energy dependence of the transition on the structure of the giant resonance. The total radiative transmission coefficient can finally be written as

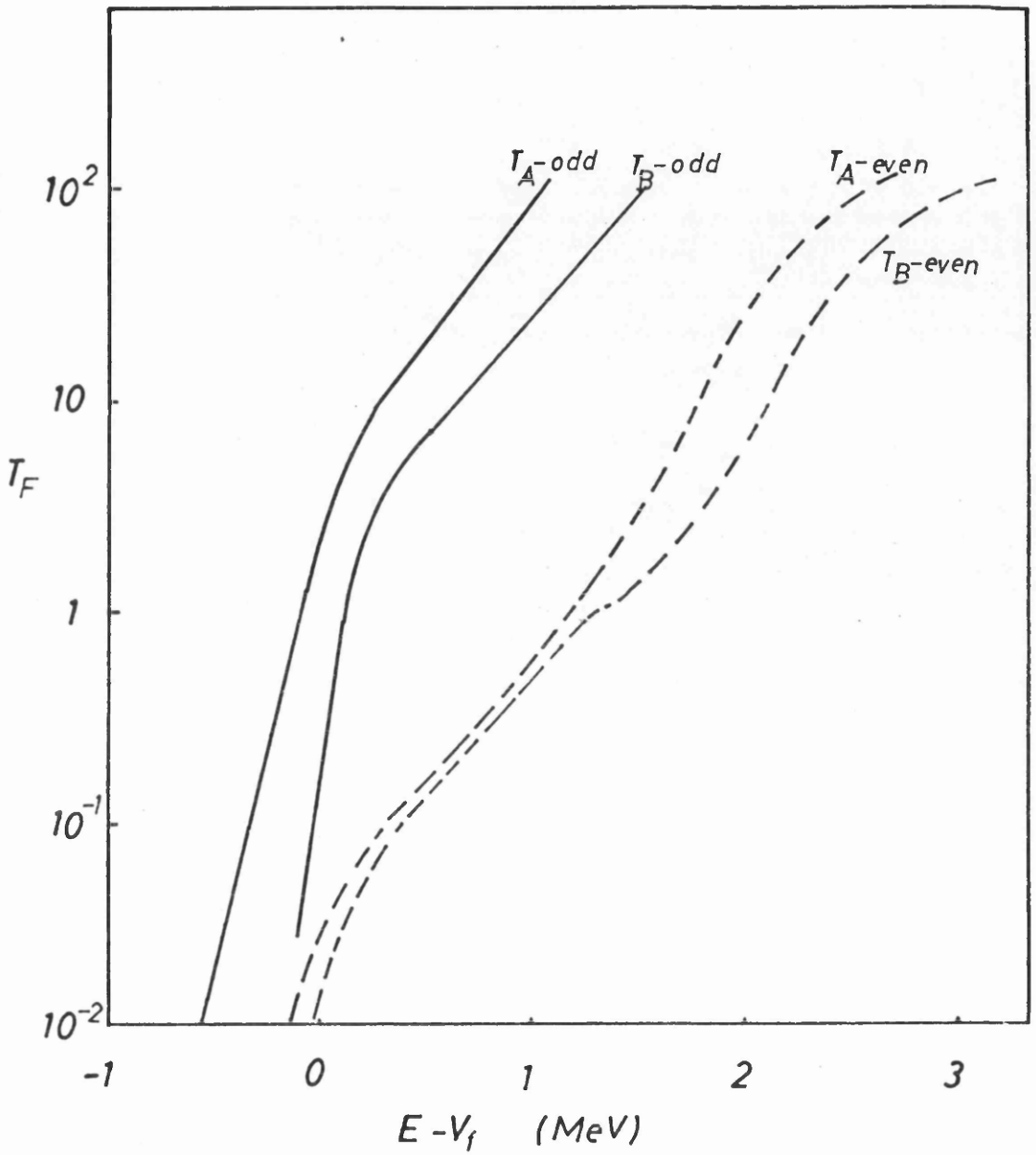

Pict.56: Neutron Fission Transmission Coefficients

$$T_{J^\pi(\gamma,tot)}(E)=\int_0^{E} d\varepsilon_\gamma\, f(E,\varepsilon_\gamma)\sum_{J_f=|J-1|}^{J+1}\rho^{(c)}(E-\varepsilon_\gamma,J_f)\,, \tag{5.8.2}$$

where $\rho^{(c)}$ is the level density distribution of the compound nucleus again and can be expressed as

$$\rho(J^\pi)=(2J+1)e^{-(J+1/2)^2/2\sigma^2}\times Ce^{E/\Theta}\,, \tag{5.8.3}$$

with σ, C and Θ again energy dependent. To establish the spectral factor, two models are available, the Weisskopf Strong Coupling Dipole Model and the Giant Resonance Model, the latter of which has been adopted here. It is based on the giant resonance in photonuclear absorption. Here f is

$$f(E,\varepsilon_\gamma)=\frac{8}{3}\frac{NZ}{A}\frac{e^2}{\hbar c}\frac{1.4}{mc^2}\sum_{i=1}^{2}\left(\frac{1}{3}\right)\frac{\Gamma_{iG}\,\varepsilon_\gamma^4}{(\varepsilon_\gamma^2-E_{iG}^2)+(\Gamma_{iG}\varepsilon_\gamma)^2} \tag{5.8.4}$$

where

$$E_{1G} = 11\ \text{MeV},\quad \Gamma_{1G} = 2.9\ \text{MeV} \tag{5.8.4.1}$$

$$E_{2G} = 14\ \text{MeV},\quad \Gamma_{2G} = 4.5\ \text{MeV} \tag{5.8.4.2}$$

denoting the parameters of the two dipole components. In the calculation of these transmission coefficients it was shown that their contribution was small, decreasing in importance, when going from 1 MeV up to higher energies, with respect to the other transmission coefficients.

5.9 The Total Scattering Transmission Coefficients

These have been calculated to include both elastic and inelastic scattering, and are based on the compound nucleus formation cross section in the optical model:

$$\sigma_{n,CN}(\varepsilon) = \pi\lambda^2 \sum_{l=0}^{\infty} (2l+1) T_{(l)}(\varepsilon) \quad , \tag{5.9.1}$$

where ε is the neutron energy, λ is the de Broglie-wavelength of the incoming neutron and $T_{(l)}(\varepsilon)$ is the incoming wave transmission coefficient as a function of the neutron orbital angular momentum l and its energy ε . The total scattering transmission coefficient can then be written as

$$T_{J^\pi(n,tot)} = (2J+1) \int_0^{E-S_n} d\varepsilon \, \rho_{eff}^{(R)}(E-S_n-\varepsilon) \sum_{l=0}^{\infty} (2l+1) T_{(l)}(\varepsilon) \tag{5.9.2}$$

where S_n is the neutron separation energy of the compound nucleus and $\rho_{eff}^{(R)}$ is again a level density distribution

$$\rho_{eff}^{(R)}(E) = C_R e^{E/\Theta_R} \tag{5.9.3}$$

with C_R and Θ_R as usual, taking the effective angular momentum as being zero.

The calculation of these transmission coefficients requires the knowledge of $T_{(1)}(\varepsilon)$ which were required also for the final cross section calculation. How this was done, is described in the following subsection.

5.10 The Incoming Wave Transmission Coefficients

Whereas the previous transmission coefficients are all based on the publication by J. E. Lynn[9], the calculation of the incoming wave transmission coefficients is based on a programme, called THEO, by J. D. Kellie[68]. Here the optical model is used, to calculate the total cross section of the target nucleus, from which the transmission coefficients can be deduced. In chapter I the transmission coefficient was defined as

$$T_l = 1 - |\eta_l|^2 \quad , \tag{5.10.1}$$

where η_l is called the reflection coefficient, and the total cross section as

$$\sigma_{tot} = \frac{2\pi}{k^2} \sum_l (2l+1)(1 - Re\,\eta_l) \tag{5.10.2}$$

in optical model terms. Therefore, from knowing σ_{tot} as a function of

1, then η_1 and hence T_1 can be obtained. It has also been shown already, how σ_{tot} depends on the total scattering amplitude in general. To produce particular calculations for this amplitude and associated optical model parameters, it is neccessary to start with a distinct optical potential. This has been done in the past by various authors [69,70], on which THEO is based. These authors propose a potential

$$V(r)=V_C(r)+V_N(r)+V_S(r) \tag{5.10.3}$$

where $V_c(r)$ is the Coulomb, $V_N(r)$ the nuclear and $V_S(r)$ is the spin-orbit part. Both $V_N(r)$ and $V_S(r)$ are composed out of real and imaginary parts, where the real part determines scattering processes and the imaginary part acounts for absorption. The insertion of this combined potential into the Schroedinger equation and its successive solution, as outlined in chapter I, leads to the determination of the scattering amplitudes and associated optical model parameters. From there the total cross section is calculated, and the incoming wave transmission coefficients from it.

5.11 Final Theoretical Calculation and Presentation of Results

The formula, to combine the transmission coefficients, to calculate the fission cross sections of U-235 and U-238, has also been presented earlier in a more general form, which leads to the particular one

$$\sigma_{n,f}(\varepsilon)=\pi\lambda^2\sum_l T_l \chi \sum_J \frac{g(J,I)T_{J\pi(F)}(\varepsilon)}{T_{J\pi(F)}(\varepsilon)+T_{J\pi(\gamma)}(\varepsilon)+T_{J\pi(n,tot)}(\varepsilon)}\,. \tag{5.11.1}$$

where

$$g(J,I)=\frac{2J+1}{2(2I+1)} \qquad (5.11.2)$$

is called the statistical weighing factor[71], with

$$J=I\pm 1/2\,. \qquad (5.11.2.1)$$

The important thing in this calculation was the way of combining the two fission transmission coefficients for the two individual barriers into a common one. It can be shown, that

$$T_{(eff,F)}=\frac{T_{(A)}T_{(B)}}{T_{(A)}+T_{(B)}} \qquad (5.11.3)$$

with $T_{(A)}$ and $T_{(B)}$ the individual and $T_{(eff,F)}$ the combined fission transmission coefficient. This is, however, only true, if either $T_{(A)}$ or $T_{(B)}$ or both are close to or above unity. If one of them is considerably less, the fission probability

$$P_F=\frac{T_{(F)}}{\sum T_{(c)}} \qquad (5.11.4)$$

has to be calculated in a different way:

$$\overline{P}_F=\left[1+\left(\frac{\sum_{c'}T_{(c')}}{T_F}\right)^2+2\left(\frac{\sum_{c'}T_{(c')}}{T_F}\right)\coth\left[\tfrac{1}{2}\left(T_{(A)}+T_{(B)}\right)\right]\right]^{-1/2}, \qquad (5.11.5)$$

where c' refers to channels other than fission. This condition was respected and the theoretical neutron fission cross sections for U-235 and U-238 calculated between 1 and 5 MeV. The results are

presented in pict. 57 and 58.

5.12 Comparison With Experimental Results and Conclusions

Pict. 59 and 60 show comparative graphs of the theoretical and experimental data of U-235 and U-238 between 1 and 5 MeV. Two features can be seen immediately: firstly, the general shape of the theoretical calculations agrees excellently with the experimental one. Both follow the same rise and fall pattern of the measured data. For U-235 the theoretical cross section peaks at exactly the same energy as the experimental one, and for U-238 the rise above the fission threshold in the calculated data follows the experimental one almost in line. The other point that can be observed, is that both theoretical curves are higher than the experimental curve by 30 % to 50 %.

A closer investigation of the individual contributing factors reveals that the neutron-capture-γ-ray-emission transmission coefficient plays not such a dominant part, as to account for this shift, and that the fission transmission coefficients were in excellent agreement with other authors[9]. The remaining uncertainties were therefore due to the incoming wave transmission coefficients, from which the total scattering transmission coefficients were also calculated. Pict. 61 shows a comparison of the experimental with the theoretical total cross section of U-238[72], from the latter one of which the incoming wave transmission coefficients were derived. It is obvious, that the agreement is not very good. To improve the theoretical cross section, therefore, it is

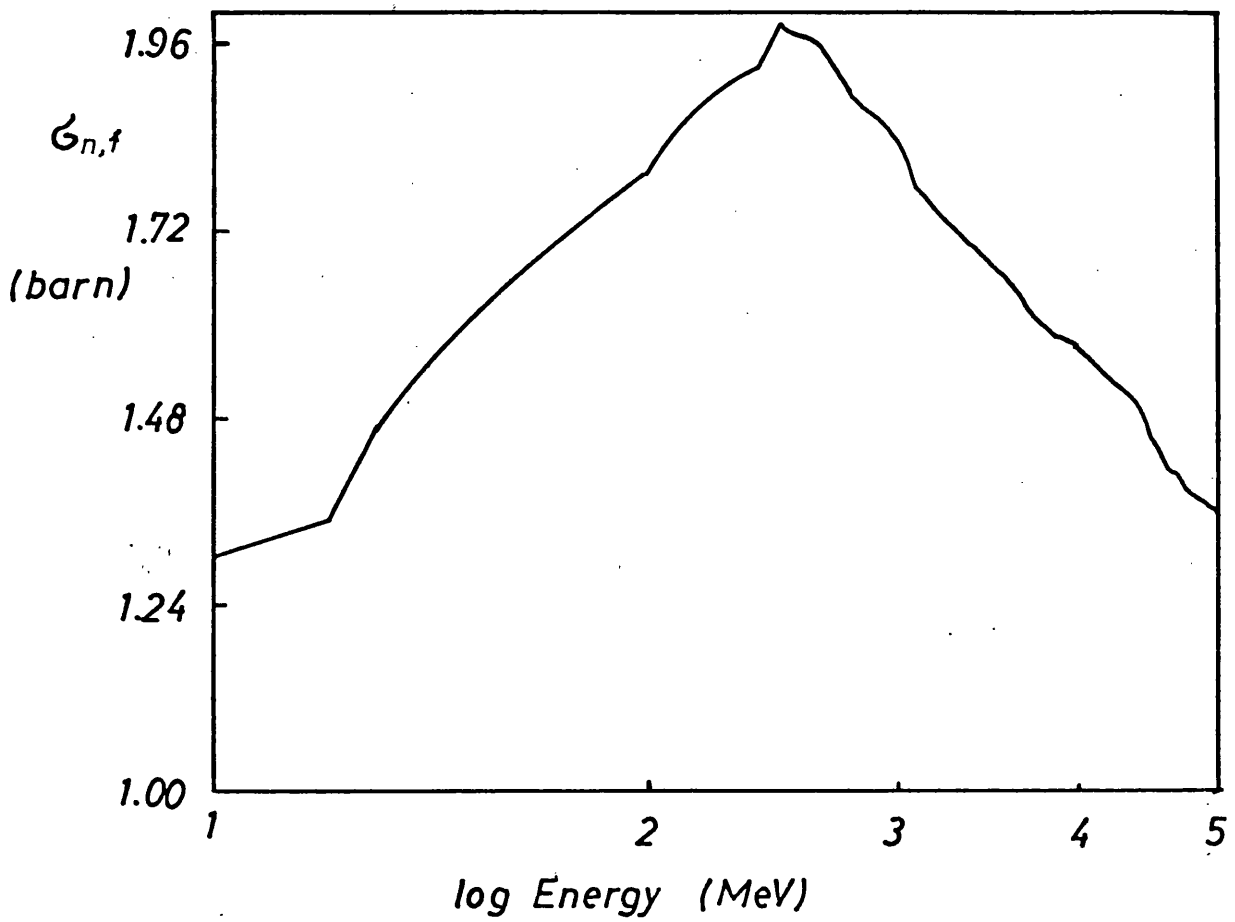

Pict.57: Theoretical Neutron Fission Cross Section of U-235

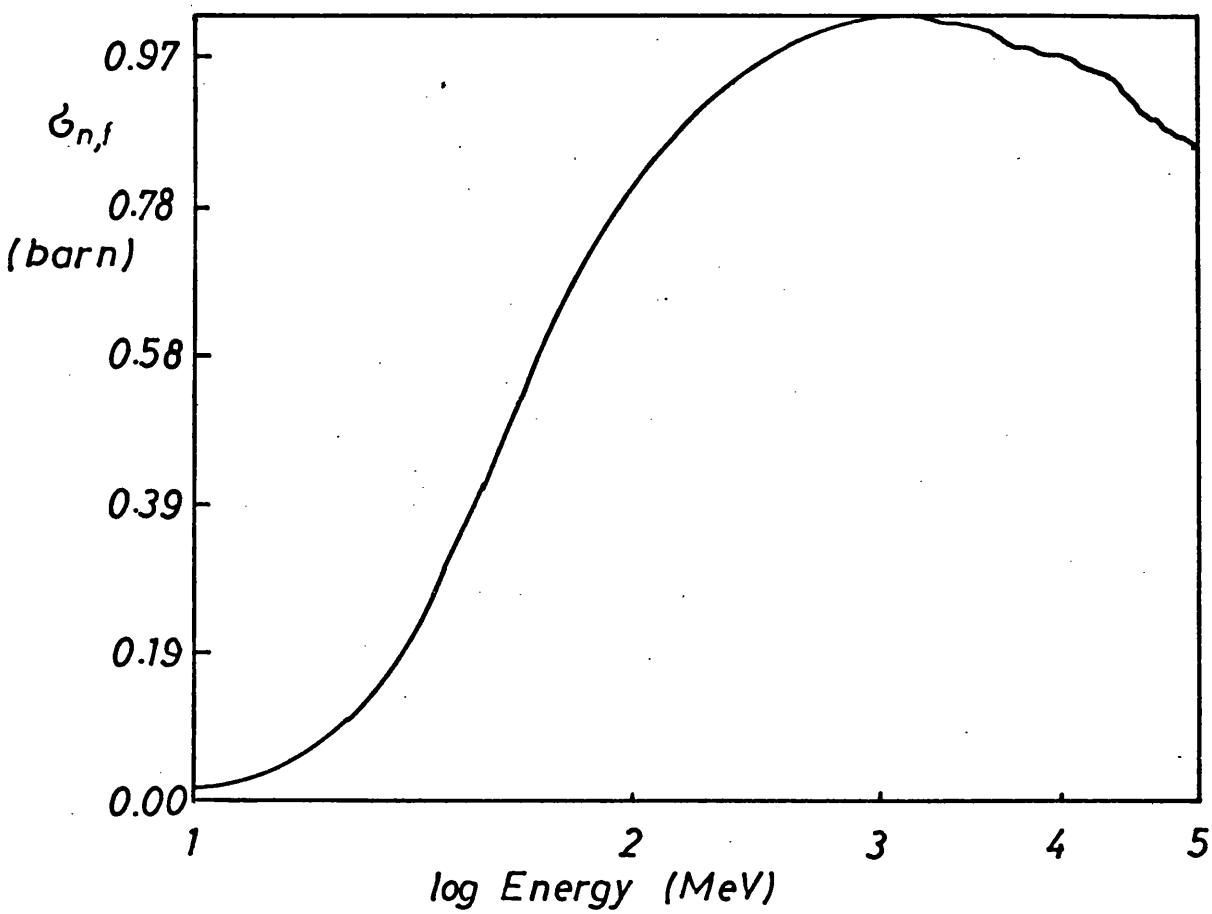

Pict.58: Theoretical Neutron Fission Cross Section of U-238

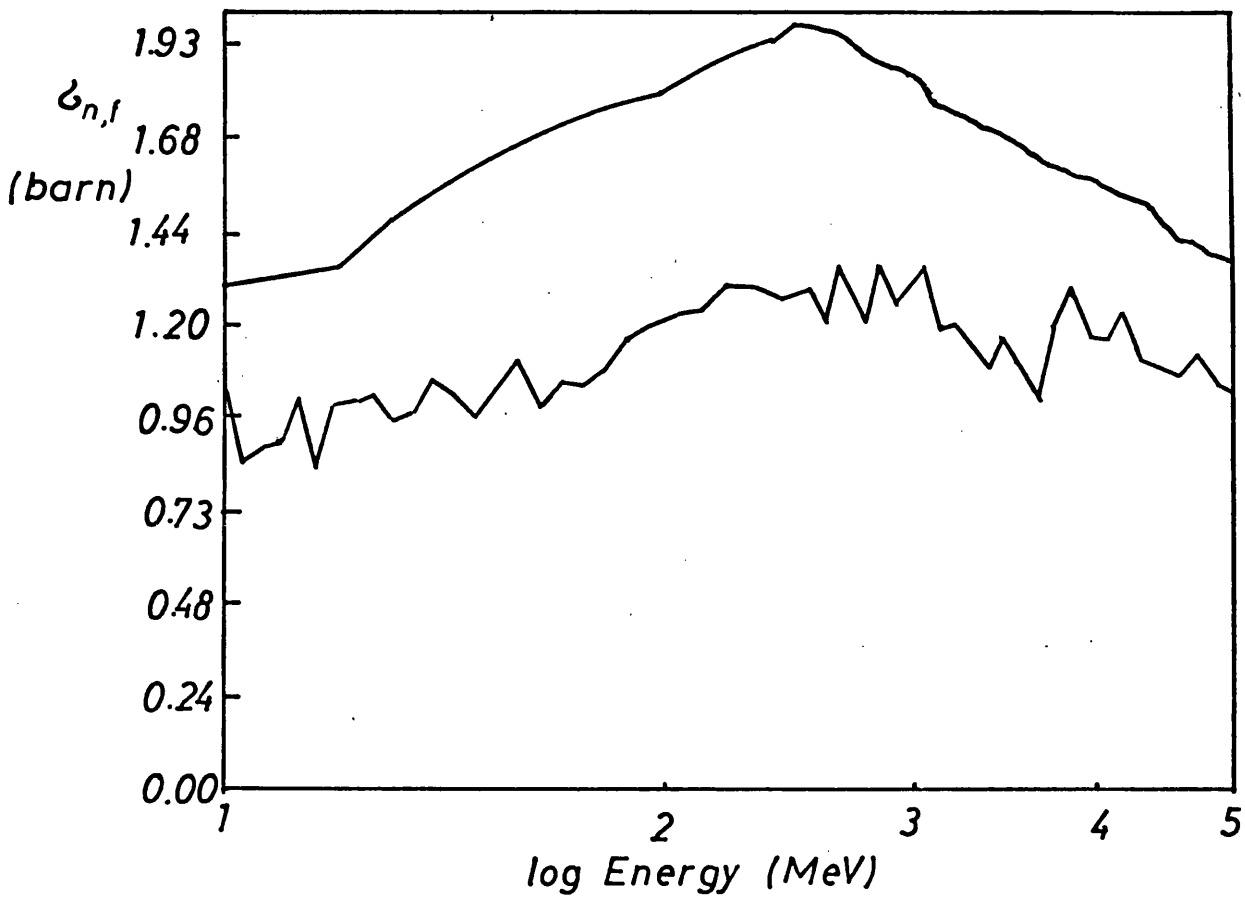

Pict.59: Comparison of Theoretical and Experimental Neutron Fission Cross Section of U-235

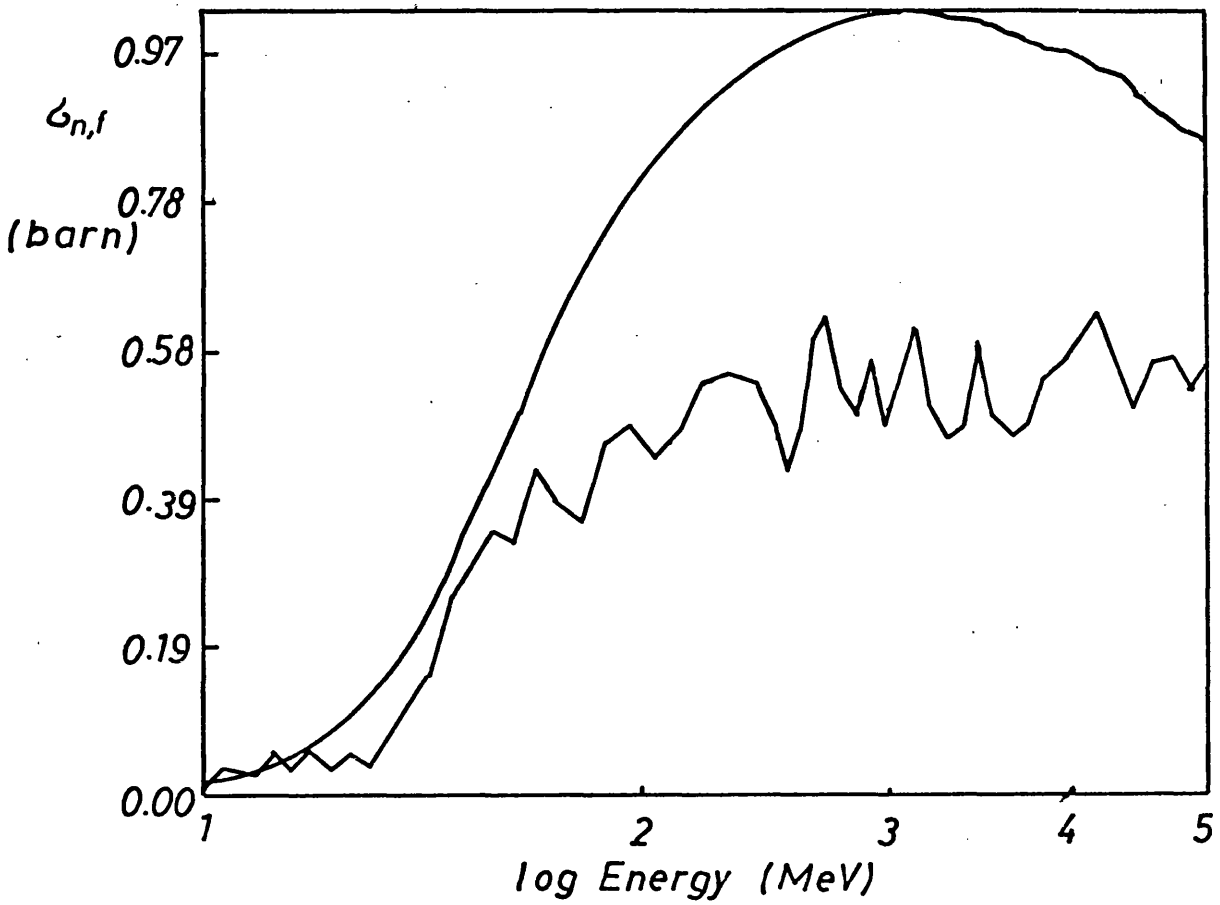

Pict.60: Comparison of Theoretical and Experimental Neutron Fission Cross Section of U-238

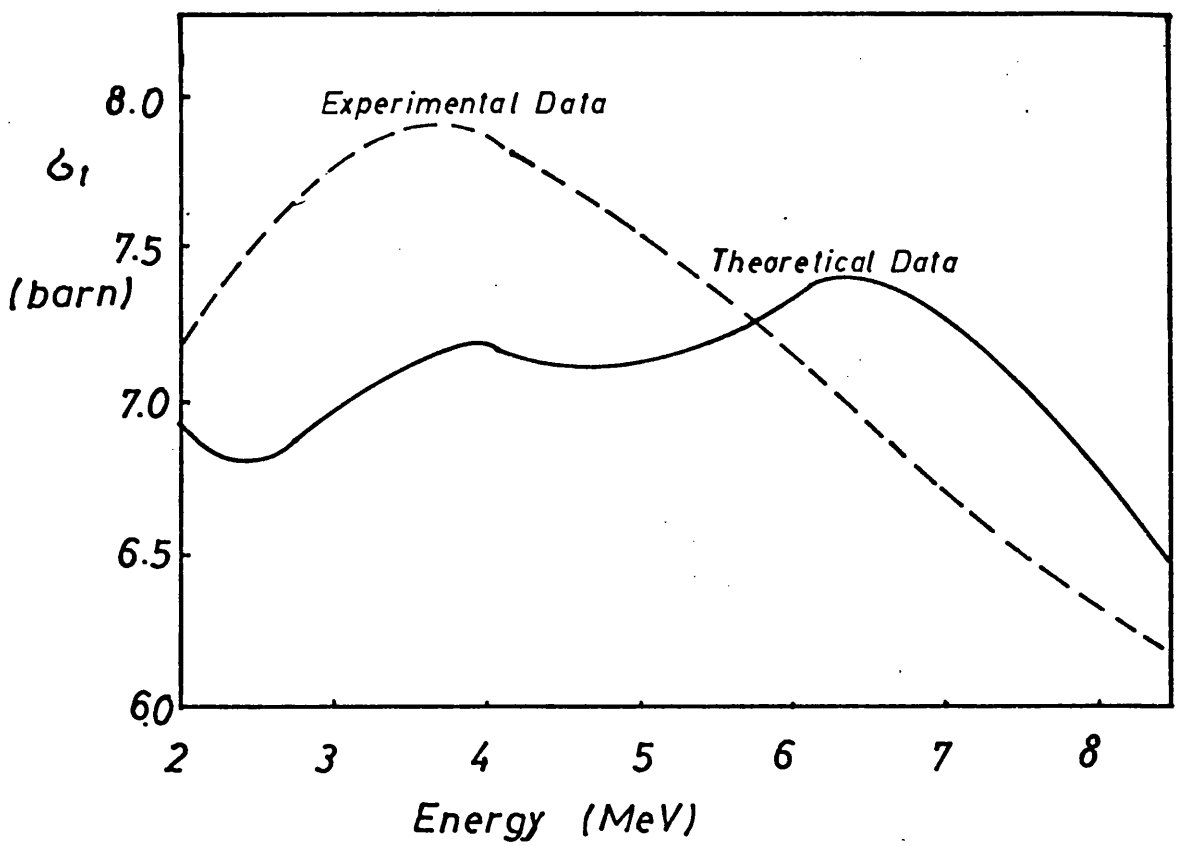

Pict.61: Total Neutron Cross Section of U-238[72]

neccessary to use a model for calculating the total cross section, which is more successful in this energy region. This would be a problem for future theoretical investigations.

The main limit on the experiment itself was the relatively low count rate, concerning fission events in the gas scintillator. This not only presented difficulties to achieve optimum statistics, but limited the range of possibilities in these experiments even further. The bi-dimensional mode of data taking would have been ideal, to allow an investigation of the dependence of fragment mass distribution on the energy of the fission inducing neutron. In this way it could have been clarified, whether there are preferential regions in the cross section, which might be associated with either symmetrical or asymmetrical fission, especially in connection with structure, associated to one or the other potential well. To identify this structure more positively, an additional measurement of the angular distribution of the fission fragments would have been neccessary. Finally, much better statistics should provide a split-up of the vibrational structure between 3.5 and 5.0 MeV into narrow rotational resonances as has been attempted in experiments with other isotopes [64,65,66].

There are basically two solutions to the count rate problem. One possibility is, to increase the target mass by designing a gas scintillator which incorporates more than one single target foil. The second possibility is to use an accelerator with a much higher

beam current, to produce more neutrons in the bremsstrahlung target. Such a machine is currently under construction in the Kelvin Laboratory.

APPENDIX A

Influence of Magnetic Fields on the Fission Detector

It is a well-known fact, that magnetic fields have an influence on the collection efficiency and therefore on the gain of a photomultiplier. Even such weak fields as the earth's can have a significant effect, depending on the type of phototube under investigation. Although these effects on phototubes are well-known, their magnitude can be different, when a tube is attached to the metal framework of a gas scintillator.

The main influence of a magnetic disturbance takes place in the critical part of the photomultiplier between the photocathode and the collection electrode, the first dynode. Here, where the electrons, released from the photocathode by the incoming photons, are focused onto the collection electrode, the impact of a magnetic field is felt most strongly. This is because even a minute deviation, of the entering electron bunch from the optimum position on the first dynode, will result in a loss of secondary electrons and therefore has a significant effect on the multiplication through the whole set of dynodes. The magnetic field, to be most effective, has to be perpendicular to the electron bunch or at least to an ideal beam of electrons from the centre of the photocathode to the first dynode. To investigate the quantitative effect of magnetic fields, a series of tests was carried out. The setup is shown in pict. 62.

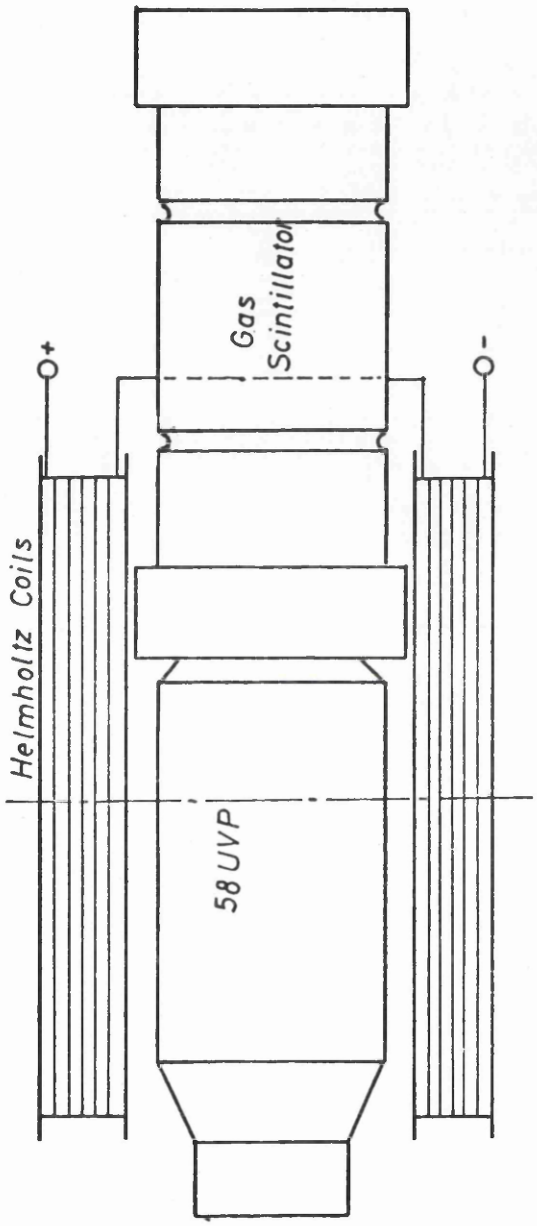

Pict.62: Setup of Magnetic Field Tests

A set of Helmholtz-coils was introduced with their axis perpendicular to the photomultiplier axis near the critical region of the 58 UVP photomultiplier, attached to the gas scintillator. When the distance between the coils is approximately equal to their radius, their magnetic field, created by the current, flowing through the coils, is nearly uniform. Current and voltage on the coils were measured, the photomultiplier was at 1 800 V, and the Cf-252 source was facing it inside the gas scintillator. For different currents, creating different magnetic fields, pulse amplitude spectra of the Cf-252 decay products were taken.

The magnetic field strength was calculated as follows:

$$B = \frac{\mu_0 N I a^2}{2(a^2+x^2)^{3/2}} \qquad \text{(A.1)}$$

where

$$\mu_0 = 4\pi \cdot 10^{-7} \ H/m \qquad \text{(A.2)}$$

a is the radius of the coils, x the distance between them, N the number of turns and I the current.

In this way a series of pulse amplitude spectra was obtained. They

are shown in pict. 63.As can clearly be seen, an increase in the strength of the magnetic field results in a decrease of photomultiplier again, until finally all pulses are moved up to the lower end of the spectrum, and no distinction, as to what is their nature, can be made any longer. A field strength of 1.25 G seemed the maximum acceptable, without disturbing the linear resolution too much. Since the magnetic fields, used in the tests, are of the order of magnitude of the earth's magnetic field, it appeared neccessary to use a Mu-metal shield all over the photomultiplier, to ensure stable working conditions during the experiments.

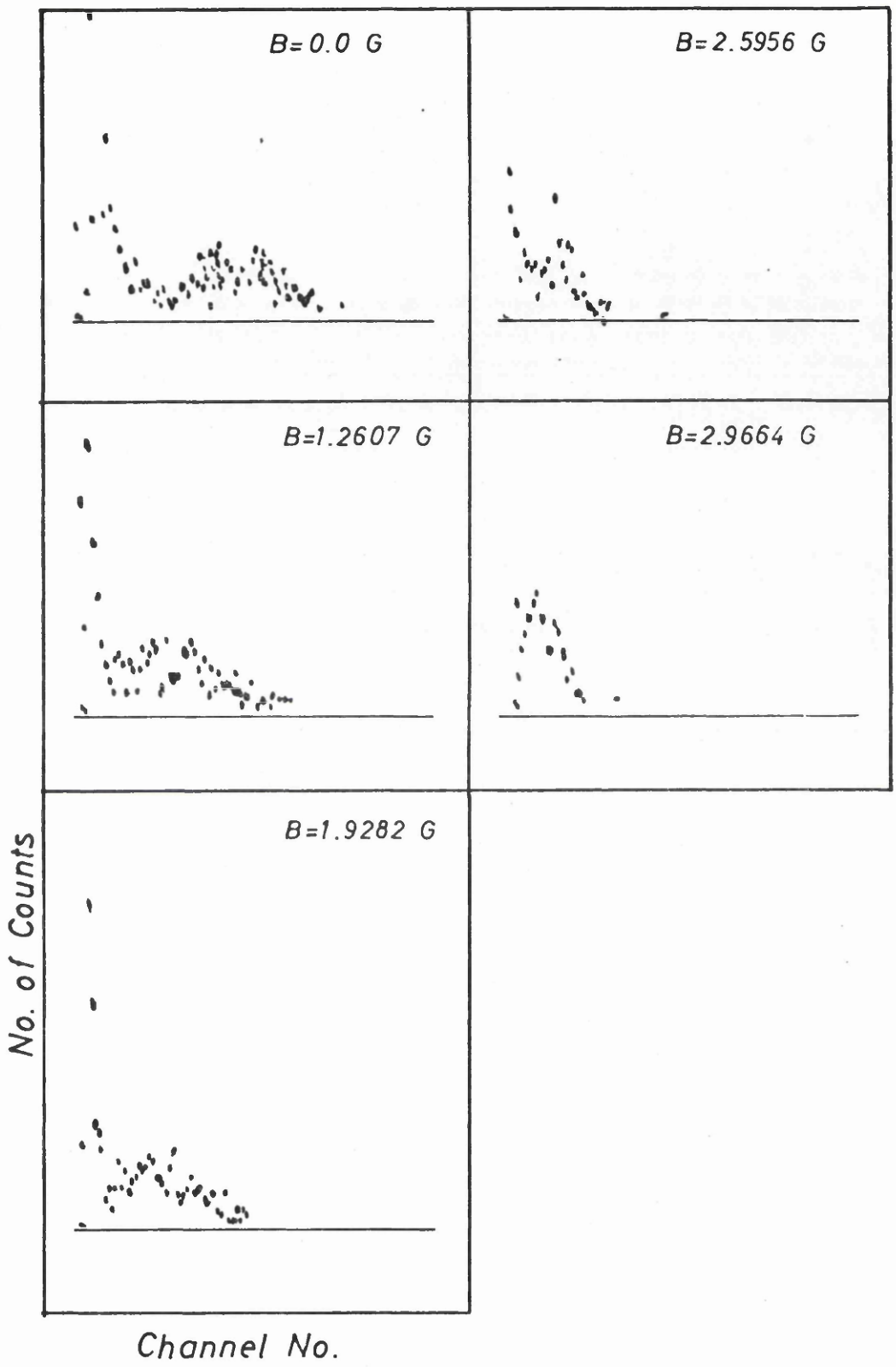

Pict.63: Cf-252 Spectra Under the Influence of Various Magnetic Fields

APPENDIX B

Investigation of Wave Length Shifters

Earlier on during the development of the gas scintillator the possibility of using wave length shifters, to avoid working in the UV-region, was investigated. Preliminary literature studies [25] singled out three possible candidates: Diphenylstilbene (DPS), p-Quarterphenyl and Diphenylbenzene. All are available as powders, but insoluble in commonly used media, such as water, various acids, benzene, etc.

The tests, concerning the usefulness of the shifters, were done in two parts. Firstly, it was decided qualitatively, which was the most efficient shifter, and secondly, the effect of it on Cf-252 spectra was investigated.

For the tests, the powders were mixed with Methylalcohol, and these mixtures were applied in turn to the quartz window in a thin layer. After the evaporation of the alcohol the powder remained evenly distributed on the disc. To make it stick, a microscopically thin film of lacquer was sprayed over it. Each shifter was then illuminated by a UV-lamp from different distances and at different intensities. The visual impact of the shifted light was observed and a qualitative decision made, that DPS was by far the most effective wave length shifter in these tests.

This was then used on the outer surface of the quartz window of the gas scintillator, between window and photomultiplier face, to investigate its effect on the Cf-252 spectrum, recorded by the gas scintillator. A success could not be achieved, since there was not a clear resolution of two separate fission peaks obtainable. This is mainly due to the difficulty of creating a thin enough, evenly distributed layer of wavelength shifter on the window. Because of its relative insolubility there were bound to be clusters in the mixture, thick enough, to absorb part of the scintillation pulse, and thus worsening the resolution. For this reason and for reasons of short response times the use of wavelength shifters in the experiments was decided against.

APPENDIX C

Determination of Target Mass

It has to be pointed out in advance that the method, described in the following, is only suited to give an estimate of the target mass. Since the thickness, quoted for the U-235 mass by the supplier, was only defined as approximate, it was decided to check this by a measurement of the total α-activity of the target foil. The setup for this measurement is shown in pict. 64.

The target was placed in a chamber, about 10 cm in diameter and 5 cm high. It was faced by a surface barrier semiconductur detector of 100 % α-detection-efficiency[73]. The chamber was evacuated, and the α-particles, leaving the foil, detected by the surface barrier counter. The counter was powered by a low voltage power supply and its output fed through a low noise pre-amplifier, before reaching a main amplifier. The output was displayed on a pulse height analyser, which gave out its contents on a teletype. In this way a spectrum of the α-activity of the U-235 foil was obtained. It is shown in pict. 65.

As one notices, the α-peak is in reality a double peak, both peaks having about equal height. This is because nearly 50 % of the total activity of the foil comes from U-234, which although of a natural abundance of 0.0055 %, its proportion is of course increased during

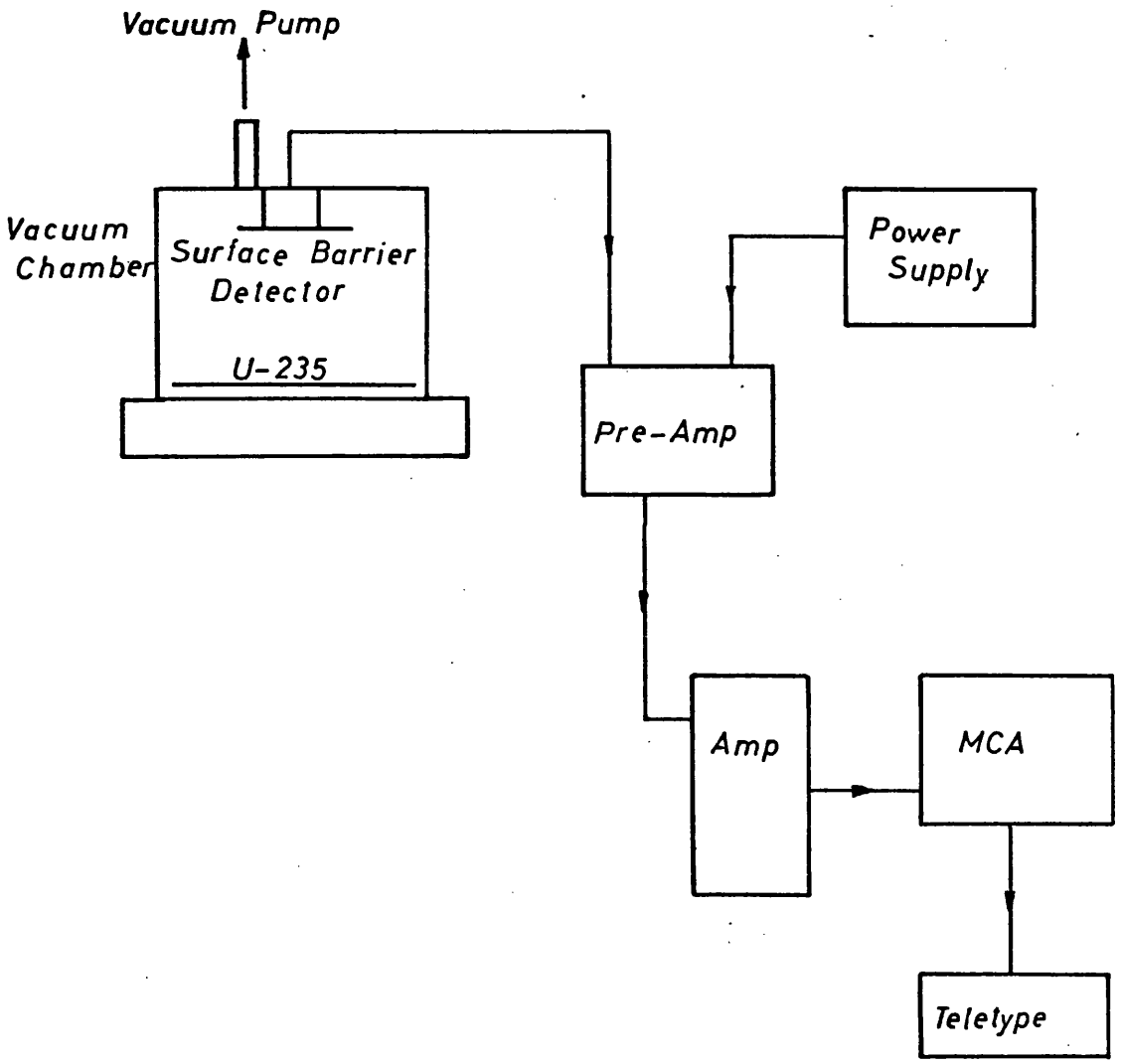

Pict.64: Setup For α-Activity Measurement of the U-235 Foil

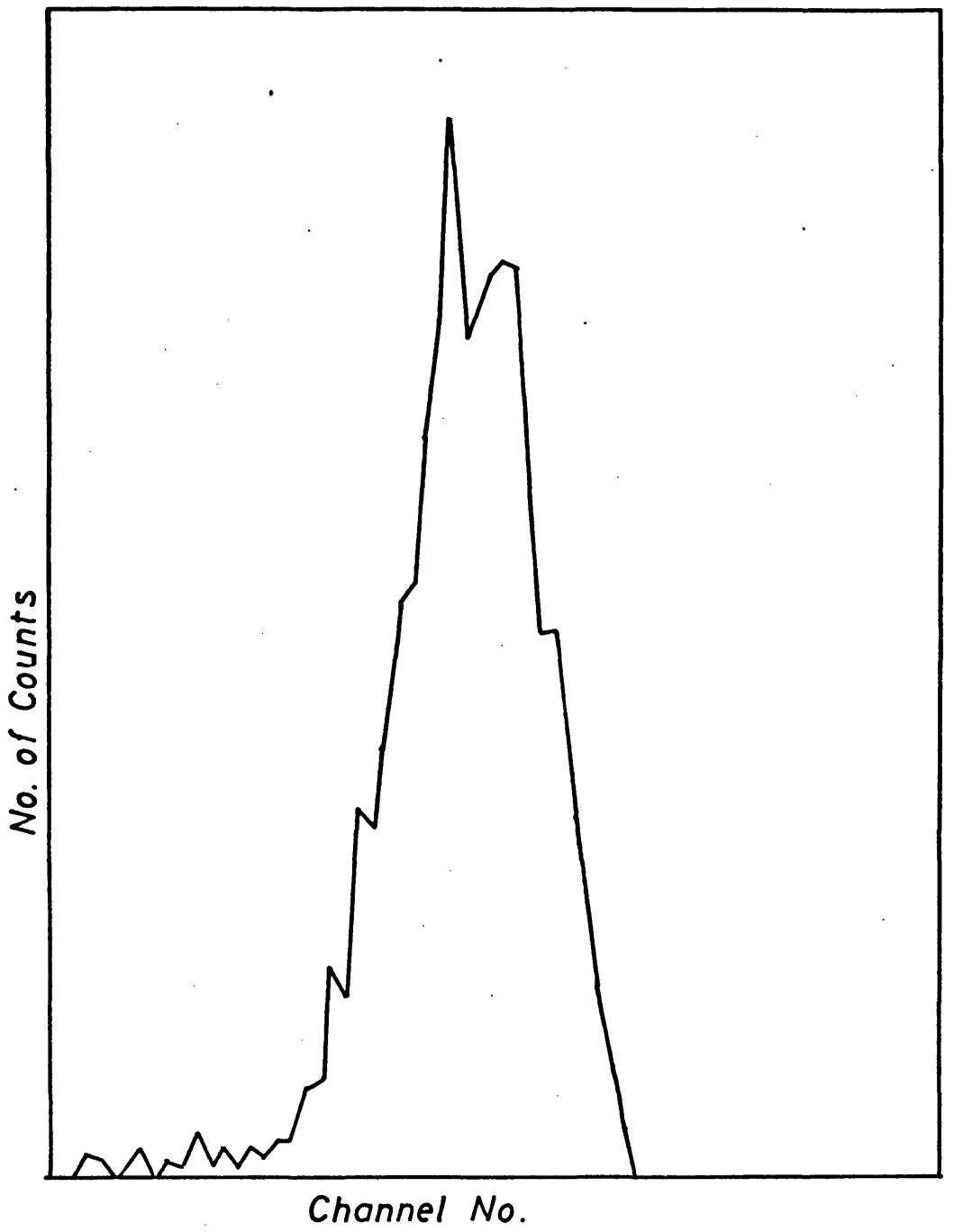

Pict.65: Energy Distribution of α-Particles From the U-235 Foil

the enrichment process of U-235 against U-238, which relies solely on an enrichment of the light component in natural Uranium in total.

Because the energies of the α -particles from U-234 and U-235 are very close, and the foil itself has a finite thickness, thus widening the energy distribution of both due to straggling, the peaks are not separable by using for example a higher quality detector. To determine the number of counts for U-235, it was therefore decided to assign about 50 % of its activity to U-235 on the basis of the relative peak heights.

This, however, was not the total activity of the foil, firstly, because of the solid angle of the detector to the foil, and secondly, because the foil was not a point source. Therefore Huygen's principle was applied to the foil, dividing it into a very fine mesh and assigning a point source to each square of the mesh in a computer code, called HYGEN. Each point source contributed to the total activity, according to its position relative to the detector face and was thus associated with a weighting factor. Taking care of the solid angle, subtended by the detector at the different point sources, the total activity of the foil could now be calculated, and from it the estimated mass of the target derived as 0.75 mg/cm^2.

This was 25 % lower than the quoted one, and two factors can account for this: firstly, the symmetrical splitup of the α-spectrum is probably not accurate enough, and secondly, part of the α-particles is lost due to straggling and absorption in the foil itself, thus reducing the measured activity by this portion with respect to the true one.

APPENDIX D

Listing of the Neutron Fission Cross Sections and Errors

E (MeV)	$\sigma_{n,f}$ U-235 (barns)	$\sigma_{n,f}$ U-238 (barns)	$\Delta E/E$ (%)	$\Delta\sigma/\sigma_{35}$ (%)	$\Delta\sigma/\sigma_{38}$ (%)
0.300	0.91		4.30	16.60	
0.309	0.79		4.36	17.00	
0.319	1.16		4.43	13.93	
0.329	0.84		4.50	16.41	
0.340	0.92		4.58	14.67	
0.351	0.87		4.65	15.55	
0.363	0.75		4.73	16.41	
0.375	0.66		4.81	15.71	
0.388	0.97		4.89	12.82	
0.402	0.87		4.98	12.82	
0.417	0.73		5.07	13.60	
0.432	0.85		5.16	13.39	
0.448	0.74		5.26	12.82	
0.465	0.69		5.36	12.25	
0.483	0.94		5.46	9.81	
0.503	0.75		5.57	10.10	
0.523	0.77		5.68	10.06	
0.545	0.70		5.80	9.51	
0.568	0.84		5.92	8.60	
0.592	0.79		6.04	8.30	
0.618	0.82		6.18	7.83	
0.646	0.71		6.31	8.55	
0.676	0.73		6.46	8.11	
0.708	0.87		6.61	7.19	
0.700	0.82	0.0105	3.28	10.43	88.88
0.716	0.92	0.0289	3.32	9.93	54.42
0.733	0.81	0.00493	3.36	10.12	125.69
0.751	0.92	0.0126	3.40	9.30	76.97
0.769	0.88	0.0	3.44	9.39	
0.788	0.74	0.0144	3.48	9.85	76.97
0.808	0.84	0.0177	3.52	9.42	62.84
0.829	0.71	0.0335	3.57	9.93	44.44
0.850	0.84	0.0204	3.61	9.07	56.21
0.872	0.80	0.0206	3.66	9.04	54.42
0.895	0.87	0.0241	3.71	8.14	47.50
0.919	0.93	0.0360	3.76	7.83	38.48
0.944	0.93	0.0394	3.81	7.70	36.28
0.970	0.98	0.0323	3.86	7.44	39.74
0.997	1.03	0.00913	3.92	7.49	76.97
1.026	0.85	0.0329	3.97	8.08	39.74
1.055	0.88	0.0283	4.03	7.60	41.14
1.086	0.90	0.0260	4.09	7.35	41.89
1.118	1.01	0.0562	4.15	7.08	29.09
1.151	0.83	0.0324	4.21	7.38	36.28

E (MeV)	$\sigma_{n,f}$ U-235 (barns)	$\sigma_{n,f}$ U-238 (barns)	$\Delta E/E$ (%)	$\Delta\sigma/\sigma_{35}$ (%)	$\Delta\sigma/\sigma_{38}$ (%)
1.187	0.99	0.0580	4.27	6.58	26.40
1.223	1.00	0.0330	4.34	6.53	34.86
1.262	1.02	0.0528	4.40	6.40	27.21
1.302	0.95	0.0383	4.47	6.72	32.45
1.344	0.97	0.0795	4.55	6.69	22.69
1.389	1.05	0.124	4.62	6.29	17.77
1.435	1.02	0.161	4.70	6.20	15.09
1.484	0.96	0.258	4.78	6.18	11.57
1.536	1.03	0.304	4.86	5.81	10.37
1.590	1.11	0.350	4.94	5.54	9.55
1.647	0.98	0.336	5.03	5.78	9.58
1.707	1.05	0.428	5.12	5.65	8.57
1.771	1.04	0.384	5.22	5.53	8.82
1.838	1.08	0.361	5.32	5.16	8.66
1.910	1.17	0.464	5.42	5.07	7.79
1.985	1.20	0.489	5.52	4.86	7.38
2.065	1.23	0.445	5.64	4.84	7.81
2.150	1.24	0.483	5.75	4.79	7.44
2.240	1.30	0.547	5.87	4.75	7.09
2.336	1.29	0.558	5.99	4.80	7.08
2.439	1.26	0.546	6.12	4.82	7.10
2.548	1.29	0.460	6.26	4.78	7.75
2.500	1.32	0.514	2.19	6.69	10.40
2.555	1.28	0.423	2.21	6.74	11.38
2.613	1.21	0.481	2.24	7.05	10.85
2.673	1.35	0.603	2.26	6.84	9.90
2.734	1.28	0.636	2.29	7.06	9.71
2.798	1.21	0.537	2.31	7.31	10.62
2.865	1.35	0.506	2.34	7.10	11.24
2.933	1.25	0.581	2.37	7.60	10.80
3.004	1.30	0.485	2.40	7.40	11.721
3.078	1.34	0.541	2.43	7.38	11.24
3.154	1.18	0.616	2.46	7.99	10.73
3.234	1.20	0.513	2.49	8.02	11.87
3.316	1.14	0.469	2.52	8.18	12.32
3.402	1.08	0.492	2.55	8.45	12.15
3.491	1.16	0.597	2.58	8.39	11.33
3.583	1.08	0.501	2.62	8.64	12.28
3.679	1.01	0.476	2.65	9.19	12.96
3.779	1.19	0.495	2.69	8.67	13.03
3.884	1.29	0.558	2.73	8.37	12.32
3.992	1.16	0.577	2.76	8.97	12.32
4.105	1.16	0.609	2.80	9.19	12.26
4.224	1.22	0.643	2.84	9.09	12.15
4.347	1.11	0.576	2.88	9.55	12.82
4.476	1.08	0.518	2.93	9.69	13.55
4.611	1.06	0.575	2.97	9.69	12.76
4.751	1.12	0.582	3.02	9.36	12.56
4.899	1.04	0.540	3.06	9.81	13.20
5.053	1.01	0.581	3.11	10.16	12.96
5.215	1.06	0.675	3.16	10.06	12.20
5.385	1.04	0.598	3.21	10.12	12.96

E (MeV)	$\sigma_{n,f}$ U-235 (barns)	$\sigma_{n,f}$ U-238 (barns)	$\Delta E/E$ (%)	$\Delta\sigma/\sigma_{35}$ (%)	$\Delta\sigma/\sigma_{38}$ (%)
5.563	1.01	0.509	3.26	10.35	14.11
5.751	1.09	0.529	3.32	10.09	14.05
5.948	1.17	0.607	3.38	9.75	13.10
6.155	1.26	0.671	3.43	9.75	12.96
6.373	1.40	0.664	3.49	9.65	13.55
6.604	1.60	0.834	3.56	9 .34	12.50
6.847	1.51	0.915	3.62	9.78	12.15
7.103	1.61	0.961	2.69	9.52	11.93
7.375	1.68	0.914	3.76	9.54	12.52
7.662	1.64	0.896	3.83	10.22	13.39
7.967	1.86	0.949	3.91	9.99	13.55
8.290	1.86	0.950	3.99	10.28	13.93
8.633	1.59	0.899	4.07	11.33	14.61
8.999	1.60	0.973	4.15	11.62	14.41
9.388	1.69	0.898	4.24	11.82	15.71
9.803	1.79	0.732	4.33	11.98	18.14
10.246	1.83	0.720	4.43	12.15	18.73
10.720	1.78	0.763	4.53	12.82	18.94
11.228	1.64	0.697	4.64	13.71	20.39
11.774	1.76	0.768	4.75	14.05	20.57
12.360	1.74	0.859	4.87	14.81	20.39
12.992	1.67	0.912	4.99	15.35	20.12

REFERENCES

1. O. Hahn and F. Strassmann, Naturwiss. 27, 11 (1939)
2. L. Meitner and O. R. Frisch, Nature, 143, Feb 1939
3. N. Bohr and J. A. Wheeler, Phys. Rev., 56, Sept 1939
4. C. F. v. Weizsaecker, Zeitschr. f. Phys., 96, July 1935
5. D. L. Hill and J. A. Wheeler, Phys. Rev., 89, 5 (1951)
6. J. R. Nix and W. J. Swiatecki, Nucl. Phys., 71, Sept 1965
7. W. D. Meyers and W. J. Swiatecki, Nucl. Phys., 81, June 1965
8. V. M. Strutinsky, Nucl. Phys., A 122, Dec 1968
9. J. E. Lynn, AERE-R7468, Nov 1974
10. D. F. Jackson: "Nuclear Reactions", Methuen & Co. Ltd., London, 1970
11. H. Feschbach et al. Phys. Rev., 96, 1 (1954)
12. W. Hauser and H. Feschbach, Phys. Rev., 87, 2 (1952)
13. E. Pfletschinger and F. Kaeppeler, NSE, 40 (1970)
14. W. P. Penitz: "Additional Measurements of the Ratio of the Fission Cross Sections of Plutonium-239 and Uranium-235", August 1971
15. W. P. Penitz and R. J. Armani, JNE, 26 (1972)
16. J. W. Meadows, NSE, 49 (1972)
17. W. G. Davey, NSE, 32 (1968)
18. W. G. Davey, NSE, 26 (1966)
19. M. G. Sowerby et al., AERE-R 7273 (1973)
20. W. Finkelnburg: "Einfuehrung in die Atomphysik", Springer Verlag, Berlin-Heidelberg-New York, 1967
21. J. W. Behrens, UCRL-51478 (1973)
22. G. I. Crawford et al., J. Phys. A, 7, 12 (1974)
23. G. D. James, ANL-7320 (1966)
24. G. I. Crawford et al., NIM, 109 (1973)

25. J. B. Birks: "The Theory and Practice of Scintillation Counting", Pergamon Press, 1964

26. R. Pagano and J. A. Wethington, Jr., Trans. Am. Nucl. Soc., 14 (1971)

27. W. P. Lutsenko et al., Atomn. Energya, 32, 5 May 1972

28. M. Pickering and J. M. Alexander, Phys. Rev. C, 6, 1 (1972) p. 332

29. M. Pickering and J. M. Alexander, Phys. Rev. C, 6, 1 (1972) p. 343

30. D. Blanc et al., Nucl., 11, (1970)

31. R. Henck and A. Coche, IEEE Trans. Nucl. Sc., Feb 1967

32. V. I. Lyashenko et al., Pribory i Tekhnika Eksperimenta, 5 (1971)

33. J. B. A. England: "Techniques in Nuclear Structure Physics, Part I", MacMillan , 1974

34. H. Koehler et al., Kernenergie, 12, 12 (1969)

35. "Mullard Technical Handbook, Part II: "Valves and Tubes", Mullard Ltd., 1973

36. R. Pagano and J. A. Wethington, Jr., Trans. Am. Nucl. Soc., 13 (1970)

37. S. J. Hall and J. McKeown, NIM, 112 (1973)

38. R. Staubst et al., NIM, 84 (1970)

39. J. B. Czirr et al., NIM, 31 (1964)

40. J. D. Kellie and G. I. Crawford, NIM, 72 (1969)

41. Z. H. Cho et al., NIM, 52 (1967)

42. USAEC: "Neutron Cross Sections", McGraw - Hill Book Co. Inc., New York (1955)

43. S. Cierjacks et al., KFK 1000 (1968)

44. A. D. Wilkinson et al.: "A Multi-Purpose Computer Network" (1970)

45. Digital Equipment Corporation: "The PDP-10 Timesharing Manual", Maynard, Mass. (1970)

46. private communication

47. private communication

48. California Radiation Laboratory, AECU - 663 (1949)

49. W. N. Reisdorf et al., Nucl. Phys., A 205 (1973)

50. M. J. Bennet and W. E. Stein, Phys. Rev., 156, Apr 1966

51. S. S. Kapoor et al., Phys. Rev., 137 , Febr 1965

52. F. Pleasonton, Phys. Rev. Oct 1968

53. J. Jungermann and S. C. Wright, Phys. Rev., 76, Oct. 1949

54. V. P. Zakharova et al., Sov. Jour. Nucl. Phys., 16, Apr 1973

55. P. P. D'Yachenko et al., Sov. Jour. Nucl. Phys., 14, June 1972

56. V. G. Vobor'eva et al., Sov. Jour. Nucl. Phys., 10, Mar 1970

57. R. H. Iyer and M. L. Sagu: "Fragment Angular Distributions In the 14 MeV Neutron Induced Fission of Th-232, U-233, U-235, U-238, Np-237, Pu-237 and Am-241, Using Solid-State Track Detectors", Radiochemistry Division, Bhata Atomic Research Centre, Trombay, Bombay - 85, 1970

58. NEA, IAEA, private communication, 1975

59. ILL, Annual Report 1974, Grenoble

60. V. S. Nikolaev and I. S. Dmitriev, Sov. Phys. - Techn Phys., 15, Febr 1971

61. "The American Insitute of Physics Handbook", McGraw - Hill Book Co. Inc., New York, 1957

62. O'Dell et al., NIM, 61, (1968)

63. G. S. Sidhu and J.B. Czirr, UCRL - 76508, Feb . 1975

64. J. Blons et al., Phys. Rev. Lett., 35, No. 26, Dec 1975

65. B. B. Back et al., Phys. Rev. Lett., 28 No. 26, June 1972

66. G. D. James et al., Nucl. Phys., A189, June 1972

67. J. W. Behrens et al. UCRL - 76219, Mar 1975

68. J. D. Kellie, private communication

69. B. Buck et al., "Computer Programms For the Optical Model Analysis of Nuclear Scattering", Nuclear Physics Laboratory, Oxford

70. J. M. Cohenca, "Computer Programme For Optical Model Analysis of Nuclear Scattering", Nuclear Physics Laboratory, Oxford

71. J. E. Lynn, "The Theory of Neutron Resonance Reactions", Claredon Press, Oxford, 1968

72. D. B. C. B. Syme et al., ANSE, Vol. 1, 1974

73. K. D. Ledingham, private communication